N° d'ordre : 40949

THESIS

Submitted to

Université Lille 1- Sciences et Technologies

by

Pranay P. Morajkar

For obtaining the PhD degree of the

Doctoral School SMRE: Sciences de la Matière, du Rayonnement et de l'Environnement

Application of laser photolysis coupled to time resolved optical detection methods to study the kinetics and spectroscopy of atmospherically relevant species

07/11/ 2012

Jury committee

1. Dr. Christa Fittschen **Research Director, CNRS, Université Lille 1 – Sciences et Technologies, France.**	**Thesis supervisor**
2. Prof. Eric Villeneuve **EPOC, Université Bordeaux 1, France.**	**Thesis co-supervisor**
3. Dr. Birger Bohn **Researcher, Institut für Energie- und Klimaforschung, Forschungszentrum Jülich GmbH, Germany**	**Referee**
4. Dr. Chakir Abdelkhaleq **Researcher, groupe de Spectrométrie Moléculaire et Atmosphérique Université de Reims, Reims, France**	**Referee**
5. Dr. Jean-Christophe Loison **Researcher, Institute de Science Moléculaire Université Bordeaux 1, France.**	**Examiner**

To my beloved parents

for their everlasting love and support …

Abstract

OH and HO_2 radicals play a vital role in many oxidation processes in the atmosphere. The degradation of volatile organic compounds under tropospheric conditions is induced by reaction with hydroxyl radicals followed by the subsequent chemistry of the initial OH oxidation products with O_2. This thesis deals with the kinetic study of some of these atmospherically relevant reactions to better understand their oxidation mechanisms using experimental techniques such as laser photolysis coupled to detection by Laser Induced Fluorescence (LIF, for OH), continuous wave- Cavity Ring-down Spectroscopy (cw-CRDS, for HO_2) and time resolved UV spectroscopy (UV, for Hexamethylbenzene-OH adduct).

Different chemical systems have been studied using the above techniques: 1) the reaction of HO_2 radicals with formaldehyde, 2) the 248 nm photolysis of acetaldehyde and 3) the OH initiated oxidation of Hexamethyl benzene. In addition to this, the spectroscopic application of cw-CRDS technique and UV spectroscopy has been used for the measurement of absorption cross section of selected absorption lines of formaldehyde in the near infrared region and Hexamethylbenzene-OH adduct in the UV region respectively.

Keywords: Atmospheric chemistry – Radicals – Hydroxyl – Laser Induced Fluorescence – Flash Photolysis – Hydroperoxyl – cw-CRDS spectroscopy – UV spectroscopy

Résumé

Les radicaux OH et HO_2 jouent un rôle essentiel dans beaucoup de processus d'oxydation dans l'atmosphère. La dégradation des composés organiques volatils dans les conditions troposphériques est généralement initiée par la réaction avec les radicaux OH, suivie par la réaction des produits d'oxydation avec l'oxygène. Dans le cadre de cette thèse, des études ont été menées afin de mieux comprendre les mécanismes d'oxydation d'espèces d'intérêt atmosphérique. Pour cela, un système expérimental de photolyse laser couplée à des techniques spectroscopiques de détection résolues dans le temps : Continuous Wave Cavity ring-down Spectroscopy (cw-CRDS) pour HO_2, Laser Induced Fluorescence (LIF) pour OH et spectroscopy UV pour l'adduit Hexamethylbenzene-OH (HMB-OH) ont été utilisés.

Différents systèmes chimiques ont été étudiés en utilisant ce dispositif expérimental : 1) la réaction d'HO_2 avec CH_2O, 2) la photolyse à 248 nm de l'acétaldéhyde et 3) la dégradation de HMB initiée par OH. Les techniques de cw-CRDS et d'absorption UV ont été utilisées respectivement pour mesurer les sections efficaces de CH_2O et de l'adduit HMB-OH.

Keywords: Chimie l'atmosphère – Radicaux – OH – Laser Induced Fluorescence – photolyse laser – HO_2 – cw-CRDS spectroscopie – UV spectroscopie

Acknowledgements

I would like to start thanking my thesis supervisor, Dr. Christa Fittschen and co-supervisor, Prof. Eric Villenave for their support, patience and wise supervision during the preparation of this thesis. I owe them my profound admiration and respect.

Many thanks to Prof. Jean-François Powels, director of PC2A, and all other colleagues, who always gave me the encouragement to during the Ph.D work.

My sincere thanks to the referees and examiners of my thesis Dr. Birger Bohn, Dr. Chakir Abdelkhaleq, Dr. Jean-Christophe Loison and Prof. Denis Petitprez for evaluating my thesis and suggesting valuable corrections.

I would like to sincerely acknowledge Prof. J.B. Fernandes, Dr. Coralie Schoemaecker, Dr. Pierre-Marrie Flaud, Dr. Ravi Fernandes, Dr. Purnakala Samant, Dr. Jyoti Sawant, Mrs. Varsha Sail and Dr. Chaitanya Jain, for their guidance, collaboration and encouragement at different stages of this work.

My sincere thanks to my friends and colleges of PC2A and LPTC namely, Damien Amédro, Pascale Dewalle, Marion Blocquet, Matthieu Riva, Amélie Guillon, Caroline Rio for their support, encouragement and for making my stay at the two labs a learning and enjoyable experience.

I would like to thank my Indo-European friends namely, Sascha Nehr, Madda lena, Ham Zhaa, Sidane, Mohammad Tunsi, Anand Teerthan , Sri Bharani, Manik Mayur, P.R. Narendra, Lishil Silvester, Selva Kumar, Ajay Ghalwadkar, Pushpendra Kumar, Samadhan Lomate for their support and making my life easier, here in France.

My sincere thanks to my friends from India namely, Vithal Morajkar, Prajot Morajkar, Sonali Banavlikar, Richa Sardessai, Priyanka Bidaye, Padmadeep Ambre, Kiran Naik, Pradnesh Satardekar, Satu Gawas, Sandesh Naik, Mira Permekar, Mamta Naik, Milind Naik and many more for always being the supporting and comforting hand I needed the most and for their encouragement and long distance support ☺

I owe my sincere thanks to all the other members of PC2A for their everlasting help and support throughout my stay here.

I would like to acknowledge European Union *via* IRENI, CNRS, DFG and Nord Pas Calais region, France for providing the financial support for this thesis and their continuous contribution to the development of science, technology and higher education in France.

At the last but the most important, I would like to conclude by thanking my parents, Mr. Pradeep Morajkar and Mrs. Pratibha Morajkar and all my relatives, for their everlasting love, support and blessings throughout my life.

Table of Contents

Chapter 1

Chapter 2

2 Experimental Techniques

Chapter 3

3 The Chemistry of CH_2O + HO_2 radicals

Chapter 4

4 248 nm photolysis of acetaldehyde: Quantum yields of H and HCO radicals

Chapter 5

5 OH initiated oxidation of Hexamethyl benzene

Chapter 1
Introduction

1 Introduction

The atmosphere comprises of different layers namely, Troposphere, Stratosphere, Mesophere and Thermosphere. The troposphere is the lowest layer of earth's atmosphere. which starts at earth's surface and goes up to a height of 7 to 20 km above sea level. The troposphere by itself acts as a huge chemical reactor, driven by the solar radiation. The chemistry of the troposphere is influenced by both natural and manmade processes which in turn affect the quality of life on earth. The simultaneous emission of NO_x (sum of NO and NO_2) as well as Volatile Organic Compounds (VOCs) from both natural and anthropogenic sources is the major cause of the tropospheric pollution which leads to harmful processes such as smog formation, acid rain, increase in the tropospheric ozone and global warming etc. The industrialization has lead to a dramatic increase in these unwanted processes and hence a great deal of research has been devoted since many years on the understanding of fundamentals of these chemical processes, their origin and their influence on life as a whole.

The understanding of the importance of the atmospheric chemistry of VOCs in the presence of NO_x started more than 50 years ago with the pioneering studies on Los Angeles smog by Haagen- Smit [1]. A detailed understanding of the photochemical smog formation has grown since then through the combination of smog chamber studies, laboratory kinetic measurements, air quality monitoring, field measurements and computer modeling studies [2]. It has been understood so far that the major emission of VOCs originate from the biogenic sources such as direct emission from the vegetation, and natural processes such as volcanic activities and forest fire etc (about 1150 million tons per year, [3, 4]). However, the troposphere has its own defense mechanism which allows cleaning the troposphere free of VOCs. The highly reactive OH radicals that are produced in the troposphere by the reaction of $O(^1D)$ with H_2O act as a detergent for the troposphere. These OH radicals initiate the oxidation process of VOCs which undergo further complex chemistry forming different products finally leading to removal of VOCs or their photo-oxidation products from the troposphere through dry or wet deposition. Hence the OH radical budget determines the oxidative capacity of the troposphere. This radical budget is significantly affect by addition of NO_x from anthropogenic sources such as combustion (vehicle and industrial processes) as well as through addition of VOCs from, industrial solvent storage, transport, and hazardous industrial waste [5, 6]. Around 60 million to 140 million tons of volatile organic compounds are emitted to the troposphere through anthropogenic sources [4].

The lifetime of different VOCs emitted to the troposphere is governed either by their photolysis by solar radiation or their reactivity towards OH radicals (and, to a minor extend for some unsaturated VOCs, reaction with NO_3 and O_3). It is important to understand the fate of the photo-oxidation processes of VOCs as it leads to production of new radical species which, in presence of O_2 and NO_x, leads to the generation of Oxygenated Volatile organic compounds (OVOCs) and Ozone as well as short lived oxygenated radical species such as Hydroperoxy radicals (HO_2). The OVOCs have relatively low vapor pressures and higher solubility in water. Hence they can be deposited on surfaces, washed out with rain or can condense to form clusters which finally leads to the formation of secondary organic aerosols (SOA) [7].

It has been well known that the stratospheric ozone is very important for the existence of life on earth as it filters the harmful UV radiation of the sun. In contrast, the tropospheric ozone acts as a toxic gas and is harmful for animal and plant life. Moreover, the tropospheric ozone acts as a green house gas and contributes to global warming. Hence it becomes very important to understand the tropospheric photochemistry not just for the removal of VOCs from the troposphere but also to understand the fate of the potentially hazardous photochemical products as both VOCs and OVOCs could have toxic or carcinogenic effects or could result in respiratory and cardiovascular disorders.

1.1 Photochemistry of the troposphere

As already explained earlier, the generation of OH radicals is vital for the removal of VOCs from the troposphere. The major source of OH radicals in the troposphere is through photochemical production from the photolysis of O_3 leading to electronically excited $O(^1D)$ which then reacts with H_2O to form OH radicals.

$$O_3 + h\nu \rightarrow O(^1D) + O_2 \quad \leq 330\text{ nm} \qquad (R1)$$

$$O(^1D) + H_2O \rightarrow 2\,OH \qquad (R2)$$

However, most of the electronically excited $O(^1D)$ are quenched by collision with either N_2 or O_2 to produce ground state $O(^3P)$ which further combines with O_2 to form O_3. Around 10% of the $O(^1D)$ reacts with H_2O to produce OH radicals and this limits the initial concentration of the OH radicals in the troposphere.

$$O(^1D) + O_2/N_2 \rightarrow O(^3P) \qquad (R3)$$

$$O(^3P) + O_2 + M \rightarrow O_3 + M \qquad (R4)$$

During the day time, OH initiated oxidation of VOCs occurs depending on the type of the VOC (represented as “RH”) either via OH addition on to the VOC or H abstraction as shown below:

$$OH + RH \rightarrow HO\text{-}RH \quad \text{(addition)} \qquad (R5)$$

$$OH + RH \rightarrow R + H_2O \quad \text{(abstraction)} \qquad (R6)$$

The subsequent chemistry of HO-RH and R in presence of O_2 results in the formation organic peroxy radicals (RO_2). The reaction R7 can also proceed via formation of hydroperoxy radicals (HO_2) the so called “prompt HO_2”. However, this channel is not the typical of all VOC and is observed only in case of aromatic compounds such as BTX.

$$HO\text{-}RH + O_2 \rightarrow RO_2 \qquad (R7)$$

$$R + O_2 \rightarrow RO_2 \qquad (R8)$$

In absence of NO, both HO_2 and RO_2 radicals can undergo chain termination reaction forming stable products as shown below:

$$HO_2 + HO_2 \rightarrow H_2O_2 + O_2 \qquad (R9)$$

$$HO_2 + OH \rightarrow H_2O + O_2 \qquad (R10)$$

$$HO_2 + RO_2 \rightarrow ROOH + O_2 \qquad (R11)$$

$$RO_2 + RO_2 \rightarrow ROOR + O_2 \qquad (R12)$$

In addition to the stable products in reaction R11, it has now been understood that depending on the type of RO_2, the reaction of RO_2 + HO_2 also proceeds through other channels producing radical species (more details in Chapter 3). However, in presence of NO, both HO_2 and RO_2 enter a radical propagating chain leading to organic alkoxy radicals (RO) or regeneration of OH radicals as shown below.

$$RO_2 + NO \rightarrow RO + NO_2 \qquad (R13)$$

$$HO_2 + NO \rightarrow OH + NO_2 \qquad (R14)$$

The RO radicals enter a complex reaction sequence which in presence of O_2 produces HO_2 radicals and other products. The NO_2 produced in the above reactions, is photolysed by the solar radiation at wavelengths <400 nm to produce NO + O and the subsequent reaction of O with O_2 leads to the production of O_3. This is the only known source of tropospheric O_3. Hence both OH and HO_2 radicals together play a vital role in the oxidation chemistry of the troposphere. The above understanding of the tropospheric photochemistry is based on numerous studies carried out both through field measurements and laboratory scale experiments [8–10]. The instruments which are used to measure the radical chemistry during field measurements, needs proper validation both for sensitive and selective measurements of the radical chemistry of the troposphere.

1.2 VOCs in the troposphere

The concentration of different VOCs in the troposphere largely depends on their sources and sinks. Hence it is important to understand the different sources and the possible sinks of the VOCs in the troposphere. The total number of VOCs present in the troposphere are numerous and more details on these VOCs can be found for example in the reviews by Atkinson et al. [11–13]. Hence, the present discussion on sources and sinks of the volatile organic compounds is restricted to those organic compounds whose gas phase OH initiated oxidation was investigated during the course of this thesis: Formaldehyde (CH_2O), Acetaldehyde (CH_3CHO) and Hexamethyl benzene (HMB).

1.2.1 Formaldehyde (CH_2O)

Formaldehyde is an important constituent of the tropospheric photochemistry. It is an indoor and outdoor air pollutant and acts as an interesting compound for determining the oxidative capacity of the troposphere [14]. formaldehyde is ubiquitously found throughout the troposphere with levels ranging from a few ppt in clean background air to a few tens of ppb in polluted areas such as metropolitan cities [15, 16]. Formaldehyde is produced as a major intermediate in the oxidation of many VOCs such as CH_4 and isoprene, the major biogenic VOCs in the troposphere. It is also produced directly, for example during biomass burning. The anthropogenic sources include combustion of fuels, industrial onsite uses and off-gassing from building materials [17]. Formaldehyde is not directly present in gasoline but it is emitted as a result of incomplete combustion in the internal combustion engines [18]. Industrial emission of formaldehyde occurs during its production process, storage and transport etc. It has also been detected in the emission from chemical manufacturing plants, pulp and paper mills, tire and rubber plants, textile mills etc. [19].

Reaction with OH radicals or photolysis by solar radiation are the two primary sinks for formaldehyde in the troposphere. Minor processes include reactions with nitrate radicals, hydroperoxyl radicals, hydrogen peroxide, ozone etc. Small amounts of formaldehyde may also be removed by dry or wet deposition. The overall tropospheric lifetime of formaldehyde is estimated to be only a few hours during day time when the photolysis rates and the OH concentrations are at the maximum [20].

1.2.2 Acetaldehyde (CH_3CHO)

Acetaldehyde is ubiquitous in the environment. It plays an important role in the atmosphere as a source of O_3, Peroxy Acetyl Nitrates (PAN) [21] and HO_x and has been classified as a hazardous air pollutant by Environmental Protection Agency (EPA) [22]. Acetaldehyde is emitted to the atmosphere both through direct anthropogenic and natural emissions as well as generated during the photochemical oxidation of VOCs such as alkanes and alkenes. The later case is thought to be the dominant source of acetaldehyde in the atmosphere (60%) [25]. The anthropogenic sources of acetaldehyde (<1%) [25] includes incomplete combustion of wood in fireplaces and woodstoves, the combustion of gasoline and diesel fuel in motor vehicles, refining and waste processing in coal plants, combustion of fossil fuels in power plants etc. Forest fires and biomass mass burning also acts as direct emitters of acetaldehyde (1.5%) [25]. Apart from the photochemical production of acetaldehyde, it has recently been understood that acetaldehyde is directly emitted to the environment by terrestrial plants (10%) [25]. Acetaldehyde is produced in the plant leaves and roots as a product of some fermentation reactions [23, 24]. Photo-oxidation of dissolved organic matters at the ocean surface also acts as acetaldehyde emitters (27%)[25]. The major sinks of acetaldehyde in the gas phase are a) its oxidation by OH radicals (88%) [25], b) photolysis by solar radiation (10 % [25]) and c) dry and wet deposition (<2%) [25]. The global atmospheric lifetime of acetaldehyde in the troposphere is ~ 0.8 days. The above details on the sources and the sinks of acetaldehyde was obtained from reference [25].

1.2.3 Hexamethyl Benzene (HMB)

Hexamethyl benzene has not been reported till date to be present in the troposphere. It exists in the solid crystalline form and has a very low vapor pressure at ambient temperatures (0.025 mmHg at 25^oC). Hexamethylbenzene has been studied during the course of this thesis because it serves as an excellent model compound in order to address very specific problems and challenges in understanding the OH initiated oxidation mechanism of monocyclic aromatic compounds such as benzene, toluene and xylenes etc. The details pertaining to the complexity of the OH initiated oxidation mechanisms of monocyclic aromatic compounds and the recent challenges in these studies will be discussed in detail in the introductory section in Chapter 5. Since, the hexamethylbenzene oxidation study could provide some useful information on the OH initiated oxidation mechanisms of other monocyclic aromatic compounds such as benzene, toluene and xylenes etc, the present section will highlight the sources and the sinks of benzene, toluene and xylenes which are present in the atmosphere.

Benzene, Toluene and Xylenes (BTX) are released into the atmosphere through both natural and more importantly through anthropogenic sources. The natural sources include forest fires, plant volatiles and crude oil seeps [26]. The anthropogenic sources that contribute to the atmospheric concentration are automobile exhaust, automobile refueling processes, industrial production, storage and transportation [27]. The major sink for BTX in the atmosphere is its oxidation initiated by the photo-chemically generated OH radical. Depending on the concentration of OH radicals, their atmospheric lifetime can vary from 2 - 3 hours to 3 - 4 days [9, 10]. All the VOCs discussed above, actively participate in the tropospheric photochemistry, resulting in both consumption and production of new radicals and products. The radical chemistry continues until the oxidation products are finally removed either through dry or wet deposition.

Since, tropospheric chemistry as a whole is very complex as numerous radical reactions occurs simultaneously, laboratory experiments play an important role in providing the basic understanding of reaction pathways, branching ratios and rate constants for elementary reactions of VOC oxidation. The results of these studies are then used in various regional and global models which is then validated by comparison with field measurements. The measurements carried out during the course of this thesis were focused on laboratory kinetic measurements of OH initiated oxidation of the VOCs by monitoring the time resolved kinetics of OH radicals, HO_2 radicals and the aromatic–OH adducts. The experimental techniques that are available for both field measurements and laboratory scale measurements of OH and HO_2 radicals have already been discussed in detail in the previous two thesis of the same group [28, 29] and hence won’t be repeated here again.

It is almost impossible to detect aromatic-OH adduct concentrations in the field measurements as the aromatic-OH radical under high oxygen concentrations (as in the atmosphere), immediately converts to peroxy radicals. Hence, the aromatic-OH adducts are only measured in the laboratory under experimental conditions of low O_2 ($\leq 10^{15}$ molecules cm^{-3}). The only direct laboratory measurements of aromatic-OH adduct have been reported over the past decade using laser photolysis coupled to detection by time resolved UV absorption spectroscopy. Hence, in order to measure the HMB-OH adduct UV spectrum and to monitor its decay kinetics, the laser photolysis coupled to a time resolved UV spectrometer was used during the course of this thesis. The laser photolysis coupled to time resolved UV absorption spectrometer, along with the laser photolysis coupled to continuous wave- Cavity Ring-down Spectroscopy (cw-CRDS) and Laser Induced Fluorescence (LIF) technique which were used during the course of this thesis for the detection and kinetic measurements of HMB-OH adduct, HO_2 and OH radicals respectively, will be discussed in detail in the experimental section in Chapter 2. In the next section, we shall discuss in brief, the general principles underlying the above mentioned experimental techniques.

1.3 General principle of the experimental techniques used during the course of this thesis

The general principle of the experimental techniques used during the course of this thesis for the laboratory scale detection and measurement of the reaction kinetics of OH, HO_2 and HMB-OH adduct is described in this section.

1.3.1 Laser Induced Fluorescence (LIF) technique

The term fluorescence refers to the emission of light radiation by atoms or molecules that have been excited by the absorption of radiation. The term laser induced fluorescence specifies that the excitation photon is provided by a laser. The target species which is often the ground vibrational level of the electronic ground state (S_0) absorbs the photon emitted by the laser and excites the target species to one of the excited vibrational level of the electronic excited state (S_1) as shown in Figure 1. 1.

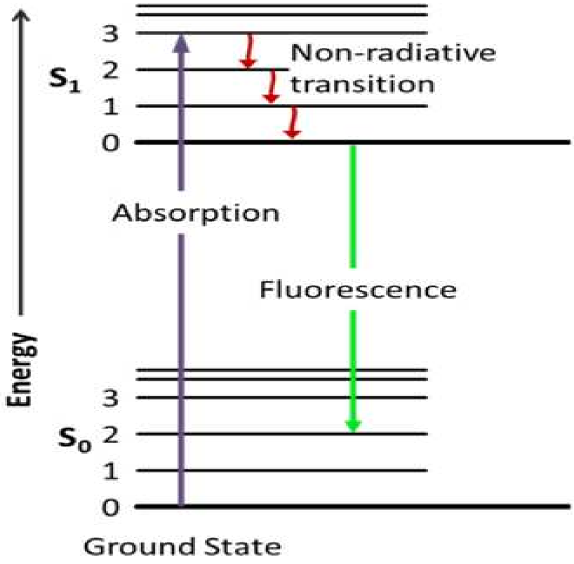

Figure 1. 1: A part of the Jablonski diagram showing the fluorescence process [30]

The molecule in the higher vibrational excited level of the electronic excited state can relax to the lowest vibrational level of the electronic excited state through non radiative transitions. From this lowest vibrational level of the electronic excited state, the molecule can undergo spontaneous light emission to return to one of the vibrational levels of the electronic ground state. The emitted light photons are usually of longer wavelength. This process is called as fluorescence. Apart from the fluorescence process, the molecule in the excited electronic state can relax to higher vibrational levels of the electronic ground state through a non radiative process such as heat loss (internal conversion) or it can also undergo intersystem crossing to a triplet state before returning to the electronic ground state (Phosphorescence). In the present work, laser induced fluorescence technique has been used to detect OH radicals. This is achieved by exciting OH radicals from the ground vibrational level of the electronic ground state ($X^2\,\Pi$) to the first excited vibrational level of the first excited electronic state ($A^2\Sigma$) using photons around 282 nm. The rotational transition involved during the OH excitation process is **Q1 (4.5)** (*Hunds case "a"*) at 282.438 nm and the red shifted fluorescence is detected at around 310 nm (1-1 and 0-0 A-X transitions). The OH detection using the LIF is shown in Figure 1. 2.

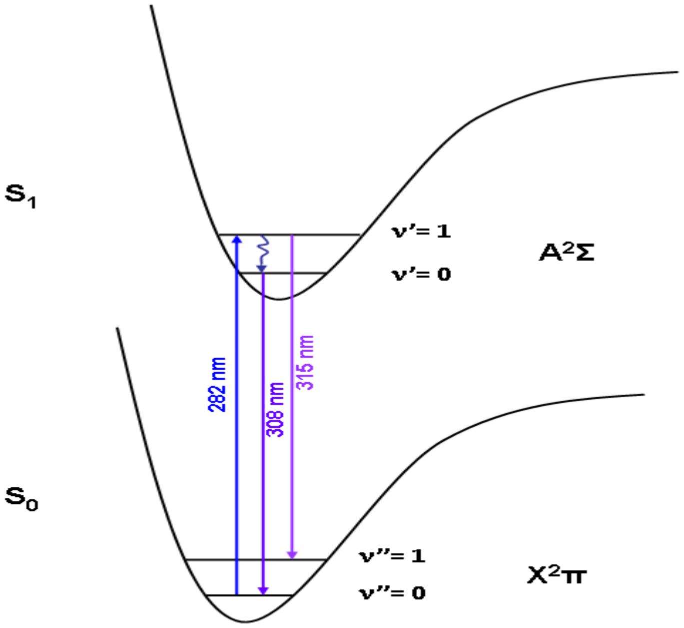

Figure 1. 2: The laser induced fluorescence process of OH radicals excited using 282 nm [29]

The intensity of the observed fluorescence signal depends on various parameters such as laser intensity (I_{laser}), concentration of the absorbing species ([OH]), absorption cross section of the absorbing species (σ), the fluorescence quantum yield (θ) and the light collection efficiency (G).

$$I_{LIF} \propto G\theta\sigma[OH] \times I_{laser} \quad (E\ 1)$$

The fluorescence quantum yield (θ) is defined as the ratio of number of photons emitted to the total number of photons absorbed. It can also be defined as a ratio of the rate constants for spontaneous emission process (k_A) to the sum of all processes such as spontaneous emission (k_A), quenching (k_Q) and other non radiative relaxation processes (k_{Tloss}) as shown below.

$$\theta = \frac{k_A}{\left[k_A + k_Q + k_{T_{loss}}\right]} \qquad (E\ 2)$$

LIF is most commonly used as a relative techniques as quantification of all the loss processes requires a very detailed knowledge of each process in presence of a given reaction mixture. However, LIF technique is highly sensitive (detection limit: 10^6-10^7 molecules cm^{-3}).

1.3.2 Cavity Ring-Down spectroscopy (CRDS) technique

The cavity ring-down spectrometer consist of a cavity formed by two highly reflective mirrors (99.9967%) which allows trapping light inside the cavity. The small fraction of the light that leaks out of the cavity at each round trip, is measured. The CRDS technique was pioneered by O'Keefe and Deacon in 1988 [31] which made use of a pulsed laser source. The use of a continuous wave cavity ring down spectrometer (cw-CRDS) was later demonstrated by Romanini in 1997 [32, 33]. In the present study, cw–CRDS technique coupled to laser photolysis system has been used to detect HO_2 radicals. Hence the present discussion will be restricted to cw-CRDS technique.

1.3.2.1 Optical cavity and cavity modes

An optical cavity (resonator) consists of an arrangement of optical mirrors that allows trapping light inside the cavity. The present CRDS system makes use of a linear cavity (standing wave cavity) in which the light propagating between the two reflective mirrors interferes with each other to form a standing wave pattern for certain resonance frequencies. The standing wave patterns of a stable cavity have certain electric field amplitude distributions which are self consistent during the propagation of the wave. These are called cavity modes: the transverse cavity modes differ in frequency while the longitudinal modes differ for different frequencies and have different intensity patterns across the cross section of the beam. The intensity distribution of the transverse modes has "n" nodes in the horizontal direction and "m" nodes in the vertical direction. If m=n=0, then the simplest among the intensity distribution obtained under this condition has a Gaussian profile and hence called as a Gaussian mode or fundamental mode and has the highest intensity (TEM_{00}). The frequency difference between two fundamental modes is called as the Free Spectral Range (FSR).

When the cavity length is an integral multiple of half wavelength, the light inside the cavity undergoes constructive interference and the light intensity inside the cavity builds up.

$$\boldsymbol{L = n\left(\frac{\lambda}{2}\right)} \qquad \textbf{(E 3)}$$

In other words, when the above criterion is satisfied, at least one of the cavity modes comes in resonance with the wavelength of light emission.

1.3.2.2 The CRDS equation

Since the light travels many times between the two reflective mirrors, it leads to an absorption path length of several kilometers using a short cavity length. This makes CRDS a very sensitive technique. Each time the light undergoes reflection at each mirrors surface, a small fraction of the light leaks out of the cavity, which is measured using a photodiode. In contrast to the typical absorption spectroscopy, a CRDS spectrometer measures the time taken by the light to decay out of the cavity which eliminates the errors due to source intensity fluctuations. The time taken by the light to decay to 1/e of the original value is called “ring-down time (τ)”. The ring-down times of an empty cavity (τ_0) and of a cavity with an absorbing species (τ_{abs}) are given as:

$$\boldsymbol{\tau_0 = \frac{L}{c(1-R)}} \qquad \textit{(E 4)}$$

$$\boldsymbol{\tau_{abs} = \frac{L}{c\{(1-R)+\sigma N l)\}}} \qquad \textit{(E 5)}$$

where L= cavity length, $\boldsymbol{l}$ = absorption path length, R = mirror reflectivity, N= concentration of the absorbing species in molecules cm^{-3}, σ = absorption cross section in cm^{-2} and c = velocity of light.

The absorption coefficient (α) is related to the absorption cross section and the concentration of the absorbing species by the Beer-Lamberts law as:

$$\boldsymbol{\alpha = N \times \sigma} \qquad \textit{(E 6)}$$

Using equation E3, E4 and E5, the absorption coefficient can be calculated by measuring the ring-down times of the cavity in absence and in presence of the absorbing species (τ_0) and (τ_{abs}) respectively as shown below:

$$\boldsymbol{\alpha = N \times \sigma = \frac{R_l}{c}\left[\frac{1}{\tau_{abs}} - \frac{1}{\tau_0}\right]} \qquad \textit{(E 7)}$$

where, (R_l) represents the ratio of cavity length (L) to the absorption path length (l). Hence, if the absorption cross section of the absorbing species at a fixed wavelength is known, then by measuring (τ_0) and (τ_{abs}) the concentration of the absorbing species can be obtained from the above equation or vice versa. Since, the cavity ring-down spectroscopy deals with measurement of ring-down times which is independent of the source intensity fluctuations, this allows measuring the absolute concentration of an absorbing species [31].

1.3.2.3 Continuous wave cavity ring-down spectroscopy (cw-CRDS)

As mentioned earlier, the classical CRDS made use of a pulsed laser source. The experimental system even though easier to build suffered from low sensitivity and selectivity. Since the duration of the pulsed laser is longer than the cavity round trip time, the electric fields within the cavity superpose themselves and the broad spectral width of the pulsed laser (low selectivity) simultaneously excites several modes within the cavity (low sensitivity) of the measurement. The simultaneous excitation of several transverse cavity modes leads to multi exponential decay of the ring-down event [34].

The classical CRDS system underwent a lot of modifications in the late nineties and the use of a continuous light source became more possible [33, 35]. The advantage is that the bandwidth of cw-laser is generally narrower than the bandwidth of pulsed laser, which makes high resolution spectroscopy possible: this is an important point for our goal, since HO_2 radicals have relatively narrow absorption features. Another advantage of cw-CRDS compared to pulsed CRDS is, that cw-laser are generally much cheaper and smaller than pulsed laser. However, in order to measure the leaking of light out of the cavity when using a cw-laser, an artifice has to be used to switch of the laser light once a mode has been excited: in our system, this is done by use of an Acousto Optic Modulator (AOM) which acts as optical switch by deviating the source of radiation once the cavity comes into resonance with the wavelength of laser emission in order to measure the ring down event. Since the band width of a continuous laser is narrower than the FSR (in contrast to pulsed lasers, where the bandwidth is generally broader than the FSR (see Figure 1. 3 below) and thus some photons are always in resonance with a cavity mode), the resonance with the cavity modes needs to be actively achieved: this can be done by either changing the cavity length or the wavelength of source emission.

In most studies, the wavelength of source emission is restricted to the detection wavelength of the absorbing species under investigation and hence the modulation of the cavity length is the only option to bring the cavity into resonance with laser wavelength. This is achieved by placing one of the cavity mirrors onto a piezo electric transducer which periodically modulates the cavity length when an external voltage is applied to it. Light builds up inside the cavity through constructive interference when resonance is achieved, which also results in an increase in the light leaking out of the cavity. When this light intensity, detected by the photo-diode, reaches a user-preset value, a signal is send to the AOM so it deviates the laser beam and hence the light trapped within the cavity is allowed to decay. The time taken by the light to decay from the empty cavity and in presence of the absorbing species is then measured and by knowing the absorption cross section of the absorbing species at a fixed wavelength, the absolute concentration of the absorbing species is obtained as already explained in section 1.3.2.2. An approximate comparison between the band width of laser emission and the transverse cavity modes of an optical cavity is shown in Figure 1. 3

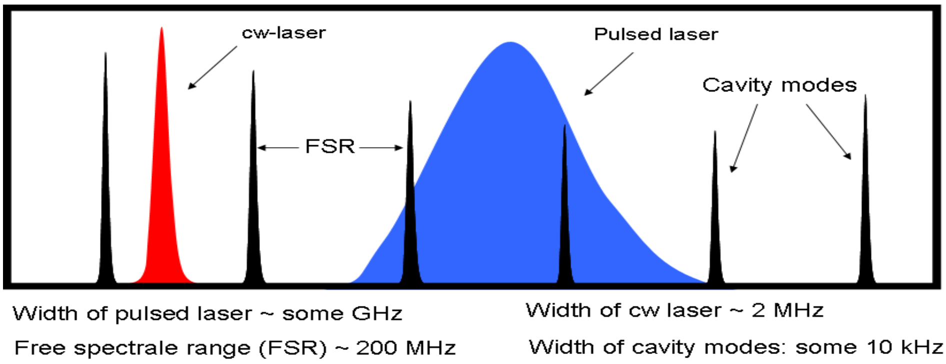

Figure 1. 3: An approximate comparison between band width of laser emission of a cw-laser and a pulsed laser with the cavity mode[29] .

The measurement strategy in case of cw-CRDS even though very complex, it allows higher sensitivity. During the course of this thesis, the cw- cavity ring-down spectrometer has been used to detect the OH stretching overtone of HO_2 radicals in the near IR region at around 6638.20 cm^{-1} as well as to quantify formaldehyde at 6624.779 cm^{-1}

1.3.3 UV absorption spectroscopy

UV absorption spectroscopy has been used over the years for detection and quantification of many organic compounds such as carbonyls, alkanes, alkenes, aromatics etc. In many of these organic compounds, the energy separation between the bonding, anti-bonding and non-bonding molecular orbitals, corresponds to the energy of light photons in the UV region. When such compounds are irradiated with a broad spectrum of UV radiation, those wavelengths which match certain electronic transitions in the organic compounds are absorbed while the rest are transmitted. The most frequently observed transitions that occur on absorption of UV radiation are those in which the electrons from the Highest Occupied Molecular Orbital (HOMO) are excited to the lowest unoccupied molecular orbital (LUMO). An example of the type of the transitions observed depending on the type of the chromospheres or the excitation energy [36, 37] is shown below:

$\sigma \rightarrow \sigma^*$	150 nm
$\sigma \rightarrow \Pi^*$	170 nm
$\Pi \rightarrow \Pi^*$	180 nm
$n \rightarrow \sigma^*$	190 nm
$n \rightarrow \Pi^*$	300 nm

Depending on the type of the chromophores present in the organic compounds, a single or a combination of the above transitions could occur and hence it might be possible to distinguish different organic species based on their UV absorption spectrum.

In case of aromatic compounds presence of a conjugated Π electron system in the aromatic ring gives characteristic absorptions that correspond to the presence of a benzene ring in unknown compounds. Depending on the type of substituent groups (electron donating or electron withdrawing); the absorption patterns are shifted in wavelength. Hence the shift/change in the spectrum can be used to identify the type of the substituent group on the aromatic ring produced in a typical reaction as shown below:

Aromatic + OH → Aromatic-OH adduct

However, these absorption patters are quite complex than can be explained by the simple $\Pi \rightarrow \Pi^*$ or $n \rightarrow \Pi^*$ transitions and more detailed quantum chemical calculations using computational tools are used to understand the type of the transitions. These computational studies are out of the scope of the present discussion.

Unlike the IR spectroscopy where transitions between individual vibrational or rotational states can be resolved as individual peaks, UV spectroscopy tends to provide wide, overlapping absorption bands over a range of wavelength. The reason for these broad absorption bands is that the energy levels of the ground and the excited state of a molecule are subdivided into vibrational and rotational energy levels and the electronic transitions could occurs from anyone of these sublevels of the electronic ground state to any of the sublevels of the electronic excited states. Due to a small difference in the energy of the various transitions, their wavelength of absorption also differs only slightly and can generally not be resolved and hence broad absorption band spectra are observed. Hence UV spectroscopy is largely non-selective. However, under certain experimental conditions, where the absorbing species under investigation is well separated in wavelength in a given absorbing mixture, than by restricting the light detection to a specific wavelength using a monochromator, time resolved UV spectrometer can be used efficiently to detect and monitor the concentration of the absorbing species. During the course of this thesis, time resolved UV absorption spectroscopy has been used to detect and monitor the reaction kinetics of the HMB-OH adduct.

As already explained, when organic molecules are irradiated with UV radiation, those wavelengths that correspond to certain electronic transitions in the molecules are absorbed by while the rest are transmitted. A UV spectrometer measures the intensity of the transmitted light in presence and in absence of the absorbing species. The Beer- lamberts law relates the ratio of the Incident intensity (I_0) / transmitted intensity (I_t) to the concentration of the absorbing species as follows:

$$\boldsymbol{ln\left(\frac{I_0}{I_t}\right) = \sigma \times C \times l} \quad \textit{(E 8)}$$

where $\boldsymbol{\sigma}$ = absorption cross section in cm^2, **C** = concentration in molecules cm^{-3} and $\boldsymbol{l}$ = absorbing path length in cm.

Knowing the absorption cross section of the absorbing species, and measuring the I_0/I_t, at a fixed wavelength, the concentration of the absorbing species can be calculated. Since the UV measurements involve the measurement of light intensities (in contrast to CRDS measurements), the calculated concentrations are susceptible to intensity fluctuations of the incident radiation. In the present study, we intend to measure the UV spectrum of HMBOH adduct, it is important to know the exact concentration of hexamethylbenzene and OH radicals. The concentration of hexamethylbenzene can be directly obtained by measuring the absorbance and the known cross section of HMB at a given wavelength in the

UV region. However, in case of OH radicals it's not so straight forward. OH radicals are produced using 248 nm photolysis of H_2O_2. In order to quantify accurately the amount of OH produced on photolysis, the system needs to be calibrated. The system was calibrated with a well known ethyl peroxy calibration method before being implemented for the measurement of HMB-OH adduct spectrum and its decay kinetics. The details of the calibration procedure and HMB-OH spectrum measurement are discussed in detail in the experimental section of Chapter 2.

1.4 References

1. A. J. Haagen-Smit, C. E. Bradley, M. M. Fox: Ind. Eng. Chem. 45, 2086 (1953).

2. R.E Hester, R.M. Harrison, R.G. Derwent, Sources, distributions, and fates of VOCs in the atmosphere. Volatile Organic Compounds in the Atmosphere (2007).

3. A. Guenther,C. Geron, Pierce, B. Lamb, P. Harlez, R. Fall. Atmos. Environ. 34, 2205–2230 (2000).

4. A. Guenther, C. Hewitt, D. Erickson, R. Fall, C. Geron, T. Graedel, L. Klinger, T. Pierce, P. Zimmermann. J. Geophys. Res. 100, 8873–8892 (1995).

5. M. Placet, C. O. Mann, R. O. Gilbert, M. J. Niefer. Atmos. Environ. 34, 2183–2204 (2000).

6. R.F. Saywer, R.A. Harley, S.H. Cadle, J.M. Norbeck, R. Slott, H.A. Bravo, Atmospheric Environment. 34, 2161–2181 (2000).

7. J. H. Kroll, J. H. Seinfeld: Atmos. Environ. 42, 16, 3593 - 3624 (2008)

8. R. Atkinson, D.L. Baulch, R.A Cox, J.N. Crowley, R.F. Hampson, R.G. Hynes, M.E. Jenkin, M.J. Rossi, J. Atmos. Chem. Phys. 4, 1461 – 1738 (2004).

9. Barbara Finlayson-Pitts, J.J.N.P.: Atmospheric Chemistry: Fundamentals and Experimental Techniques.

10. J.G.Calvert, R. Atkinson, H.Karl. Becker, R. M. Kamens, H. J. Seinfeld, T. Wallington, G. Yarwood: The mechanism of Atmospheric oxidation of Aromatic hydrocarbons. (2002).

11. R. Atkinson, D.L. Baulch, R.A.Cox, J.N.Crowley, R.F Hampson, J.A.Kerr, M.J.Rossi, J.Troe: Atmos. Chem. Phys. 6, 3625–4055 (2006).

12. R. Atkinson, D.L Baulch, R.A Cox, J.N Crowley, R.F Hampson, R.G. Hynes, M.E.Jenkin, M.J.Rossi, J.Troe: J. Atmos. Chem. Phys. 4, 1461 – 1738 (2004).

13. R. Atkinson, D.L.Baulch, R.A.Cox, R.F.Hampson, J.A.Kerr, M.J.Rossi, J. Troe, J. Phys. Chem. 26, 1329 – 1499 (1997).

14. J.R. Hopkins, T. Still, S. Al-Haider, I.R.Fisher, A.C Lewis, , P.W. Seakins. Atmos. Environ. 37, 2557–2565.

15. Q. Fan, P.K Dasgupta, Anal. Chem. 66, 551–556 (1994).

16. Dingle, P. Franklin, Indoor and Build Environment. 3, 111–116 (2002).

17. California Air: Acetaldehyde as a toxic air contaminant. part A. Exposure assesment. California Environmental Protection Agency, Air resource board, Stationary source division.

18. E. Viskari, M. Vartiainen, P. Pasanen. Atmos. Environ. 34, 917–923 (2000).

19. Z. Polkowska, K. Skarzynska, T. Gorecki, J. Namiesnik. Journal of Atmospheric Chemistry. 53, 211–236.

20. A. Vlasenko, A.M. Macdonald, S.J. Sjostedt, J.P.D. Abbatt. Atmos. Meas. Tech. 3, 1055–1062 (2010).

21. J.M. Roberts, Atmospheric Environment. Part A. General Topics. 24, 243–287 (1990).

22. EPA: Chemical summary for acetaldehyde,. Office of Pollution Prevention and Toxics (1994).

23. A.J. Winters, M.A. Adams, T.M. Bleby, H. Rennenberg, , D. Steigner, R. Steinbrecher, J.Kreuzwieser, Atmospheric Environment. 43, 3035–3043 (2009).

24. S. Rottenberger, B. Kleiss, U.Kuhn, A. Wolf, M.T.F. Piedade, W. J Kesselmeier, J. Biogeosciences. 5, 1085–1100 (2008).

25. D.B. Millet, , A.Guenther, D.A. Siegel, N.B.Nelson, H.B. Singh, J.A.Gouw, C. Warneke, J.Williams, G.Eerdekens, V.Sinha, T.Karl, F Flocke, E. Apel, D.D.Riemer, P.I. Palmer, M. Barkley, Atmospheric Chemistry and Physics Discussions. 9, 24225–24279 (2009).

26. T.E. Graedel, Chemical compounds in the atmosphere, New york: Academic Press. (1978).

27. S.A. Edgerton, J.Shah, J. Expos. Anal. Environ. Epidemiol. 2, 109–115 (1992).

28. Thiebaud: Dévelopment d'un spéctromèter c cavité optique de haute finesse couplé é la photolyse laser-Measures spectroscopique et cinétiques du radical HO2, Thesis submitted to Université Lille 1- Sciences et Technologies, (2007).

29. C. Jain: Laser photolysis coupled to detection by LIF and cw- CRDS: Application to spectroscopic and kinetic studies of OH, HO2 and HONO, Thesis submitted to Université Lille 1- Sciences et Technologies, (2011).

30. Wikipediacontributors:Fluorescence, http://en.wikipedia.org/w/index.php?title=Fluorescence&oldid=506248129, (2012).

31. A. O'Keefe, D.A.G Deacon, Review of Scientific Instruments. 59, 2544–2551 (1988).

32. D. Romanini, A. A. Kachanov, F. Stoeckel: Diode laser cavity ringdown spectroscopy. Chem. Phys. Lett. 270, 538– 545 (1997).

33. D. Romanini, A. A. Kachanov, N. Sadeghi, F. Stoeckel: Cw cavity ringdown spectroscopy. Chem. Phys. Lett. 316–322 (1997).

34. D. E. Vogler: Open-path and fiber-based cavity ring-down spectroscopy, Thesis submitted to Swiss Federal Institute Of Technology, (2005).

35. D. Romanini, A.A. Kachanov, N, Sadeghi, F. Stoeckel, Chem. Phys. Lett. 264, 316–322 (1997).

36. E.M. McCash, Fundamentals of molecular spectroscopy. Tata McGraw-Hill Publishing company, New Delhi.

37. G. Christain: Text book of analytical Chemistry. Wiley, New Delhi, India.

Chapter 2

Experimental techniques

2 Experimental Techniques

This chapter provides a detailed description of the instrumentation and the experimental techniques used for the entire work of this thesis. Chapter 2 is divided in to three sections. Section *2.1* deals with the simultaneous measurements of HO_2 and OH radicals using the laser photolysis coupled to Cavity Ring-down Spectroscopy (CRDS) and Laser Induced Fluorescence (LIF) techniques respectively, which were used to measure a) the absolute cross section of CH_2O in the near IR region and to investigate the equilibrium of $CH_2O + HO_2$ reaction (see Chapter 3) and b) the measurements of the quantum yields of HCO and H atoms from the 248 nm photolysis of Acetaldehyde (see chapter 4).

Section *2.2* of this chapter deals with the Discharge fast flow tube coupled to time of flight mass spectroscopy (TOF-MS) studies that were carried out in collaboration with J.C Loison for product determination of the OH initiated oxidation of HMB (see Chapter 5). Section *2.*3 describes the laser photolysis coupled to time resolved UV spectroscopic technique which was used to record the UV absorption spectrum of the HMB-OH adduct and its decay kinetics (more details in Chapter 5).

2.1 Laser photolysis coupled to cavity ring-down spectroscopy and laser induced fluorescence techniques

In this section the experimental setup employed to measure time resolved HO_2 and OH concentration profiles will be discussed. The experimental setup is divided into four main components: the photolysis cell, the photolysis laser, the cw-CRDS system and the LIF system. A detailed description of this set-up has already been given in a publication prior to this thesis [1]. A schematic view of the experimental setup is shown in Figure 2.1.

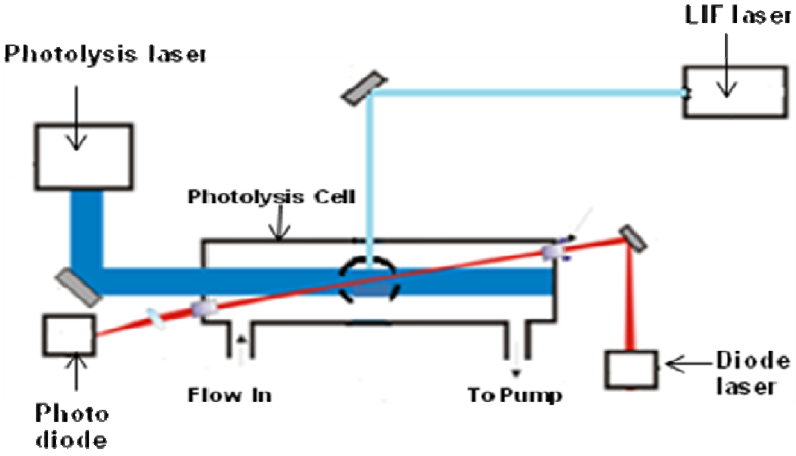

Figure 2.1: Schematic representation of the laser photolysis coupled to LIF and cw-CRDS setup

2.1.1 Photolysis Cell

The schematic representation of the photolysis cell is shown in Figure 2. 2. The photolysis cell is a three axis stainless steel cell with one long axis (78 cm) and two short axes (27 cm), internally coated with Teflon. The cell was constructed using six stainless steel tubes each with an internal diameter of 6 cm, connected along the three perpendicular axes that pass through a cubic central structure to form a three dimensional cross. The six end flange are designed in such a way that, besides fulfilling more specific functions detailed below, they seal the reactor. The X, Y and Z axis are used for the CRDS detection, LIF excitation and LIF detection, respectively.

The two flanges of the central axis (X axis) are modified in order to insert mirror holders within which the CRDS mirrors are placed. In addition to this, the flanges are equipped with quartz windows (diameter 3 cm) in the centre which allow the photolysis beam to enter the reactor.

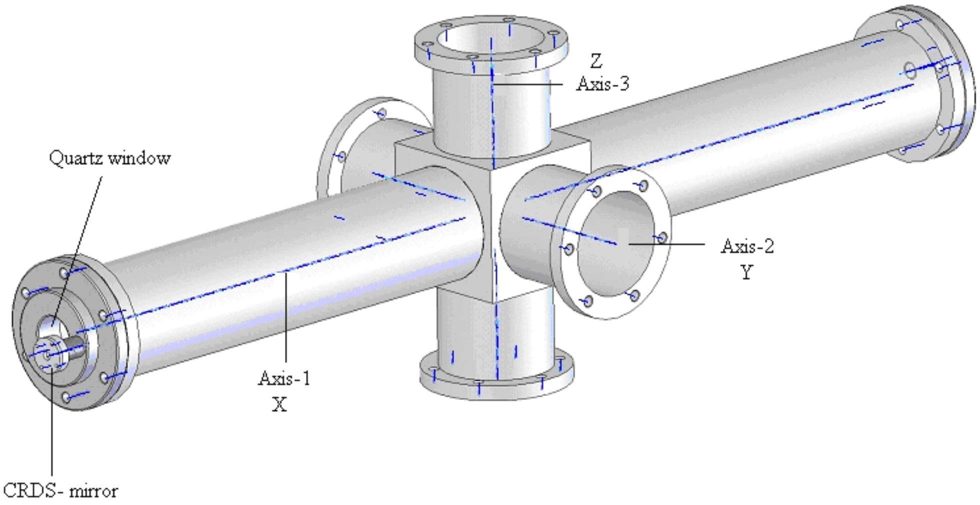

Figure 2. 2: Schematic representation of the reaction cell

The flange at one end of the horizontal short axis (Y axis) is designed to accommodate a thermocouple in order to measure the temperature of the gas mixture inside the reactor while the other flange contains a quartz window at the centre (diameter 2.5 cm) to allow the LIF excitation laser beam to enter into the photolysis cell.

The upper flange of the vertical short axis (z axis) is equipped with a quartz window (diameter 6 cm) in order to allow detecting the fluorescence photons. A system consisting of two lenses (Thor labs, focal length 75 mm) is mounted between the central cube of the cell and the above mentioned window in order to collect and focus the fluorescence signal onto the photo-cathode of the Photomultiplier tube (PMT), fixed to the upper flange. An interference filter mounted between the window and the PMT filters out all extraneous light (e.g. scattered light from the photolysis laser and the LIF excitation laser) and allows the light radiation in the wavelength range of 308 ± 5 nm to be detected by the PMT.

2.1.2 Photolysis laser

The photolysis is achieved by using a Kr-F excimer laser (Lambda Physik LPX 202i series). It consists of a cavity in which a desired mixture of Kr/F_2/He is filled. When a high voltage is applied to the gas mixture, the Kr and F_2 gets excited to higher energy states to form a meta stable Kr-F excimer molecule. This excimer emits 248 nm photons which stimulates the emission from the other Kr-F excimer molecules, resulting in laser action. The emitted laser beam had a pulse duration of ~ 10 ns, much shorter than the reaction time of the species of interest encountered in this work. The laser energy could be varied over a large range from 10 to 90 $mJcm^{-2}$.

2.1.3 The cavity ring down spectrometer

The cavity ring down spectrometer consists of a cavity formed by two highly reflective mirrors (R = 99.9967%, Los Gatos) mounted on a three-axis optical support with micrometric adjustment screws, which are used to align the mirrors *(X-Y-Z Newport U100-A series*). One of the cavity mirrors is mounted on a piezo-electric transducer (P-305.00, PI) in order to modulate the cavity length. The piezo-electric transducer used is a ceramic component which undergoes expansion or contraction when an external voltage is applied to it. Thus by applying a triangular voltage signal, the cavity length can be modulated periodically. This technique has been used to detect HO_2 radicals in the near infrared region, and the source of detection radiation is provided by a fibered, distributed feed-back (DFB) diode laser (Fitel-Furukawa FOL15DCWB-A81-W1509 DFB laser for 6635±12 cm^{-1} range) with an output power of ~20 - 25 mW. The diode laser emission passes through a fibred optical isolator followed by a fibered beam splitter which sends 1% of the DFB laser beam into a wavemeter (Burleigh WA-1100) with an accuracy of 0.01 cm^{-1} for monitoring the wavelength of the laser emission. The remaining 99% exit the fibre, passes an Acousto-Optic modulator (AOM) and is finally coupled into the cavity through a short focal length lens. This short focal length lens allows the DFB laser beam to be focused at the centre of the cavity for mode matching, so as to excite the fundamental TEM_{00} mode only.

The optical signal transmitted through the cavity is detected and converted into current by an avalanche photodiode (Perkin Elmer C30662E). An in-house designed amplifier-threshold circuit converts the current signal to an exploitable voltage signal and triggers the AOM to deviate the DFB laser beam when the cavity comes into resonance and the photodiode signal passes over a user defined threshold. The exponential decay of the light leaving the cavity following the deviation of the laser beam represents a "*ring down event*".

In order to simplify and optimise the event analysis, an in-house designed event filter switch is used. Both the photodiode signal and the AOM signal are connected to this filter. This event filter switch allows the photodiode signal to be recorded by the acquisition card only when the cavity is in resonance, i.e. when the AOM is in position to deviate the laser beam. The resulting signal is connected to a fast 16 bit analogue acquisition card (National Instruments PCI − 6259). The acquisition frequency is 1.25 MHz and thus the ring down signal is being sampled with a resolution of 800 ns. The data is transferred to a PC in real time via PCI bus. Details on this event filter can be found in [2]. The schematic representation of the cw-CRDS technique used in this work is as shown in the Figure 2. 3.

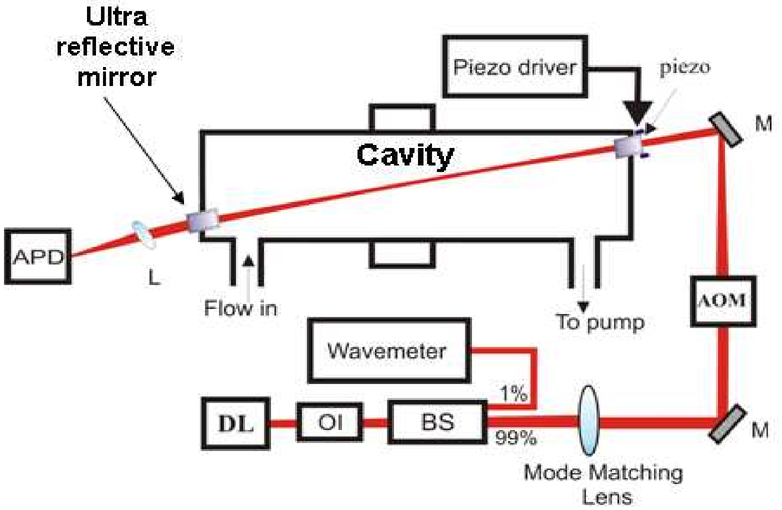

Figure 2. 3: Schematic representation of the CRDS technique. APD = Avalanche Photodiode, DL = Diode laser, OI = Optical isolator, BS = Beam splitter, AOM = Acousto – optical modulator, M = Mirror and L = Lens

2.1.4 The LIF system

The laser induced fluorescence technique has been used to detect OH radicals. This is achieved by exciting OH radicals from the ground vibrational level of the electronic ground state ($X^2\Pi$) to the first excited vibrational level of the first excited electronic state ($A^2\Sigma$) using photons around 282 nm. The rotational transition involved during the OH excitation process is Q1 (4.5) (*Hunds case "a"*) at 282.438 nm. The red shifted fluorescence at 308 nm was detected using a PMT. The 282.438 nm photons were generated by frequency doubling the output of a dye laser (PrecisionScan PRSC-24-HPR, Sirah Laser) pumped by the frequency doubled output of a Nd: YVO4 laser (Spectra Physics Navigator II YHP40-532QW), operated at 10 kHz, producing an average output power of 26 mW in the UV. The fluorescence signal was collected perpendicular to the laser beam and focused on to the photocathode of the PMT using a lens system and interference filter (308 ±5). The electrical signal generated by the PMT is sent to a Boxcar integrator and transferred to a data acquisition card. Since the OH fluorescence decays under the experimental conditions of this work within a few hundred nano seconds, the position and the length of the acquisition gate of the boxcar integrator is adjusted such as to record a maximum of the fluorescence signal without acquiring stray light from the excitation laser pulse.

2.1.5 The Etalon

The LIF excitation laser (PrecisionScan PRSC-24-HPR, Sirah Laser) used in this study suffered from a rapid wavelength drift, resulting in a change of the LIF laser intensity due to the change of the excitation wavelength. In order to lock the LIF laser at the OH excitation wavelength (282.438 nm), a temperature controlled etalon was build during the course of this thesis. The schematic representation of the temperature controlled etalon is shown in Figure 2. 4. The LIF laser beam passes through a 6.3 mm thick window which allows most of the light to pass through while ~4% of the incident light gets reflected. The incident light is reflected twice (~2% each reflection), once from the front surface and then from the back surface of the window. The window is thick enough to have the two reflections geometrically well separated. This allows aligning one of the reflected beams onto the photodiode1 (called laser photodiode) to measure the power of the excitation laser, while the second reflected beam is aligned on to the etalon using a quartz prism as shown in Figure 2. 4.

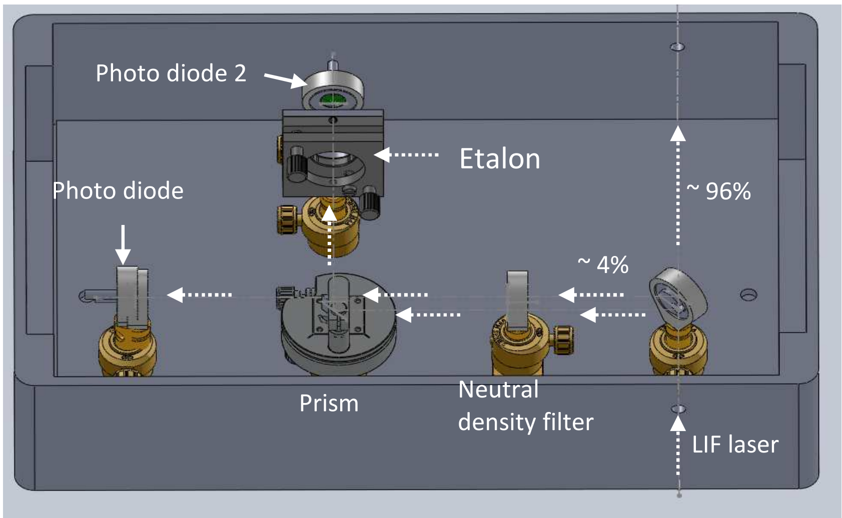

Figure 2. 4: Schematic representation of the temperature controlled etalon system

A Fabry- Pérot etalon typically consists of a transparent plate with two reflecting surfaces and can hence be considered as a cavity. The name "Etalon" is derived from the French "*étalon*" which means "measuring gauge" or "standard". When the light beam enters the etalon at an angle (θ), it undergoes multiple internal reflections as shown in Figure 2. 5.

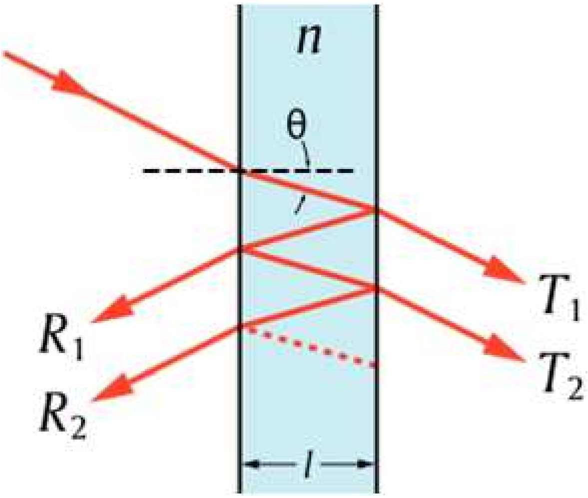

Figure 2. 5: The working principle of the Fabry – Pérot etalon [3]

The transmission of light from etalon depends on the type of the light interference occurring inside the cavity: when the constructive interference of the light occurs, i.e., it results in high transmission peaks (transmission maxima: T_{max} in Figure 2. 6). If destructive interference of light occurs inside the cavity than the transmitted light corresponds to a transmission minimum. Whether the reflections inside the etalon are in phase or not, depends on the wavelength of the light (**λ**) in vacuum, the angle (**θ**) at which light travels through the etalon, the distance between the two reflecting surfaces (***l***) and the reflective index of the material between the reflecting surfaces (***n***). The resultant spatial distribution of the transmitted light intensity will have a fringe pattern formed by bright and dark rings which correspond to the transmission maximum and minimum respectively.

However, with the etalon built during the course of this thesis (thickness = 1 cm and finesse > 10) the beam is aligned perpendicular to the etalon and hence no fringe pattern is produced by the etalon. Instead, the beam is reflected back and forth between the two reflecting surfaces and the intensity of the exiting beam depends on whether they undergo constructive or destructive interference. The wavelength separation between two adjacent transmission peaks is called the Free Spectral Range (FSR) as shown in Figure 2. 6. The position of the transmission peaks is strongly linked to the distance between the two reflecting surfaces, i.e. the thickness of the etalon. Since the thickness is a function of the temperature, the position of the transmission maxima for a given wavelength (in our case the excitation wavelength for OH-radicals) can be controlled by precisely controlling the temperature of the etalon. Therefore, the Fabry-Pérot etalon is placed inside a temperature controlled enclosure whose temperature is controlled to ~0.1K using a temperature stabilization servoloop system.

In practice, the etalon is exploited for stabilising the emission of the dye laser onto the excitation wavelength for OH-radicals as follows: first, the laser is tuned to the peak of the OH-absorption line by measuring the fluorescence intensity. Then, the temperature of the etalon is adjusted in such a way, that the transmission through the etalon is placed on the centre of a slope of a transmission peak (position **P1** marked in Figure 2. 6). Thereafter, the temperature of the etalon is kept constant. Doing so, any drift in the excitation laser wavelength results in a decrease or increase of the transmitted light intensity due to a shift in the position of the transmission peaks which in turn results in a change in position **P1**. Adjusting the temperature of the etalon in a way such that the wavelength corresponding to the peak of the OH-absorption line is positioned at **P1**, has two advantages: the one is that the change in transmitted intensity is maximal, and the other is that it is possible to determine in which direction (shorter or longer wavelength) the laser has drifted, depending on either increase or decrease of the transmitted intensity. A program written in Labview then readjusts the laser wavelength depending on the direction of the change in the position P1.

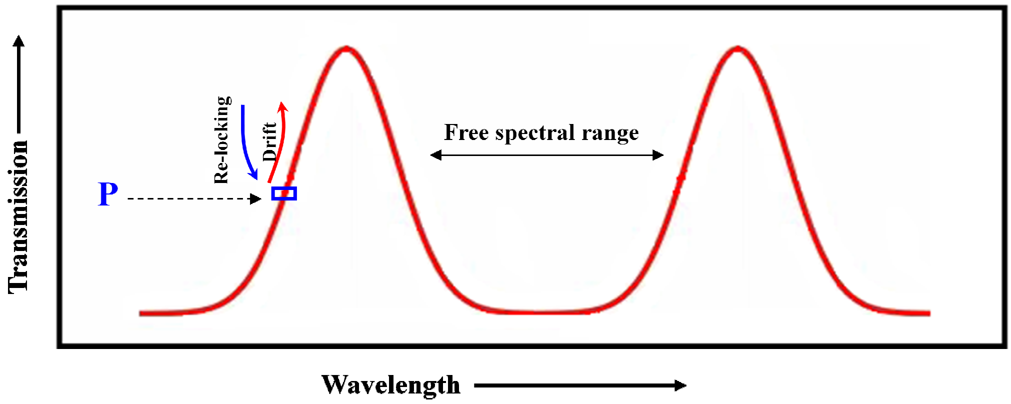

Figure 2. 6: Locking of the LIF laser using the temperature controlled etalon

Application of the experimental set up for kinetic and spectroscopic measurements

This experimental setup finds its application in two distinct but equally important areas of research, i.e. gas kinetics and spectroscopy. The kinetic application in this thesis is focused on the measurements of the time resolved kinetics of OH and HO_2 radicals, whereas the spectroscopic application is mainly used to record the absorption spectra of some species either in a continuous mode for stable species or in a pulsed mode (using pulsed photolysis) for transient species.

2.1.6 Kinetic application: time resolved measurement of OH and HO_2 radicals

A schematic representation of the experimental system used for simultaneous, time resolved measurements of OH and HO_2 radicals is shown in

Figure 2. 7. A complete description of the experimental setup and its validation for kinetic applications has already been published in [1] prior to this thesis. The synchronisation of the LIF and CRDS techniques and measurement timing strategies are achieved by using two different delay generators (DG1 and DG2). The master timing unit here is DG1 as it performs two important functions. Firstly, it controls the repetition rate of the LIF excitation laser by continuously sending trigger pulses at a repetition rate of 10 kHz to the LIF excitation laser, leading to a time resolution of 100 μs for the OH concentration profile.

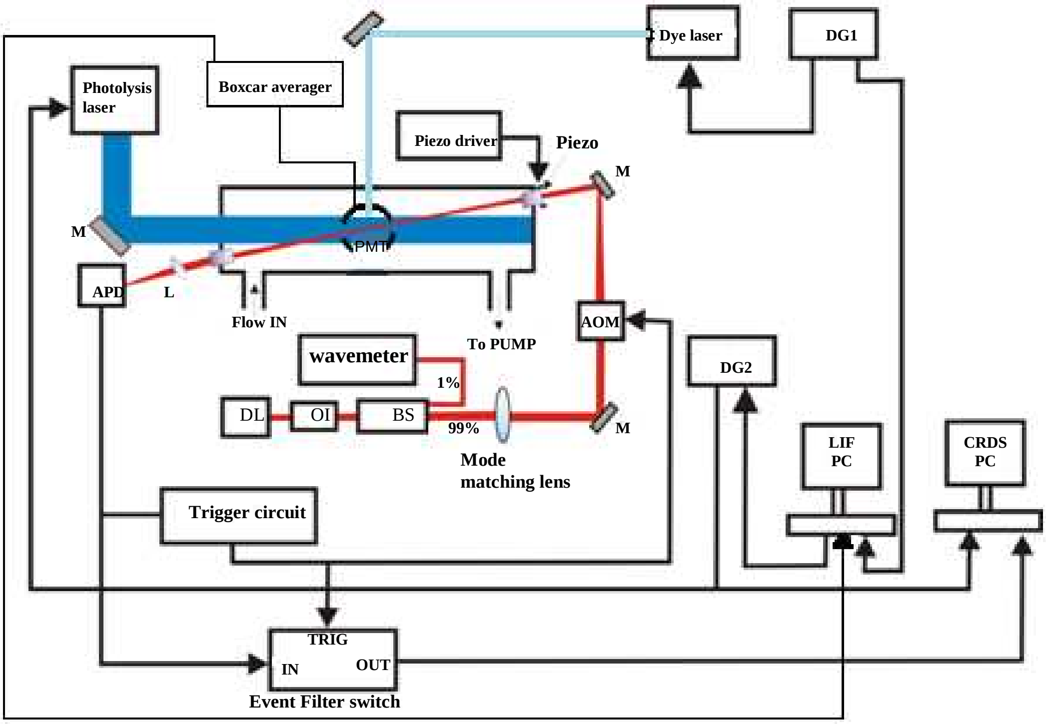

Figure 2. 7: Schematic representation of the experimental setup used for the simultaneous measurement of OH and HO_2 radicals. DG = Delay generator, APD = Avalanche Photodiode, DL = Diode laser, OI = Optical isolator, BS = Beam splitter, AOM = Acousto – optical modulator, M = Mirror and L = Lens

DG1 also triggers DG2, which subsequently triggers the photolysis laser as well as the CRDS acquisition procedure. The CRDS acquisition procedure is triggered immediately while the photolysis laser is triggered after a given delay. This allows measuring the baseline, i.e. to obtain some ring down events before the photolysis process. The DG2 receives pulses at a rate of 10 kHz from DG1; however the photolysis rate is of the order of 1Hz or less. In order to decrease the repetition rate of DG2's trigger cycle, a dummy delay of 1s or more (depending on the photolysis rate) is set on an unused output channel of DG2. In this way, DG2 considers only a new trigger pulse from DG1 once the delays of all output channels have been fulfilled. Hence the position of the photolysis laser pulse with respect to both the start of the data acquisition time and the LIF excitation pulse is known.

Since the occurrence of the photolysis laser pulse with respect to the start of the data acquisition window is known, ring down events are continuously acquired during the entire kinetic measurement period and the delay of each ring down event relative to the photolysis laser pulse can be calculated from its position within the acquisition time window. This way, for each photolysis pulse, a variable number of ring down events occurring at random, but well determined delays with respect to the photolysis laser pulse are recorded. Ring down events are recorded for multiple photolysis laser pulses (generally 50 - 100) until ring-down events are obtained in the entire time window.

The ring down time τ of each individual event is obtained in a two-step process. Firstly, the ring down time is estimated by linear regression of the logarithm of the first 20 μs of the decay in order to obtain a rough guess of the ring-down time. In the second step, the decay is now fitted in a time window corresponding to seven previously determined ring-down times using a Levenberg – Marquardt exponential fit [4] integrated into the main Labview program. The timing strategy and the synchronization between LIF and the CRDS system is shown in Figure 2. 8. The averaging time of both the HO_2 and the OH signals depend on the signal to noise ratio which in turn depends on the experimental conditions.

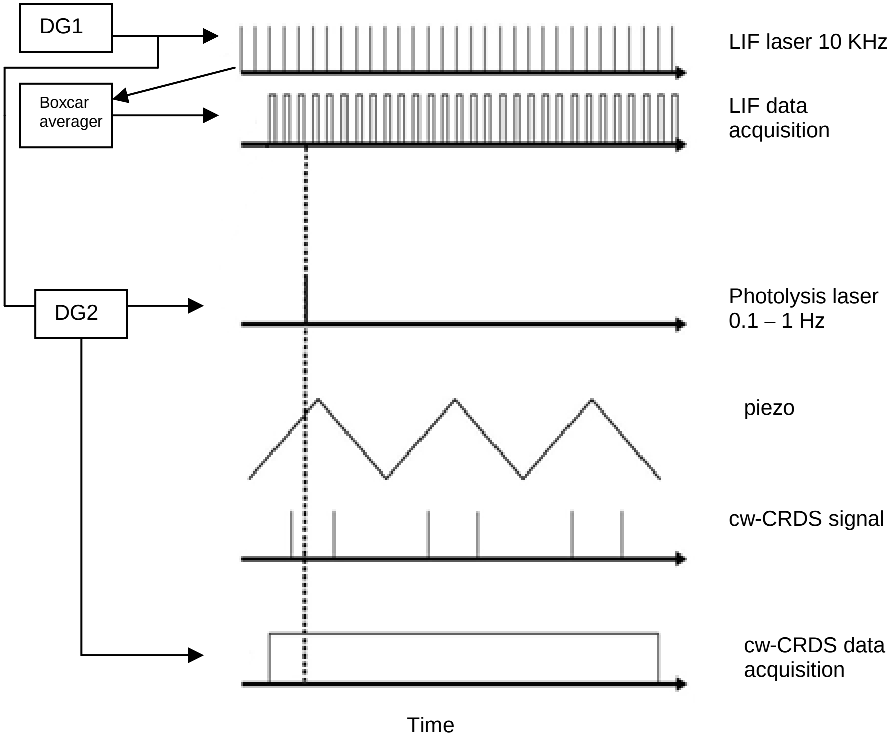

Figure 2. 8: Schematic representation of the timing strategy and the synchronisation of the LIF and CRDS system.

2.1.7 Spectroscopic application: Measurement of spectra of stable species.

The measurement strategy used is as follows. The concentration of the absorbing species is maintained throughout the measurement period by flowing well defined gas flows through calibrated flow meters into the reactor. Typically, 50 ring-down events have been averaged before the cw-CRDS diode laser was tuned to the next wavenumber in order to record the spectrum. The wave number of the DFB diode laser emission is slowly varied in the region of interest by applying a desired voltage in small increments to the laser diode controller unit using the data acquisition card via a Labview program. The precision of the wavemeter was limited to ±0.01 cm^{-1} whereas in most spectroscopic measurements a higher resolution is desired. Therefore the wave number from the wavemeter is recorded only for every tenth increment of 0.001 cm^{-1} as desired for a given measurement. Hence the wavenumber is measured in 10 times larger increments than the individual data points. Two data files are therefore obtained: the first contains the ring-down times τ as a function of the voltage applied to the diode laser controller (these files have the extension time_volt_rd), the second file contains the wavenumber as a function of the voltage and contains 10 times less data pairs than the first file: this file has the extension time_volt_wn. At the end of the data acquisition, all data points from the second file are fitted to a polynomial leading to a mathematical relation between voltage and wavenumber. This relation is than applied to each individual data from the first file in order to obtain a more precise wavenumber: this data-treatment is integrated in a Labview passed program named "Kinetic Analyser". The schematic representation of this continuous spectrum measurements strategy is shown in

Figure 2. 9.

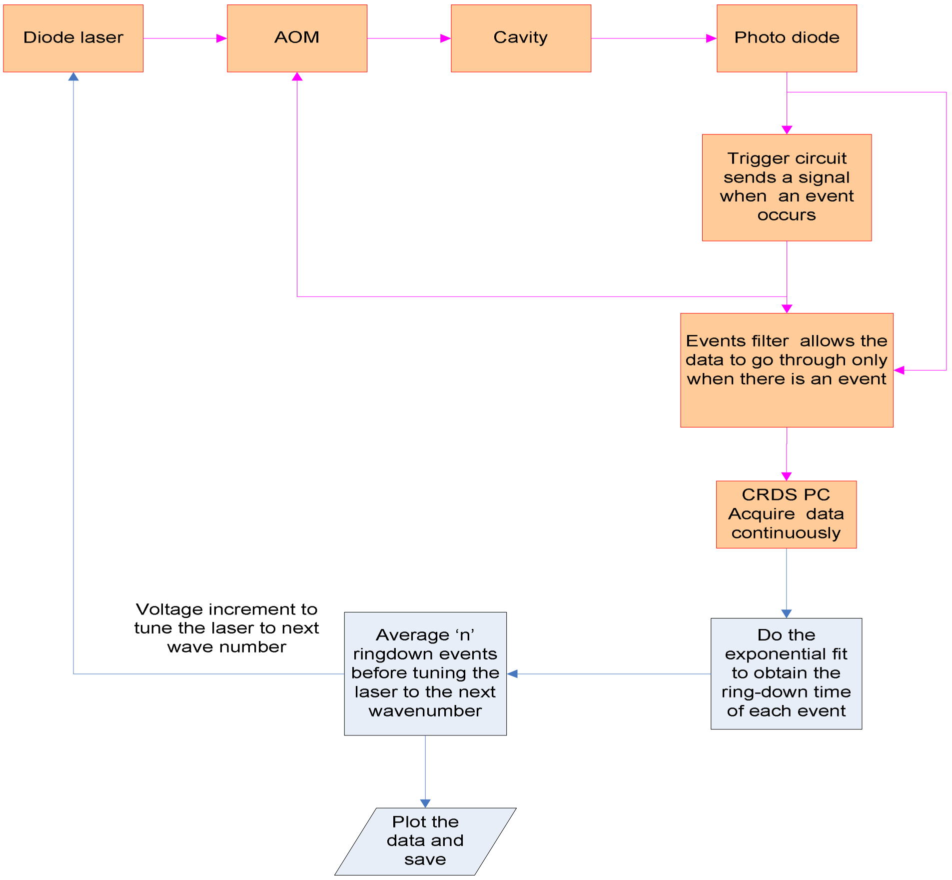

Figure 2. 9: Measurement strategy flow diagram for measuring the absorption spectra of stable species [5].

2.2 Discharge fast flow tube coupled to Time Of Flight Mass Spectrometer (TOF-MS)

The discharge fast flow tube coupled to Time of Flight- mass spectrometer used in this work was developed by J.C Loison [6] to investigate the reaction kinetics both of atmospheric as well as interstellar interest. The schematic representation of the experimental set-up is as shown in Figure 2. 10

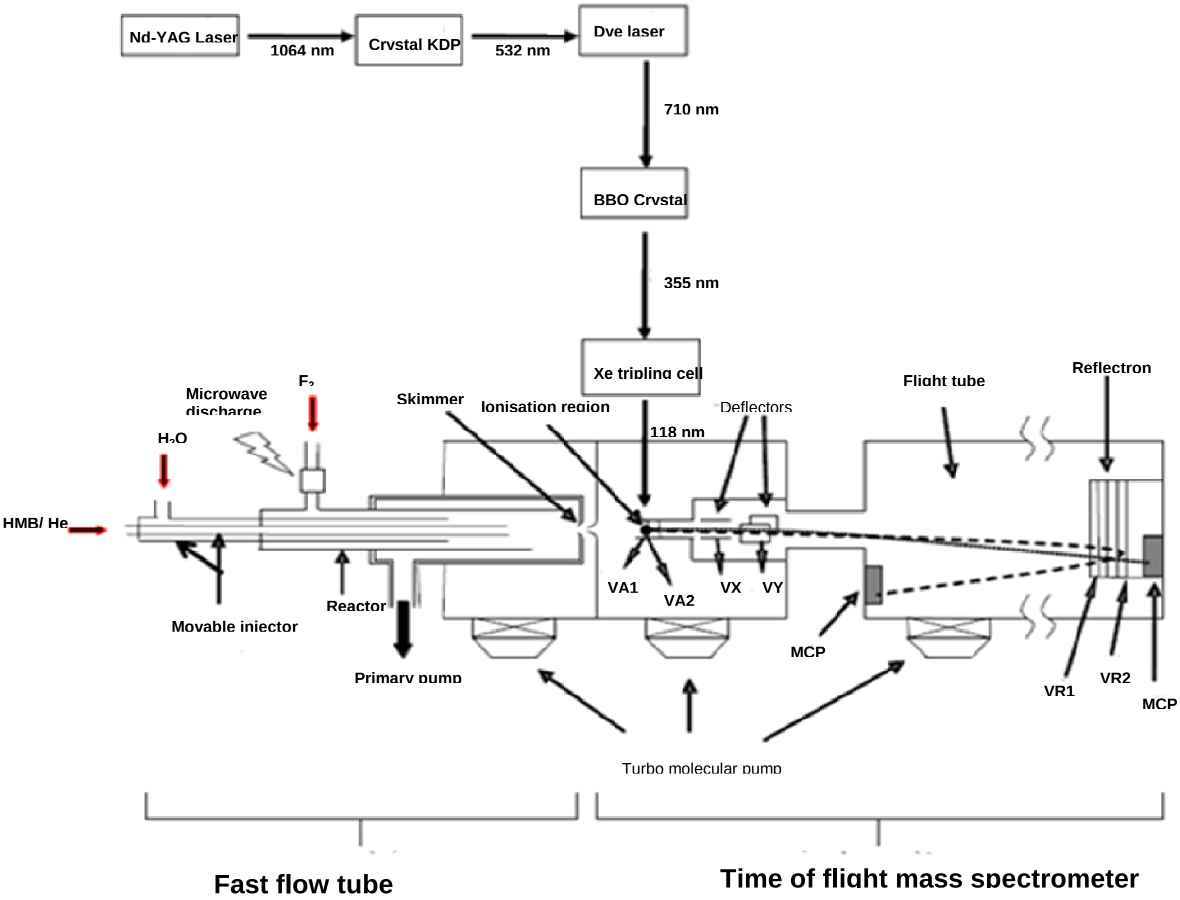

Figure 2. 10: Schematic representation of the discharge fast flow tube coupled to Time of flight mass spectrometer (TOF)

The experimental setup can be divided into two parts 1) Fast flow tube reactor and 2) Time of flight mass spectrometer.

2.2.1 The fast flow tube reactor

The fast flow reactor comprises of a 24 mm inside diameter/65 cm long quartz tube, inside which a sliding movable injector is mounted. The injector is a 6 mm inside diameter/90 cm long glass tube. The reactor is fitted out with three gas inlets allowing direct injection of various reactants which reduces the importance of recombination reactions at the reactant level.

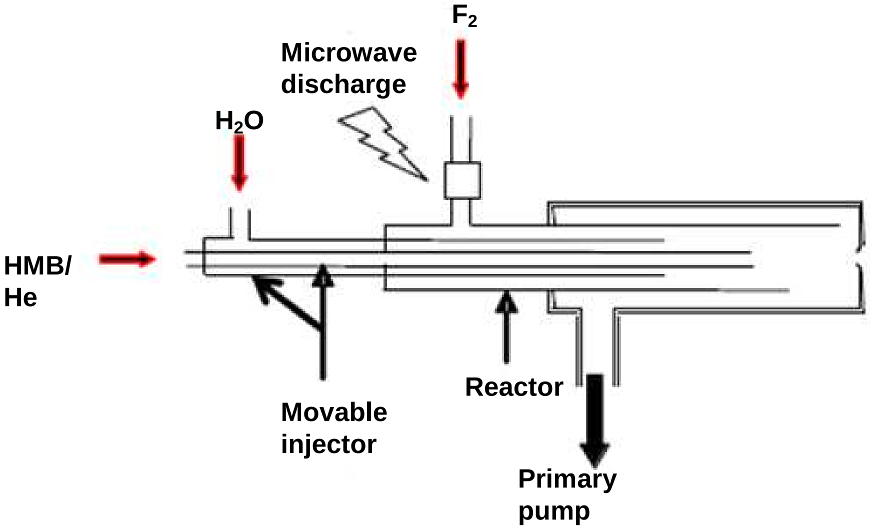

Figure 2. 11: Schematic representation of the fast flow tube reactor

2.2.2 Characterization of the flow

In order to understand the type of the gas flow that flows in the flow tube reactor, one must calculate the Knundsen number (kn) and the Reynolds number (Ne). Knundsen number is a dimensionless number that determines whether the gas flow is viscous or molecular. If the Kn <0.01, it means that the gas flow is viscous and the intermolecular interactions between the gas molecules dominate. If the gas flow is molecular (Kn> 10), than it represents a steady state where each gas particle moves independent of the other.

The Knudsen Number is defined as:

$$K_n = \frac{\Lambda}{L_r} \qquad E\ 1$$

Where ,

Λ = The mean free path travelled by the gas particle (cm)

L_r = The internal diameter of the reactor (cm)

Here the molecules are treated as spheres between which there is no interaction. The mean free path (Λ) travelled by the gas molecule is given as:

$$\boldsymbol{\Lambda} = \frac{1}{\sqrt{2}} \times \frac{1}{(\pi N d^2)} \qquad \textbf{E 2}$$

Where,

N = The number of molecules per cm^3

d = The diameter of the molecule in cm.

Since in this study the experiments were carried out using He as the bath gas ($d = 2.18 \times 10^{-8}$ cm) in the pressure range of 1 – 3 Torr ($3.26 \times 10^{16} < N < 9.7 \times 10^{16}$ molecules cm^{-3}), the calculated value of kn = 0.006, which means that the flow in the reactor is viscous flow.

Reynolds Number (Re), is a dimensionless number that determines whether the viscous flow is laminar or turbulant. If Re < 1000, than the viscous flow in the reactor is laminar and if the Re > 1000, the viscous flow in the reactor is turbulant [7].

The Reynolds number is defined as:

$$R_e = \frac{(\rho\, D\, V_e\,)}{\mu} \qquad \textbf{E 3}$$

Where,

ρ is the gas density (g cm^{-3})

V_e is the speed of gas flow (cm s^{-1})

D is the diameter of the reactor (cm)

μ is the dynamic viscosity of the fluid (g cm^{-1} s^{-1})

Under the experimental conditions of this study, where the flow rate of He was between $700 < Ve < 3000$ cm^3 min^{-1} , D = 2.4 cm , $\rho = 2.16 \times 10^{-7}$ g cm^{-3} at 373 K and $\mu = 2 \times 10^{-4}$ g cm^{-1} s^{-1}, the calculated Reynolds number (Re) is in the range of 1.8 – 7.8 for $700 < Ve < 3000$ cm s^{-1} and hence the flow is laminar and viscous.

2.2.3 Time of flight mass spectrometer

The schematic representation of the time of flight mass spectrometer is as shown in Figure 2. 12. The interface between the flow tube reactor and the mass spectrometer consist of a differentially pumped orifice-skimmer combination. The gas mixture exiting from the flow reactor (pressure = 1 – 3 Torr) was pumped through the cone with an orifice (skimmer) into the first chamber maintained at a lower pressure (1 x 10^{-3} Torr) using an Alcatel T550 turbo pump (450 dm^3 s^{-1} for He). The centre line portion of the expanded jet passed through a 2.1 mm skimmer (Beam Dynamics) aperture into the ionization chamber, which was maintained at less than 10^{-5} Torr by a Turbo pump (Varian 550 $l.s^{-1}$ for He).

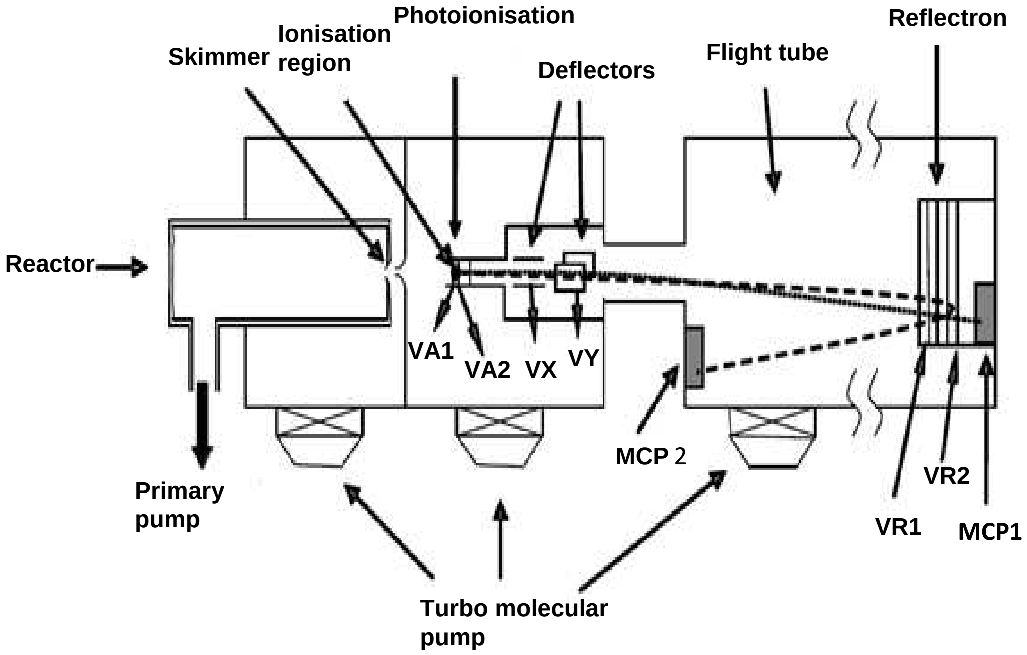

Figure 2. 12: The schematic representation of the Time of flight mass spectrometer

2.2.4 Ionization and detection

The ionisation method used in this study is called single photon ionisation. When a vacuum UV photon (118 nm) interacts with the compounds whose ionisation potential is lower than the energy of the incident photon, the molecule gets ionised producing molecular ion by loosing an electron. The vacuum UV photons are generated by pumping a dye (LDS- 720) with a Nd-YAG laser

(Quantel YG 581c) which produces a laser beam of 710 nm. This laser beam is frequency doubled using a beta barium borate (BBO) crystal. The 118 nm UV photons are then generated by tripling the frequency doubled UV laser beam in a rare gas (35 Torr of Xe).

The ionization region is equipped with two plates VA1 and VA2 (see Figure 2. 12*)* between which the particles are ionized and then accelerated through the potential difference of the two plates. The deflector plates VX and VY are used to create electric fields perpendicular to the path of ions and thus to guide the particles into the flight tube. The flight tube is 82 cm long held at 1×10^{-7} Torr pressure with a final turbo molecular pump (Varian, pumping speed of 150 L s-1 for helium). The ionised particles which travel through the flight tube at different speeds depending on their mass are detected using a combination of two microchannel plates (MCP1 and MCP2 : C-726; 40 mm active area) and a 820 mm reflectron. The reflectron helps in diverting the direction of ionized particles to the MCP2 which is kept opposite to MCP1.This prevents the saturation of the MCP as the total number of molecular ions detected are distributed over two MCPs.

2.2.5 Data acquisition

When a molecular ion hits the microchannel plate, it produces electrons and this electrical signal, is amplified, displayed on a numerical oscilloscope (TDS 3000 from Tektronix) and recorded on a PC. The recorded peaks which correspond to the changes in the recorded electrical signal can be related to the mass to charge (m/z) ratio of a specific molecular ion by using the relationship between the time of flight (T_{vol}) and the m/z as follows:

$$\boldsymbol{T_{vol} = \frac{L}{\sqrt{2eV}} \times \sqrt{\frac{m}{z}}} \qquad \textbf{\textit{E 4}}$$

Where,

T_{vol}= the time of flight (s)

L = the flight distance in the flight tube (L = 2.2 m)

e = the elementary charge, $e = 1.6 \times 10^{-19}$ C

V = the voltage in the acceleration zone of the mass spectrometer (V)

m = the mass of the molecular ion

z = charge of the ion

The mass resolution is $(m / \Delta m) = 1300$.

Accordingly, experiments were performed to investigate the reaction of OH + HMB and to identify the different products of this reaction. In this study, the OH and OD radicals were produced by the $F + H_2O\ (D_2O) \rightarrow OH\ (OD) + HF$ reaction. F atoms were produced in a microwave discharge at 2450 MHz (Sairem GMP 03 KSM) in a mixture of 1% F_2 in He (Linde) introduced into the 24 mm main reactor 50 cm before the reaction zone. Typical OH concentration ranges from $1 - 4 \times 10^{12}$ molecules cm^{-3}. HMB concentration that were used in these experiments were in the range $2 - 8 \times 10^{13}$ molecules cm^{-3}, with a ratio [HMB]/[OH] always greater than 10. HMB vapours were generated by passing helium (Linde, purity>99.996%) through a heated cell containing solid HMB. The HMB concentration in the reactor was determined relative to a known propene (C_3H_6) concentration by ionization using ($\sigma(C_3H_6$,10.54 eV) = $(11.0 \pm 1.0) \times 10^{-18}$ cm^2, and (σ(HMB,10.54 eV) = (σ(benzene, toluene, o,m,p-xylene,10.54 eV)= $(30.0 \pm 5.0) \times 10^{-18}$ cm^2). (For more details on the TOF-experiments, refer J.C. et al 2012 at the end of this thesis in Appendix A.

2.3 Laser photolysis coupled to time resolved UV spectrometer

The Laser photolysis coupled to UV spectrometer setup is as shown in Figure 2. 13

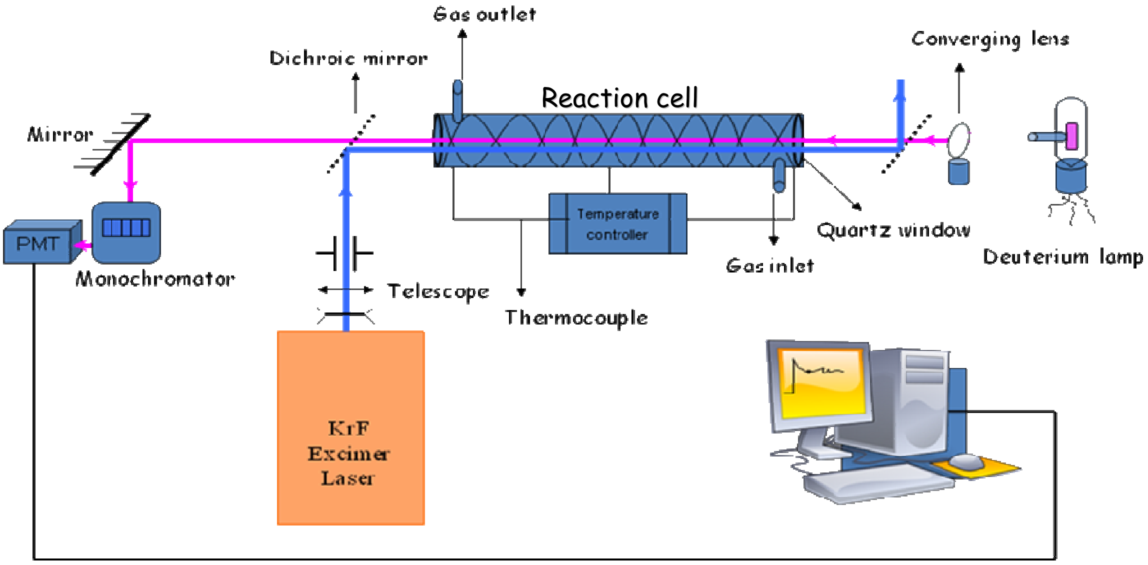

Figure 2. 13: Schematic representation of the Laser photolysis coupled to UV spectrometer setup

2.3.1 Reaction cell

The reaction cell is a 70 cm long cylindrical Pyrex tube, 1.8 cm internal diameter, and fitted with Suprasil grade quartz windows. Teflon O-rings are placed at regular intervals inside this tube in order to prevent the spread of excimer beam due to internal reflections. This cell was covered with heating coils and finally wrapped with aluminium paper. The temperature was measured at three different position of the cell and controlled accordingly using a temperature controller.

2.3.2 Excimer laser

The excimer laser (Lamda physic EMG 200) is similar to the one explained in section 2.1.2, except that the maximum laser energy of only 10-15 mJcm^{-2} could be obtained by applying a high voltage of 32 kV. A lens system made up of a converging and diverging lens which acts like a telescope was used to increase the size of the laser beam. This enlarged laser beam passes through the reaction cell using dichroic mirrors, one placed at the entrance of the reaction cell and the other at the exit. One disadvantage with this system is that the dichroic mirrors cut off the detection radiation from 235 to 260 nm.

2.3.3 Detection System

A deuterium lamp (Hamamatsu L2D2) placed perpendicular to the reaction cell acts as the source of detection radiation from 200 - 400 nm. Since the deuterium lamp emission is quite dispersed, an optical lens was used to focus the beam into the reaction cell. Once the beam passes through the reaction cell (single pass), it was then focused onto the entrance slit of a monochromator (Jobin Yvon HRP) with a resolution of 1 nm and was coupled to a photomultiplier tube (PMT). In this way, the intensity of the analysing beam could be monitored at a selected wavelength.

2.3.4 Data acquisition

The amplified electrical signal from the PMT needs to be digitized in order to be processed and stored. This is done using a data acquisition card (National Instruments) connected to a computer. A program written using Labview, controls the frequency of the excimer laser shot and the time of data acquisition. This allows to record the time resolved UV absorption signals.

2.3.5 Determination of initial OH concentration

Since it was intended to study the OH initiated oxidation of Hexamethyl benzene (HMB), it was important to determine the exact initial concentration of the OH radicals produced in the reaction cell. OH radicals were produced in the reaction cell using 248 nm photolysis of H_2O_2.

$$H_2O_2 \quad + h\upsilon_{248\ \mathrm{nm}} \quad \rightarrow \quad 2OH \qquad \textbf{(R 1)}$$

N_2 was bubbled through a bubbler containing aq. H_2O_2 solution (50% in H_2O) and the controlled flow was then introduced into a known fast flow of N_2, or N_2 and O_2. The resultant steady-state concentration of H_2O_2 in the cell was determined by its

UV absorption at 220 nm (σ = 2.58 x10^{-19} cm^2 molecule^{-1}) [8]. In order to determine the exact concentration of OH radicals produced on photolysis, a standard calibration procedure was used which involved the reaction of C_2H_6 (3 × 10^{16} molecules cm^{-3}) and OH radicals in presence of large excess of O_2 to form the $C_2H_5O_2$ radicals at (760±10) Torr. The primary step includes the H atom abstraction from C_2H_6 by OH radicals which leads to the production of C_2H_5 radicals. Under the pseudo first order conditions with respect to oxygen, C_2H_5 radicals are almost quantitatively converted into $C_2H_5O_2$ radicals.

Since the excimer laser shot produces a “dead time” during which the photomultiplier tube (PMT) goes blind for a period of 40 - 60 micro sec, the fast reactions of the formation of C_2H_5 radicals and their subsequent conversion to $C_2H_5O_2$ radicals occur within the excimer laser generated “dead time” and hence these kinetics forming $C_2H_5O_2$ radicals cannot be observed under the experimental conditions of this work. Instead, the change in the ratio of the intensity of incident radiation (I_o) to the intensity of the transmitted radiation (I_t), due to the absorption by the $C_2H_5O_2$ radicals is monitored at 270 nm where the absorption cross section(2.2 x 10^{-18} cm^2 molecule^{-1}) of $C_2H_5O_2$ radicals is well known [9]. Since the reaction kinetics of ethyl peroxy radicals are well known from the literature [10], by recording the time resolved UV decay profiles of $C_2H_5O_2$ and by modelling its decay kinetics, the initial concentration of OH radicals could be obtained.

2.3.6 Data Analysis

The change in the concentration of $C_2H_5O_2$ radicals with time leads to a change in the measured absorbance according to the Beer-lamberts law:

$$\boldsymbol{ln\frac{I_0}{I_t} = \sum_i \sigma_i \times C_i(t) \times l} \qquad \textbf{E 5}$$

Where

I_o = the intensity of the incident beam

I_t = the intensity of the transmitted beam

σ_i = cross section of the absorbing species i

C_i (t) = Concentration of the absorbing species i at time t l = optical path length (70 cm)

The mechanism used to simulate the $C_2H_5O_2$ decay profiles is as shown in Table 2. 1 and the simulated kinetic profile of the $C_2H_5O_2$ radical is as shown in Figure 2. 14.

Reaction	**Reaction number**	**Rate constant @ 373K $cm^3 molec^{-1} s^{-1}$**	**Reference**
$H_2O_2 + hv \rightarrow 2\ OH$	***R1***		
$C_2H_6 + OH \rightarrow C_2H_5 + H_2O$	R2	5.3×10^{-13}	[11]
$C_2H_5 + O_2 + M^* \rightarrow C_2H_5O_2 + M$	R3	7.6×10^{-12}	[12]
$C_2H_5O_2 + C_2H_5O_2 \rightarrow 2\ C_2H_5O + O_2$	R4a	6.18×10^{-14}	[10]
$\rightarrow C_2H_5OH + CH_3CHO$	R4b	2.52×10^{-14}	[10]
$C_2H_5O + O_2 \rightarrow CH_3CHO + HO_2$	R5	1.62×10^{-14}	[13]
$C_2H_5O_2 + HO_2 \rightarrow C_2H_5OOH + O_2$	R6	4.2×10^{-12}	[14]
$HO_2 + HO_2 \rightarrow H_2O_2 + O_2$	R7	1.62×10^{-12}	[15]
$OH + H_2O_2 \rightarrow HO_2 + H_2O$	R8	1.71×10^{-12}	[15]

**Reaction pressure = 760 ± 10 Torr*

Table 2. 1: The mechanism used to simulate the $C_2H_5O_2$ decay profiles

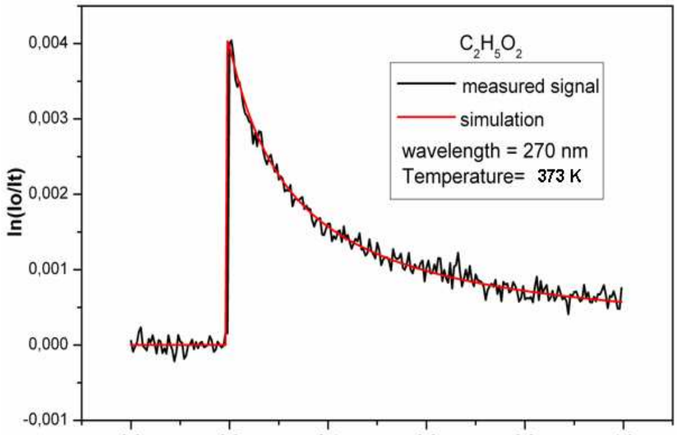

Figure 2. 14: Simulated UV decay profiles of $C_2H_5O_2$ radicals

Computer simulations were performed to simulate these decay profiles using a program written in Turbo Pascal language. Simulations involved creating a system of differential equations for the change in the concentration of the absorbing species considered in the mechanism. This system which depends on the rate constants and the cross sections of different absorbing species considered in the mechanism was then integrated numerically. Thus, by simulating the decay kinetics of ethyl peroxy radicals using the rate constants reported in the literature (see Figure 2. 15), the initial concentration of OH radicals was calculated with respect to the concentration of $C_2H_5O_2$ radicals. A typical example of the amount of OH radicals produced (obtained from the $C_2H_5O_2$ calibration) as a function of $[H_2O_2]$ at 15 mJ cm^{-2} is as shown in Figure 2. 15.

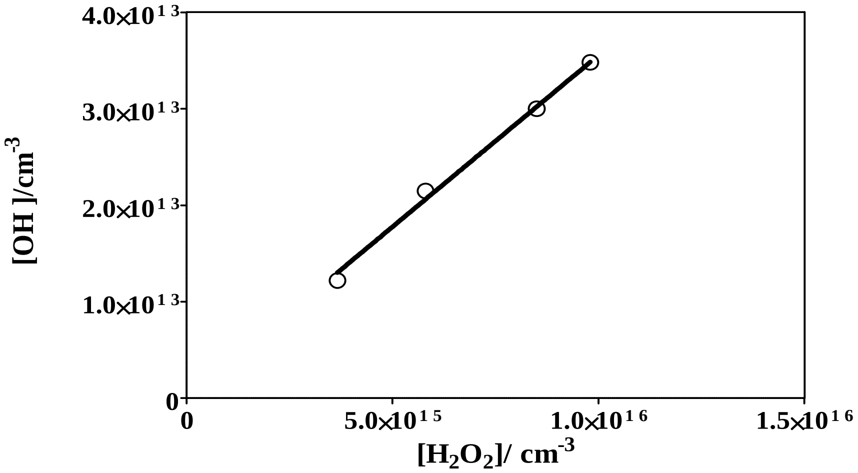

Figure 2. 15: Amount of OH radicals produced (obtained from the $C_2H_5O_2$ calibration) as a function of $[H_2O_2]$ at 15mJcm^{-2}

2.3.7 HMB-OH adduct spectrum

In order to record the UV absorption spectrum of the HMB–OH adduct, experiments were performed using the laser photolysis coupled to time resolved UV spectrometer. HMB-OH adduct was formed by the reaction of OH (from the laser photolysis of H_2O_2 at 248 nm) with the hexamethyl benzene and subsequently monitored using time-resolved UV spectrometer in the wavelength range 265 to 340 nm.

$$\text{HMB} + \text{OH} \longrightarrow \text{HMBOH adduct} \qquad \text{(R8)}$$

Gas mixtures consisted of passing N_2 through separate bubblers containing HMB and aqueous H_2O_2 solution and these controlled flows were introduced into a known fast flow of N_2, or N_2 and O_2. The resultant steady-state concentration of H_2O_2 in the cell was determined by its absorption at 220 nm ($\sigma = 2.58 \times 10^{-19}$ cm^2

molecule^{-1}) [8] and the concentration of HMB was determined by measuring and using its absorption cross-section (3.1 x 10^{-17} cm^2 molecule^{-1} [16]) at the same wavelength in two successive measurements. Since hexamethyl benzene is a solid, its vapour pressure is low (12 mTorr at 298 K [17]. Hence, it was necessary to have a robust heating system to generate enough hexamethyl benzene vapour pressure as well as to avoid the condensation of HMB in the reactor. To achieve the desired concentration of HMB in vapour phase, a cylindrical tube bubbler (70 cm long) with narrow openings at the two extreme ends was designed. A desired quantity of HMB was introduced in the bubbler which was then melted using a heat gun in order to have a thin uniform coating of HMB on to the inner walls of the cylindrical tube. The entire tube was covered with heating coils and then finally wrapped in aluminium paper. This tube containing HMB was heated at 373K to obtain the desired concentration. The concentration of HMB for a set value of N_2 flow was measured by its absorption at 220 nm. A stable concentration of (1 - 2) x 10^{15} molecules cm^{-3} was obtained. Typically, concentrations of ca. (6 - 8) x 10^{15} molecules cm^{-3} H_2O_2, and (1.5 - 2) x10^{15} molecules cm^{-3} HMB were employed in all experiments. HMB-OH adduct concentrations of (2 - 3) x 10^{13} molecules cm^{-3} were obtained, using laser fluence of 10 - 15 mJ cm^{-2}. H_2O_2 (Aldrich, 50wt %), HMB (Aldrich 99%), C_2H_6 (AGA, 99.95%), Nitrogen (Messer, 99.995%) and Oxygen (Messer, 99.995%) were all used without any further purification. Experiments were carried out with a fast total flow (around 2 Lmin^{-1}) and with an excimer pulse frequency of 0.125 s^{-1}. This allowed complete replenishment of the cell contents between successive laser shots. For each individual measurement, at a given wavelength, around 50 decay traces were recorded and averaged to improve the signal-to-noise ratio. Data analysis involved a similar procedure as described in section 2.3.6

In the next chapter we shall discuss the results obtained for the various experiments performed using the experimental techniques mentioned in the present chapter.

2.4 References

1. A. Parker, C. Jain, C. Schoemaecker, P. Szriftgiser, O. Votava, C. Fittschen: App. Phys. B Lasers and Opt. (2010).

2. O. Votava, M. Mašát, A.E. Parker, C. Jain, C. Fittschen, Review of Scientific Instruments. 83, 043110–043110–7 (2012).

3. S. Lipson, H.Tannhauser: http://en.wikipedia.org/wiki/File:Etalon-2.svg. http://en.wikipedia.org/wiki/File:Etalon-2.svg.

4. D. Halmer, G. Basum, P. Hering, M. Mu□rtz, Review of Scientific Instruments. 75, 2187 (2004).

5. C. Jain: Laser photolysis coupled to detection by LIF and cw- CRDS: Application to spectroscopic and kinetic studies of OH, HO_2 and HONO, Thesis submitted to Université Lille 1- Sciences et Technologies, (2011).

6. J-C Loison, S. Sanglar, E. Villenave: Rev. Sci. Instr. 76, 519–24 (2005).

7. C. Rio: Etude des mécanismes d’oxydation des composés terpéniques par le radical OH, submitted to University of Bordeaux1, (2009).

8. R. Atkinson, D.L. Baulch, R.A.Cox, J.N.Crowley, R.F. Hampson, R.G. Hynes, M.E Jenkin, M.J. Rossi, , J.Troe, J. Atmos. Chem. Phys. 4, 1461–1738 (2004).

9. G.S. Tyndall, R.A. Cox, C. Granier, R. Lesclaux, G.K. Moortgat, M.J. Pilling, A.R. Ravishankara, T.J. Wallington. J. Geophys. Res. D. 106, 12157–12182 (2001).

10. C. Anastasi, D.J. Waddington, A. Woolley, J. Chem. Soc., Faraday Trans. 1. 79, 505–516.

11. F.P. Tully, J.E.M. Goldsmith, A.T. Droege, J. Phys. Chem. 90, 5932–5937 (1986).

12. A.F. Wagner, I.R. Slagle, D. Sarzynski, D. Gutman, J. Phys. Chem. 94, 1853–1868 (1990).

13. D. Hartmann, J. Karthäuser, J. P. Sawerysyn, R. Zellner, Ber. Bunsenges: Phys. Chem. 94, 639 (1990).

14. R. Atkinson, D.L. Baulch, R.A.Cox, J.N.Crowley, R.F Hampson, J.A. Kerr, M.J. Rossi, J. Troe. Atmos. Chem. Phys. 6, 3625–4055 (2006).

15. C.C.Kircher, S.P Sander, J. Phys. Chem. 88, 2082–2091 (1984).

16. A. Bolovinos, J. Philis, E. Pantos, P. Tsekeris, G. Andritsopoulos. J. Mol. Spectrosc. 94, 55–68 (1982).

17. J.S. Chickos, P. Unhannannt, W. Hanshaw, J.Chem.Eng.Data. 8, 1133 (2006).

Chapter 3
The Chemistry of HO_2 + CH_2O reaction

3.1 The present understanding of the $CH_2O + HO_2$ chemistry

Formaldehyde (CH_2O) is an important intermediate in the tropospheric photo-oxidation of both methane and non-methane volatile organic compounds. It is also emitted to the troposphere both through natural and anthropogenic sources as a result of direct emission from vegetation or from the incomplete combustion of fossil fuels and biomass etc. In the troposphere, the most important removal pathway is photolysis by solar radiation and its oxidation by OH radicals, both processes are well known. In addition to this, the reaction of $CH_2O + HO_2$ has been a subject of research interest since many years because, especially under low NOx conditions and at low temperatures the title reaction might contribute to the loss of formaldehyde from the troposphere and thus result in changes in the HO_2 radical budget of the troposphere. However, this reaction can be more important in laboratory experiments due to generally higher concentrations compared to atmospheric conditions.

The reaction of CH_2O and HO_2 leads to an equilibrium generating the Hydroxymethyl peroxy radical ($HOCH_2O_2$) as shown in reaction R1.

$$HO_2 + CH_2O \leftrightarrow [HO_2CH_2O] \leftrightarrow HOCH_2O_2 \qquad R1$$

This equilibrium was first investigated by Su et al. [1] and Niki et al. [2] in 1979. They made use of flash photolysis technique coupled to the detection of the products by FTIR spectroscopy wherein the absorption due to an unknown species was assigned to $HOCH_2O_2$ radical. They also investigated the subsequent reaction of $HOCH_2O_2$ with HO_2 radicals generating the α-hydroxy-methyl-peroxide ($HOCH_2OOH$).

$$HO_2 + HOCH_2O_2 \rightarrow HOCH_2OOH + O_2 \qquad R\ 2a$$

Another reaction channel for the $HOCH_2O_2 + HO_2$ reaction leading to formic acid, was identified by Veyret et al.[3] in 1982 by flash photolysing a mixture of CH_2O, O_2 and NO while simultaneously monitoring the rate and the yield of NO_2 appearance. They performed kinetic simulations from which the rate constant for the association reaction $HO_2 + CH_2O$ was obtained. The formation of formic acid was explained based on the mechanism that involved 1) $HOCH_2O_2$ radical and its subsequent chemistry with NO and O_2 to produce formic acid.

$HOCH_2O_2 + NO \rightarrow HOCH_2O$ R3

$HOCH_2O + O_2 \rightarrow HCOOH + HO_2$ R4

and 2) the self reaction of $HOCH_2O_2$ to form $2HOCH_2O$ which than could undergo reaction R4 to form HCOOH. However, their simulations involved a very complicated reaction system and the rate constants were obtained by fitting the complex model. Hence these measurements were very indirect. In 1985 Barnes et al. [4] studied the title reaction in an indirect way by monitoring the reactants and nitrate products of the $HO_2 + CH_2O + NO_2$ reaction by using FTIR absorption spectrometry. They provided evidence for the formation of the $HOCH_2O_2$ radical as the primary reaction product by the IR spectroscopic identification of its NO_2 recombination product $HOCH_2OONO_2$. They have performed computer simulation of the concentration-time profiles of HO_2NO_2, H_2CO and $HOCH_2OONO_2$ from which they could obtain the rate constant $k_{CH2O+HO2} = (1.1\pm 0.4) \times 10^{-13}$ cm^3 $molecule^{-1}s^{-1}$ at 273 K. The equilibrium constants was later investigated by Zabel et al. [5] by crypto trapping HO_2 and $HOCH_2O_2$ at 96 K and measuring their concentration by ESR spectroscopy. The reported value of the equilibrium constant is $K = 3.4 \times 10^{-15}$ $molecule^{-1}$ cm^3 at 298 K. However, these studies were based on the measurement of product yields and no time resolved measurements were performed.

In 1989, Veyret et al. [6] re-investigated the $HO_2 + CH_2O$ equilibrium using the flash photolysis coupled to time resolved UV absorption spectroscopy. In this study the HO_2 radicals were generated by flash photolysing $Cl_2/CH_2O/O_2$ mixture. These measurements provided the first UV absorption spectrum of $HOCH_2O_2$ radicals in the wavelength range of 200 to 270 nm. Kinetic simulations of the HO_2 decay profiles were performed from which the rate constant $k_1= 6.3 \times 10^{-14}$ cm^3 $molecule^{-1}s^{-1}$, $k_{-1}= 125$ s^{-1} and $K_{eq}= 5 \times 10^{-16}$ $molecule^{-1}cm^3$ at 298 K were determined. However, it is important to note that in these measurements both HO_2 and $HOCH_2O_2$ radicals absorb in the same wavelength region, and therefore complications can be expected in determination of radical concentrations. High initial radical concentrations (up to 10^{14} molecules cm^{-3}) have been used in this study and the authors reported that the determination of the equilibrium constant was complicated largely by the fact that significant losses of both HO_2 and $HOCH_2O_2$ radicals occurred on the same time scale due to the competing reaction of $HOCH_2O_2$ with HO_2 radicals (R2) and hence the rate constants k_1 and k_{-1} determined in their study largely depends on the rate constant for reaction R2. In addition to these complications, the signal-to-noise ratio was rather low especially in the higher temperatures range (from 295 to 333 K). Hence, the rate constants k_1 and k_{-1} obtained from these measurements could well have been affected by the experimental limitations. It can be concluded, that all the above reported studies devoted to the measurement of the equilibrium constant, were performed with rather indirect and non selective techniques. Hence the rate constants k_1 and k_{-1} and also the equilibrium constant need to be reinvestigated in a more direct way.

Apart from the measurement of the equilibrium constant, the mechanism for the formation of formic acid is still very uncertain. In 1989, Burrows et al. [7] proposed that the reaction of $HO_2 + HOCH_2O_2$ directly leads to the formation of HCOOH even in absence of NO and have reported a product branching ratio of 60 ±15% for R2a and 40 ±15% for R2b respectively.

$$HOCH_2OO + HO_2 \rightarrow HCOOH + H_2O + O_2 \qquad R2b$$

However, recently the reaction of $HOCH_2O_2 + HO_2$ was investigated by Jenkin et al. [8] and they have identified an OH producing new radical channel assuming the oxy radical and O_2 as co- products:

$$HOCH_2OO + HO_2 \rightarrow OH + HOCH_2O + O_2 \qquad R2c$$

Also, it has been concluded from the same study that the oxy radical ($HOCH_2O$) reacts subsequently with O_2 to exclusively form HO_2 and HCOOH which explains the formic acid production observed in the earlier studies [1, 2, 7–9]

$$HOCH_2O + O_2 \rightarrow HCOOH + HO_2 \qquad R4$$

Jenkin et al. have reported a yield of 20±5% for the radical pathway R2c, along with 30±6% and 50±11% for R2b and R2a respectively.

In a more recent investigation (2010), Ngyuen et al. [10] performed theoretical calculations and provided evidence for the existence of another OH producing channel. The reaction of $HOCH_2O_2$ + HO_2 was found to proceed via a short lived unstable tetroxide which later decomposes via two different channels:

$$HOCH_2OO + HO_2 \rightarrow HOCH_2O_4H \rightarrow HCOOH + O_2 + H_2O \qquad \text{R2d}$$

$$\rightarrow HCOOH + HO_2 + OH \qquad \text{R2e}$$

Interestingly, they found that formic acid could be produced in two different channels while only one of them also produces OH radicals as shown in reaction R2d and R2e. The OH producing channel R2e was found to be two times slower than reaction R2d. Even though the overall mechanism of the reaction of HO_2 + $HOCH_2O_2$ proposed by Jenkin et al. was similar to the one of Nguyen et al., it is important to note that the reactions generating OH radicals such as proposed by Nguyen et al. are completely different from the OH radical pathway of Jenkin et al. If the chemistry of $HOCH_2O_2$ + HO_2 leads to the generation of OH radicals under atmospheric conditions, then the above reaction system could serve as an OH precursor especially in remote environments with high HO_2 and low NOx conditions.

From a broader perspective, even though the HO_2 + CH_2O chemistry is not the dominant loss process for CH_2O in the troposphere, yet it is not negligible and can play a more important role in laboratory or chamber studies due to the higher concentrations. Also, the recent finding about a possible OH production from the $HOCH_2O_2$ + HO_2 chemistry shows that a reinvestigation of the reaction system of HO_2 radicals with formaldehyde in a more direct way is needed. This provided the motivation for this work as we are able to measure selectively absolute concentrations of HO_2 radicals. We therefore investigated directly the HO_2 + CH_2O reaction system by measuring time resolved decay kinetics of HO_2 radicals using a highly sensitive, selective and absolute technique of cw-CRDS coupled to laser photolysis.

3.2 Results and Discussion

In order to investigate the kinetics of the reaction system of CH_2O with HO_2 radicals using laser photolysis coupled to CRDS technique, it is important to reliably know the absolute concentrations of CH_2O and HO_2 radicals. The use of cavity ring down spectroscopy to measure the absolute concentrations of HO_2 radicals in the near IR region has been validated in previous works [11]. Precisely knowing the concentration of formaldehyde is even more important, because we will work under pseudo-first order conditions with respect to formaldehyde, i.e. in large excess of formaldehyde compared to HO_2 radicals. Any error in the determination of formaldehyde concentration will therefore be directly transferred as a systematic error in the determination of the rate and equilibrium constant. It is known, that formaldehyde has structured absorption features in the wavelength region that is commonly used in this work for the detection of HO_2 radicals. We therefore intended to use our cw-CRDS set-up to quantify formaldehyde and therefore it is necessary to know the absorption cross sections of some absorption lines of formaldehyde in the near IR region, which can be used to determine its concentration. So far, only one study by Staak et. al [12] has been devoted to the determination of absorption cross section of formaldehyde in the near IR region around 6600 cm^{-1}. These measurements have been performed at a pressure of 1.6 Torr pure formaldehyde using cavity-enhanced absorption spectroscopy (CEAS). Since, it is expected that the pressure broadening of the bath gas (50 Torr He in our studies) could have a significant effect on the absorption cross sections of formaldehyde, it was intended to measure experimentally the absorption cross section of formaldehyde in the near IR region under our pressure conditions, so that it could be used to determine the absolute concentration of formaldehyde during the kinetic study of the reaction of HO_2 with CH_2O.

3.2.1 Measurement of the absorption cross section of formaldehyde in the near IR region

In order to measure the absorption cross section, the two important parameters that need to be determined are a) Concentration of the absorbing species and b) absorbance at a fixed absorbing path length. Using the above two parameters, the cross section of the absorbing species can be obtained from the Beer-lamberts law.

3.2.1.1 Determination of absolute concentration of formaldehyde

In order to determine absorption cross sections of formaldehyde, it is necessary to measure reliably the absolute concentration. Formaldehyde is a molecule difficult to handle: the monomer easily adsorbs on surfaces and also polymerizes. It is therefore not straight forward to prepare gas mixtures with a known concentration of formaldehyde. This difficulty has been bypassed in this work by applying a method that allows determining *in-situ* the concentration of formaldehyde through its reactivity against OH-radicals. The experimental system used in this study has already been discussed in section 2.1.6. The concentration time profiles of OH radicals were measured using laser photolysis coupled to LIF, first in absence of formaldehyde and then in presence of formaldehyde and from the two decay rates, using the well known rate constant of OH + CH_2O, the absolute concentration of formaldehyde is measured.

OH radicals were generated by photolysing H_2O_2 at 248 nm [11, 13] which react in the absence of other reaction partners in the following reaction sequence

$H_2O_2 + h\nu_{248} \rightarrow 2\,OH$ (R6)

$OH + H_2O_2 \rightarrow HO_2 + H_2O$ (R7)

$OH + HO_2 \rightarrow O_2 + H_2O$ (R8)

$2\,HO_2\ (+M) \rightarrow H_2O_2 + O_2\ (+M)$ (R9)

$2\,OH\ (+M) \rightarrow H_2O_2\ (+M)$ (R10)

$OH \rightarrow$ Diffusion (R11)

$HO_2 \rightarrow$ Diffusion (R12)

The absorption cross section of H_2O_2 at 248 nm is 9.4×10^{-20} cm^{-2}[14], which leads at a typical photolysis energy of 50 mJ cm^{-2} and initial H_2O_2 concentrations of $\approx 3 \times 10^{14}$ molecules cm^{-3} to an initial OH radical concentration of $\approx 3 \times 10^{12}$ molecules cm^{-3}. Under these conditions, the self reactions of OH radicals can be safely ignored, because it is too slow ($k_{10} = 6.9\times10^{-31}$ cm^6 $molecule^{-2}s^{-1}$) [15] to be competitive with reaction (R7), even at short reaction times. A simulation of the above model shows, that less than 0.3% of the initial OH radicals will decay through (R10) and this reaction has therefore no impact on the decay rate of OH radicals. Hence, OH radicals will predominantly react at short reaction times with H_2O_2 to form HO_2 radicals (R6). As the reaction advances and the HO_2 radical concentration increases, the very fast reaction (R8) ($k_8 = 1.1\times10^{-10}$ molecule^{-1}cm^{3}s^{-1}) [15] becomes more or less important, depending on initial H_2O_2 concentration and photolysis energy [16]. Under our conditions, around 10 – 15% of the OH radicals react, in the absence of formaldehyde, through reaction (R8). This leads at longer reaction times (when the HO_2 concentration becomes high and consequently the OH concentration becomes low) to an acceleration of the decay compared to a mono exponential decay. This effect however is so small, that it is not visible at our typical signal-to-noise ratios (see Figure 3. 1). Finally at longer reaction times, the HO_2 radicals recombine through self-reaction (R9), but this process has no impact on the OH decay. Loss of OH and HO_2 radicals out of the photolysis volume due to diffusion is only a minor process under our conditions and from our experience we know that it can be approximated by an exponential decay. The H_2O_2 concentration can thus be obtained by measuring OH-decays using LIF (see upper curve inFigure 3. 1) and subsequent fitting of the decays to the above mechanism. Using a rate constant of $k_7 = 1.7\times10^{-12}$ cm^3 molecule^{-1}s^{-1} for (R7) [15], we deduce typical concentrations of $[H_2O_2] \approx 3 \times 10^{14}$ molecules cm^{-3}.

Formaldehyde in the vapour phase was generated by gently heating and thus depolymerising *para*-formaldehyde (solid) in a trap through which 100 sccm He gas was flown; this He flow carried the depolymerised gas phase formaldehyde through a short Teflon tube into the reactor. This He/CH_2O mixture was further diluted at the exit of the trap by a much higher He dilution flow (around 400 ccm STP) in order to avoid the re-polymerization of formaldehyde to *para*-formaldehyde and its subsequent condensation within the Teflon tubing or within the reactor, maintained at 295 K. The concentration of formaldehyde was varied by varying the temperature of the *para*-formaldehyde trap in the range of 303 K – 313 K. For the purpose of determining the absolute formaldehyde concentration it is sufficient in a first approximation to deduce the first order decay including all loss processes for OH radicals in the absence of formaldehyde (named k'_{H2O2}).

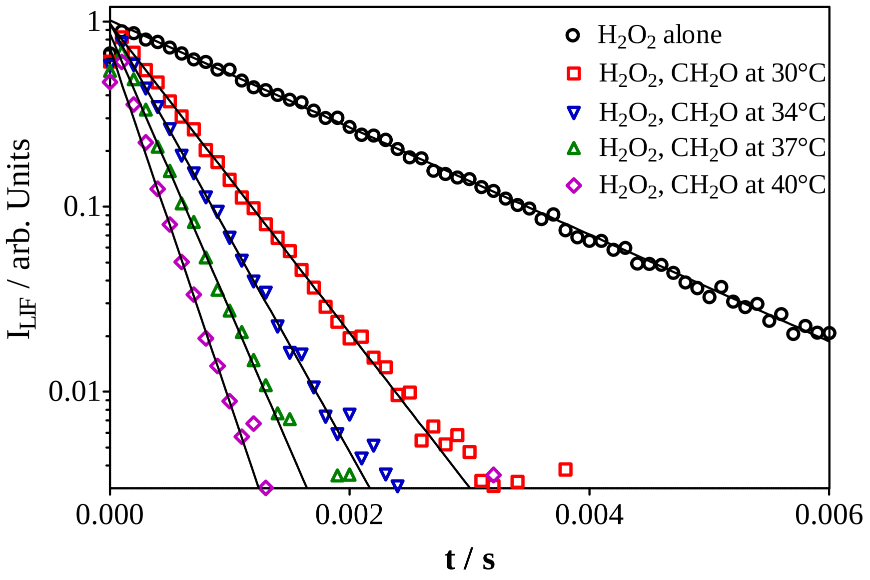

Figure 3. 1: OH decays in presence different concentrations of formaldehyde

Addition of formaldehyde to the reaction mixture will lead to a competition for OH radicals between the above discussed loss processes, mainly (R2), and its reaction with formaldehyde:

$$OH + CH_2O \rightarrow H_2O + CHO \qquad (R13)$$

Therefore the OH-decay in the presence of H_2O_2 and CH_2O can be expressed by

$$\frac{d[OH]}{dt} = -[OH] \times (k'_{H2O2} + k_{13} \times [CH_2O]) \quad \textbf{(E1)}$$

and hence

$$ln\frac{[OH]_0}{[OH]} = (k'_{H2O2} + k_{13} \times [CH_2O] \times t) = k'' \times t \quad \textbf{(E2)}$$

Knowing the first term k'_{H2O2} by measuring the OH-decays in the absence of formaldehyde, the absolute concentration of formaldehyde can now be determined from the exponential OH-decays obtained in the presence of H_2O_2 and CH_2O (k''):

$$[CH_2O] = (k'' - k'_{H2O2})/k_{13} \qquad \textbf{(E3)}$$

Reaction (R13) is an important process in atmospheric chemistry, therefore its rate constant has been measured several times and all results have been reviewed by Atkinson et al. [15] leading to a recommended rate constant of $k_{13} = 8.5\times10^{-12}$ cm^3 $molecule^{-1}$ s^{-1} with an uncertainty of ± 15 %.

This simple approach leads to a slight underestimation of the formaldehyde concentration due to the fact, that in the presence of formaldehyde the loss of OH radicals through (R8) becomes negligible: not only the concentration of HO_2 radicals decreases drastically compared to experiments in the absence of formaldehyde, but also the OH decay itself is much faster and thus less time is available for the radical-radical reaction (R7). Simulations show, that the formaldehyde concentration would be underestimated by around 3% due to this process. However, this approximation is counter balanced by another approximation: HCO radicals, the product of reaction (R13), react very rapidly with OH radicals ($k = 1.7\times10^{-10}$ cm^3 $molecule^{-1}s^{-1}$) [17], which has a similar effect than (R8) in the absence of formaldehyde. Therefore, the simple approximation of (E3) leads within less than 2% to the same formaldehyde concentration than fitting the OH decays to a full model including all radical-radical reactions.

Another possible error source is the photolysis of formaldehyde at 248 nm, which leads with high quantum yields to H-atoms and HCO radicals [18]. These radicals react with OH radicals and can therefore have an impact on the OH decays. However, the absorption cross section of formaldehyde at 248 nm is only 2.5×10^{-21} cm^{-2} [18], i.e. around 40 times smaller than the absorption cross section of H_2O_2. Because the initial concentrations of formaldehyde and H_2O_2 are roughly the same, the radical concentration produced by this process is also 40 times smaller than the initial OH radical concentration. It has been shown that radical-radical reactions induced by the H_2O_2 photolysis are negligible (except for (R8) in the absence of formaldehyde), it can therefore be safely considered that an increase in the initial radical concentration by a few percent will not change this conclusion. Also, the low absorption cross section of formaldehyde at 248 nm assures that the formaldehyde concentration can be considered identical during the photolysis experiments and the cw-CRDS measurements: under our conditions, only a fraction of less than 10^{-4} of the initial formaldehyde is photolysed. It can be seen in Figure 1, that the OH-decays are nicely exponential over more than 2 orders of magnitude, with a statistical error of less than 5%. We therefore estimate that this method leads to the determination of the formaldehyde concentration with an accuracy of better than 20%.

3.2.1.2 Measurement of the formaldehyde absorption spectra

cw-CRDS can be synchronized to laser photolysis in order to obtain time resolved profiles of species like HO_2 [19] or HONO [20], but was used in this work independent of the laser photolysis for the measurement of the formaldehyde absorption spectrum. Once the OH decay has been obtained with a good signal-to-noise ratio (the LIF signals have been averaged over 50 to 100 photolysis pulses), the photolysis laser was stopped, the gas mixture was allowed to renew and the absorption spectrum of formaldehyde was measured with a resolution of around 0.001 cm^{-1} (red line in Figure 3. 2). The absorption spectra of two different absorption lines at 6625.248 and 6624.779 cm^{-1} were measured each at two different total pressures, 11 and 50 Torr He. Typically, 50 ring-down events have been averaged before the cw-CRDS diode laser was tuned to the next wavenumber. For more details on absorption spectrum measurement using cw-CRDS, refer Chapter 2, section 2.1.7. Once the absorption spectrum has been measured, the photolysis laser is turned on and the OH decays were re-measured again in order to verify that the formaldehyde concentration had not changed during the measurement of the spectrum. Following this step, the formaldehyde flow into the reactor has been stopped by rerouting the small He-flow outside the formaldehyde trap. This enabled the measurement of the spectroscopic base line (black line inFigure 3. 2) and also the kinetic baseline, i.e. the decay of OH radicals in the absence of formaldehyde. An example for a measured spectrum of formaldehyde is shown in Figure 3. 2

.

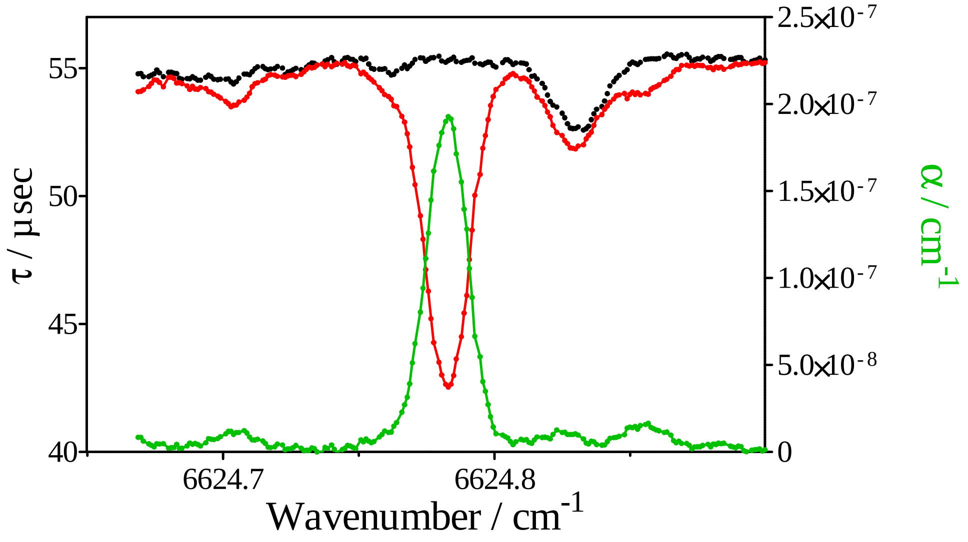

Figure 3. 2: Typical example of absorption spectrum for firmaldehyde at 11 Torr He: upper black line: ring down time as a function of wavenumber measured in the absence of formaldehyde (left axis), middle red line: ring down time as a function of wavenumber measured in the presence of formaldehyde (left axis), lower green line is the absorbance calculated for the given conditions using equation [1]. (λmax= 6624.779 cm^{-1})

The CRDS equation has been used to calculate the absorption coefficent (α) at a given wavelength, which is equal to the product of [CH_2O] and its absorption cross section (σ), as shown in Equation E4.

$$\alpha_\lambda = [CH_2O] \times \sigma_\lambda = \frac{R_L}{c}\left(\frac{1}{\tau} - \frac{1}{\tau_0}\right) \qquad \textbf{(E4)}$$

where c the speed of light, τ_0 and τ are the ring-down times in the absence and presence of formaldehyde, respectively and R_L being the ratio between the cavity length L, i.e. the distance between the two cavity mirrors (80 cm), to the length L_A over which the absorber is present. L_A is in our case 74 cm, because 3 cm are deduced at each side in order to take into account the flushing of the mirror holders, necessary to protect the CRDS mirrors. Figure 3. 2 shows typical example of such a measurement: the upper black line represents the spectrum obtained at 11 Torr in the absence of formaldehyde, i.e. only H_2O_2 and H_2O are present and small absorption features due to their presence can be observed. The middle red line represents the evolution of the ring down time as a function of wavenumber after addition of 3.6 × 10^{14} molecules cm^{-3} formaldehyde to the gas mixture (left y-axis applies for both traces). The lower green line represents the absorption spectrum obtained by applying equation E4 to each data point (right Y-axis applies). The absorption cross section at the center of the line can be directly taken from this type of graph, but it is more precise to deduce it from fitting the full line profile. In Figure 3. 3 such a fitting is shown for the absorption line at 6625.248 cm^{-1} at 50 Torr using a formaldehyde concentration of 4.39×10^{14} cm^{-3}: The Fityk software (Version 0.9.8) [21] has been used for a least-square fit of the experimental data of this small portion of the spectrum to a Voigt profile. The Doppler half-width at half-maximum (HWHM) γ_D has been fixed to its theoretical value at ambient temperature (0.00744 cm^{-1}).

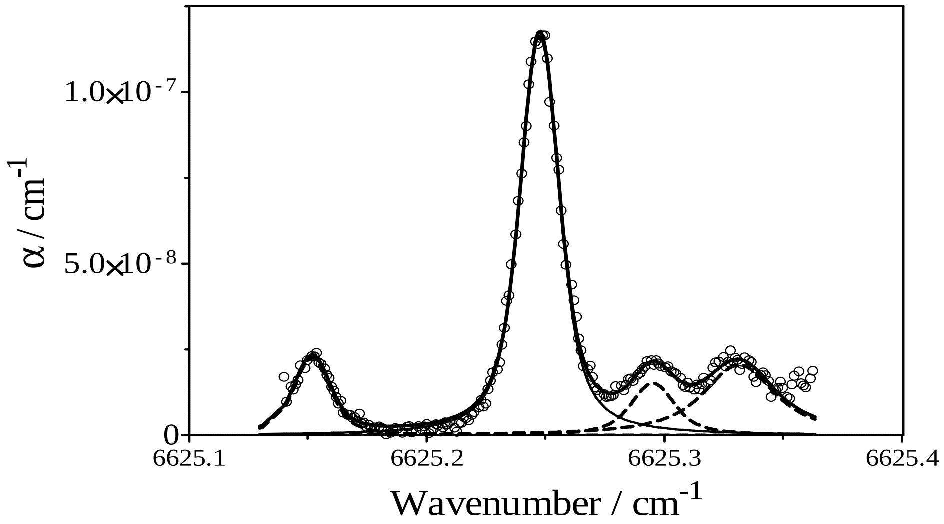

Figure 3. 3 : Absorption spectrum of formaldehyde around 6625.248 cm^{-1}. Open dots are experimental values, lines represent fits to Voigt profile by fixing the Doppler width to its theoretical value: dashed lines represent the fits for individual lines, full line represents the sum

The obtained absorption coefficient values at the maximum of the absorption peak were plotted as a function of formaldehyde concentration as shown inFigure 3. 4: the upper graph shows the results from experiments at 11 Torr, the lower graph at 50 Torr. The error bars have been estimated from the signal-to-noise ratio of the cw-CRDS measurements and were more important during the 50 Torr measurements. The slope of the linear regression leads directly to the absorption cross section at the center of the absorption line at the given pressure.

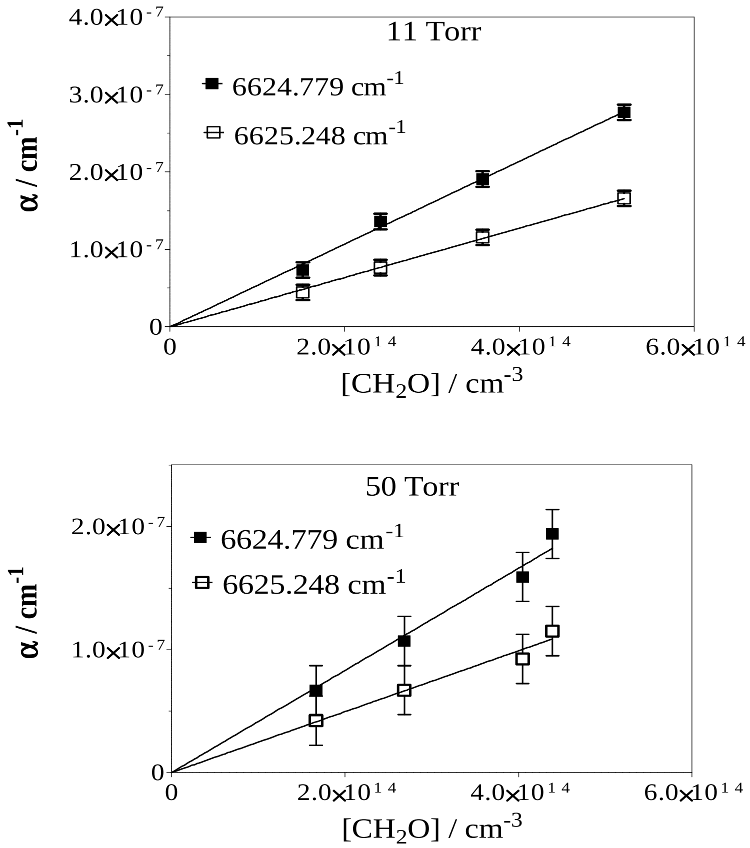

Figure 3. 4: Plot of absorption coefficient (α) as a function of formaldehyde concentration for the two absorption lines at 6624.779 and 6625.248 cm^{-1} measured at 11 and 50 Torr.

The obtained cross section values for the two absorption lines at 11 and 50 Torr are presented in Table 3. 1

	$\sigma_{11\ Torr}$ / 10^{-22} cm^2	$\sigma_{50\ Torr}$ / 10^{-22} cm^2	γ_{coll} / cm^{-1} atm^{-1}	A / 10^{-24} cm
6624.779 cm^{-1}	5.34 ± 0.08	4.2 ± 0.1	0.044 ± 0.008	9.13
6625.248 cm^{-1}	3.18 ± 0.04	2.47 ± 0.09	0.037 ± 0.003	5.27

Table 3. 1: Pressure dependant absorption cross sections (σ) at the centre of the two absorption lines at 11 and 50 Torr, collision induced broadening factor (γ) and line strength (A). The errors represent statistical error only and refer thus to the quality of the linear fit.

3.2.2 Pressure broadening of the formaldehyde absorption lines

Figure 3. 5 shows the absorption line at 6625.248 cm^{-1} at 11 and 50 Torr Helium, normalized to the concentration of formaldehyde, with the full lines showing the least-square fit to a Voigt profile.

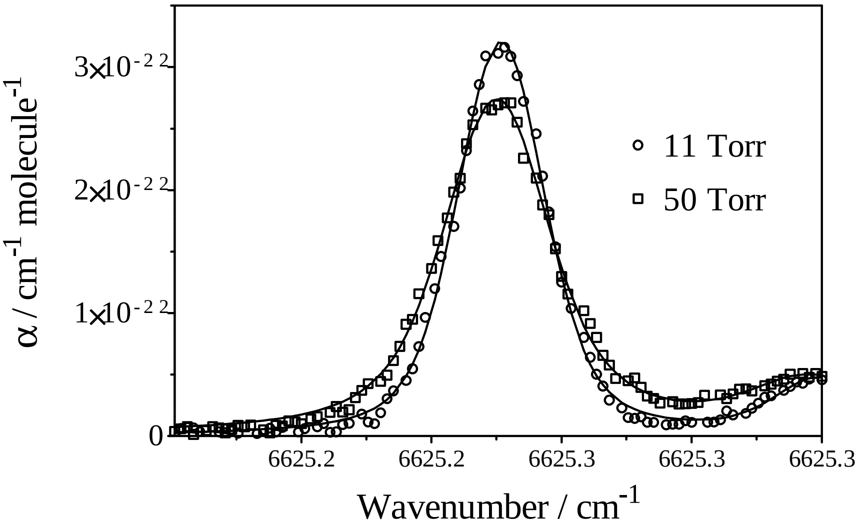

Figure 3. 5: Pressure dependant absorption lines at 11 and 50 Torr He, divided by the formaldehyde concentration. Full lines represent the model to a Voigt profile

Figure 3. 6 shows the half width at half maximum, obtained as average from fitting the experimental data at all four formaldehyde concentrations, as a function of the pressure for both absorption lines.

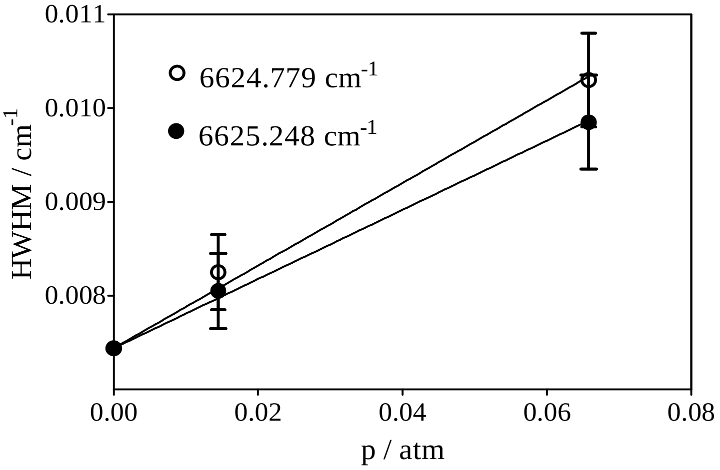

Figure 3. 6: Measured half-widths at half-maximum (HWHM) as a function of pressure for both lines. Line width at zero pressure represents the theoretical value at ambient temperature (0.00744 cm^{-1}), regression lines have been forced through this value.

The intercept of the linear regression, leading to the collision induced broadening factor, has been forced through the theoretical value of the Doppler width at room temperature. The obtained broadening factors are listed in Table 3. 1 for both lines. Even though broadening factors depend on the quantum state of the transition [22], the broadening coefficients obtained for both lines can be considered the same within the error limits. Also shown in Table 3. 1 are the line strengths for both absorption lines as obtained from the area in the Voigt fits. With this information it is possible to estimate the absorption cross section under the conditions in the work of Staak et al.[23] in order to compare both results. Using our line strengths and the self-broadening coefficient measured by Staak et al. (0.918 cm^{-1} atm^{-1}), one obtains the following absorption cross sections for the experimental condition of Staak et al., 1.5 Torr formaldehyde: $\sigma_{6624.779cm-1} = 4.64 \times 10^{-22}$ cm^2 and $\sigma_{6625.248cm-1} = 2.68 \times 10^{-22}$ cm^2. These values can be compared with the absorption cross sections listed by Staak et al.[23] for these two lines: 9.3 and 5.3×10^{-22} cm^2. Both values obtained in this work are 50 % lower than the values listed by Staak et al.

The absorption of formaldehyde in the near IR region has already been used in two experimental systems: Djehiche et al.[24] have observed the formation of formaldehyde during the photolysis of methylnitrite, CH_3ONO, using a small absorption line at 6625.74 cm^{-1}. For this line, Staak et al. reported an absorption cross section of 1.15×10^{-22} cm^2, while Djehiche et al. have determined the absorption cross section in 40 Torr of air by using a commercial calibrated standard mixture of formaldehyde. From these measurements they have determined an absorption cross section of 2.7×10^{-23} cm^2. In order to compare both values, one can use the broadening coefficients for N_2 and for self-broadening from Staak et al.: the absorption cross section of Djehiche et al. converts into a line strength of 1.12×10^{-24} cm, which in turn transforms into an absorption cross section of 5.7×10^{-23} cm^2 under 1.5 Torr of formaldehyde. In excellent agreement with this work, the value of Djehiche et al. is only 47% of the value listed by Staak et al. In a more recent work, the near IR absorption has been used to quantify formaldehyde as a reaction product during the oxidation of methane, CH_4, in a jet-stirred reactor [25]. In this work, four absorption lines between 6638 and 6642 cm^{-1} have been employed by using the absorption cross sections such as reported by Staak et al. to quantify formaldehyde. A good agreement between the formaldehyde concentrations calculated by using the four different absorption lines has been found, indicating that the relative peak heights are in good agreement with the relative peak heights such as obtained by Staak et al. However, the absolute concentrations are in poor agreement with model predictions: the measured concentrations are a factor of 2 lower than the predictions. Expanding the results from this work over the entire wavelength range, i.e. dividing all absorption cross sections of Staak et al. by a factor of 2, would bring into excellent agreement the experimental results obtained by Bahrini et al. [25] with the model predictions.

The explanation for the disagreement of a factor of 2 between the three different, independent measurements of absorption cross sections in different regions of the spectrum and the work of Staak et al. is yet unknown. However, a possible cause of the error needs to be discussed: First of all, Staak et al. have measured the spectrum in a static cell, filling it with 1.5 Torr of pure formaldehyde: a systematic error in the pressure measurement might not be ruled out completely. Also, formaldehyde is difficult to handle, some formaldehyde might have been adsorbed on the windows of the cell, thus adding to the light absorption, but not to the pressure measurement: such an effect would lead to higher absorption cross sections. The method presented in this work avoids such possible, systematic errors due to the in-situ measurement of the formaldehyde concentration. Another reason might be that CEAS is not an absolute method as is CRDS, the reflectivity of the mirrors must be obtained through independent processes. All systematic errors during this procedure are directly transferred to the absorption cross sections of formaldehyde. Therefore, it can not be ruled out that the sum of all possible errors in the work of Staak et al. might lead to absorption cross section systematically too high by a factor of 2. The measured cross sections of formaldehyde were then used to determine the concentration of formaldehyde that were employed in the measurements of the equilibrium constant of $CH_2O + HO_2$ reaction.

3.2.3 Determination of Equilibrium constant of CH_2O +HO_2 reaction

In order to determine the equilibrium constant for the reaction of CH_2O + HO_2, experiments were performed by using laser photolysis coupled to cavity ring down spectroscopy. The reaction has been initiated through the photolysis of formaldehyde, leading to the formation of HCO and H atoms, both of which react subsequently with O_2 to generate HO_2 radicals. The photolysis channels [26] of formaldehyde are as shown below.

$$CH_2O + h\nu_{248nm} \rightarrow HCO + H \qquad \Phi = 0.28 \qquad (R14a)$$

$$\rightarrow CO + H_2 \qquad \Phi = 0.49 \qquad (R14b)$$

$$HCO + O_2 \rightarrow HO_2 + CO \qquad (R15)$$

$$H + O_2 \rightarrow HO_2 \qquad (R16)$$

Due to the low absorption cross section of formaldehyde at 248 nm ($\sigma = 2.53 \times 10^{-21}$ cm^2), only low concentration of HO_2 radicals can be generated this way. In order to improve the signal to noise ratio, H_2O_2 ($\sigma = 9.1 \times 10^{-20}$ cm^2) was co-photolysed along with formaldehyde at 248 nm. The photolysis of H_2O_2 leading to the generation of OH radicals with the subsequent chemistry leading to HO_2 formation has already been discussed in the previous section. Under the typical experimental conditions of this study, $[CH_2O] = 2.98 \times 10^{15}$ cm^{-3}, $[H_2O_2] = 1.4 \times 10^{14}$ cm^{-3}, $[OH] = (1 - 2.4) \times 10^{12}$ cm^{-3} and $[O_2] = 1.5 \times 10^{17}$cm^{-3}, the pseudo first order rate constant $k'_{CH2O+OH} = 25500$ s^{-1} [28] is much greater than $k'_{H2O2+OH} = 238$ s^{-1} and hence the major reaction in this co-photolysis system was the reaction of OH radicals with formaldehyde, leading to the H abstraction forming HCO and H_2O. Both H and HCO radicals are immediately converted into HO_2 radicals under the time scale of these measurements, $k_{HCO+O2} = 780000$ s^{-1} [29] and $k_{H+O2} = 1336$ s^{-1} [30]. A typical HO_2 concentration-time profile recorded at a photolysis laser energy of 33 mJcm^{-2} is shown in Figure 3. 7 on a semi-logarithmic scale. The decay profile of the HO_2 radicals can be expressed by a bi-exponential decay showing two different slopes, a fast decay for reaction time < 10 ms followed by a much slower decay for reaction times > 10 ms.

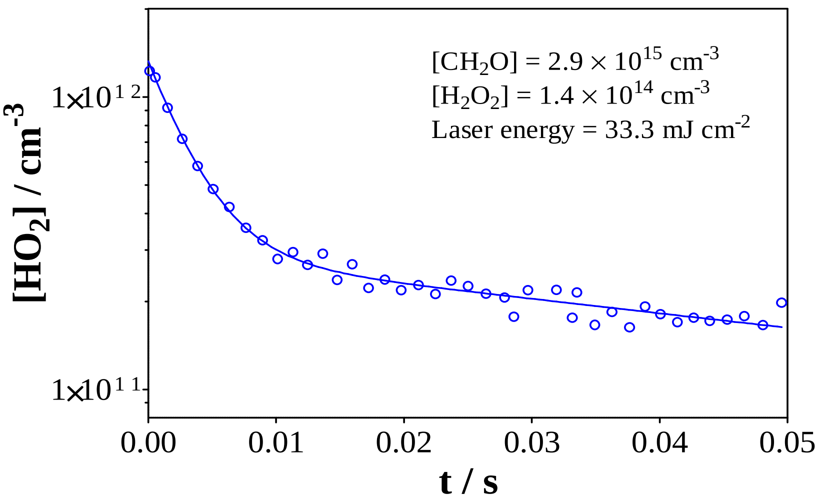

Figure 3. 7: A typical HO_2 concentration-time profiles at 297K and 51 Torr total pressure.

The bi-exponential fitting equation used to fit the HO_2 decay profiles is given as:

$$[HO_2]_{observed} = \{[HO_2]_0 \times \%fast \times exp\ (-k_{fast} \times t)\} + \{[HO_2]_0 \times (1-\%fast) \times exp\ (-k_{slow} \times t)\} + P \qquad (E5)$$

where $\%_{fast}$ is the fraction of the observed HO_2 signal due to the fast phase. k_{fast} and k_{slow} are the rate constants in s^{-1} corresponding to the fast and the slow phase running down to plateau (P) (P has been fixed to 0 in all fits). $[HO_2]_0$ is the initial concentration of HO_2 at time t=0.

Under the experimental conditions employed in this study, the reaction of HO_2 with formaldehyde was at short reaction times the major scavenger for HO_2 radicals with the first slope in Figure 3. 7 representing exclusively the reaction of HO_2 + CH_2O running into the equilibrium. In the absence of any other loss processes for the HO_2 radicals out of the equilibrium the second slope would have been zero and the HO_2 concentration at long reaction times would represent the equilibrium concentration of HO_2. However, this not the case as the HO_2 radical concentration gradually decays as represented by the second slope at longer reaction times. The observed second slope (between 7 and 20 s^{-1} in our experiments, depending on the reaction conditions) can not be explained by the self-reaction of HO_2 radicals, as this reaction is very slow (< 1 s^{-1}) under our typical HO_2 equilibrium concentrations (< 10^{12} cm^{-3}).

This slope is partly due to the loss of HO_2 radicals as well as the adduct ($HOCH_2O_2$) out of the detection volume by diffusion, and possibly due to the reaction of HO_2 radicals with the adduct as well as a possible self-reaction of the adduct, as already explained in section 3.1. Neglecting any impact of secondary reactions on the equilibrium concentration of HO_2 radicals, the equilibrium constant can be obtained in a first approximation from a fit of the HO_2 concentration-time profiles to a bi-exponential decay as explained below:

The equilibrium constant can be written in terms of the concentration of the products and the reactants as:

$$\boldsymbol{K_{equilibrium}} = \frac{[\boldsymbol{HOCH_2O_2}]}{[\boldsymbol{CH_2O}]\times[\boldsymbol{HO_2}]\boldsymbol{equilibrium}} \quad \textbf{\textit{(E6)}}$$

The equilibrium concentration of HO_2 can be obtained by extrapolating the second slope of the HO_2 decay profile to time t = 0. Hence, using the bi-exponential fitting equation, the concentration of HO_2 in equilibrium and the concentration of $HOCH_2O_2$ is obtained as follows:

$$[HO_2]_{equilibrium} = ([HO_2]_0 - P) \times (1 - \%fast) \quad \textbf{\textit{(E7)}}$$

$$[HOCH_2O_2] = ([HO_2]_0 - P) \times \%fas\boldsymbol{t} \quad \textbf{\textit{(E8)}}$$

Substituting equation E7 and E8 in equation E6, the equilibrium constant can be written as:

$$\boldsymbol{K_{equilibrium}} = \frac{([\boldsymbol{HO_2}]_{\boldsymbol{0}}-\boldsymbol{P})\times\%\boldsymbol{fast}}{([\boldsymbol{HO_2}]_{\boldsymbol{0}}-\boldsymbol{P})\times(\boldsymbol{1}-\%\boldsymbol{fast})\times[\boldsymbol{CH_2O}]} \quad \textbf{\textit{(E9)}}$$

Using equation E9, the equilibrium constant at 297 K, $K_{equilibrium}$ = (K_c) = 5.4 x 10^{-16} molecule^{-1} cm^3 was obtained for a bi-exponential fit to the HO_2 decay profile in Figure 3. 7

Since HO_2 reacts with CH_2O to enter an equilibrium, k_{fast} is defined as:

$$k_{fast} = k_1[CH_2O] + k_{-1} \quad \textbf{\textit{(E10)}}$$

Equation E10 can be modified in order to obtain k_1 as follows:

$$k_{fast} = k_1([CH_2O] + \frac{k_{-1}}{k_1})$$

$$k_{fast} = k_1 \times [CH_2O] \times (1 + \frac{1}{[CH_2O]\times K_{equilbrium}})$$

Substituting E6 in the above equation, we get

$$k_{fast} = k_1 \times [CH_2O] \times (1 + \frac{[HO_2]_{equilibrium}}{[HOCH_2O_2]}) \qquad \textbf{(E11)}$$

Rearranging equation E11, to obtain k_1,

$$\boldsymbol{k_1 = \frac{k_{fast}}{[CH_2O]\times[1+\frac{[HO_2]_{equilibrium}}{[HOCH_2O_2]}}} \qquad \textbf{(E12)}$$

k_{fast} is obtained directly from the bi-exponential fits while $[HO_2]_{\text{equilibrium}}$ and $[HOCH_2O_2]$ are calculated using equation E7 and E8 respectively. Hence, the rate of the $CH_2O + HO_2$ forward reaction (k_1) can be obtained from equation E12.

Since, $K_{\text{equilibrium}}$ can also be defined as,

$$K_{equilibrium} = \frac{k_1}{k_{-1}} \qquad \textbf{(E13)}$$

rearranging equation E13 and substituting equation E12 in E13, we can calculate k_{-1} as follows.

$$\boldsymbol{k_{-1} = \frac{\frac{k_{fast}}{[CH_2O]\times[1+\frac{[HO_2]_{equilibrium}}{[HOCH_2O_2]}}}{K_{equilibrium}}} \qquad \textbf{(E14)}$$

Using, equation E12 and E14, the rate constants $k_1 = 3.7 \times 10^{-14}$ cm^3 $molecule^{-1}$ s^{-1} and $k_{-1} = 69.5$ s^{-1} at 297 K were obtained from the bi-exponential fit for the example in Figure 3. 7. In order to validate the above results, a series of experiments were performed by changing different experimental conditions such as formaldehyde concentration, photolysis laser energy and the reaction temperature. The results obtained from each of the above variations are discussed in the next section.

3.2.3.1 HO_2 decay a function of formaldehyde concentration

In order to confirm that the loss of HO_2 radicals at short reaction times <10 ms was mainly due to its reaction with formaldehyde (in large excess) running into an equilibrium, experiments were performed by measuring HO_2 concentration time profiles as a function of formaldehyde concentration at a fixed laser energy and reaction temperature. formaldehyde concentrations have been varied during this study in the range $[CH_2O] = (3.0 - 7.2) \times 10^{15}$ molecules cm^{-3}, with $[H_2O_2] = 1.4 \times 10^{14}$ molecules cm^{-3} and $[O_2] = 1.5 \times 10^{17}$ molecules cm^{-3}, initial HO_2 concentrations were in the range $[HO_2]_0 = (0.7- 2.7) \times 10^{12}$ molecules cm^{-3}.

The HO_2 decay profiles at three different formaldehyde concentrations are shown on a semi- logarithmic scale in Figure 3. 8 : for easy comparison, the HO_2 signals have been normalized with respect to the initial HO_2 concentration.

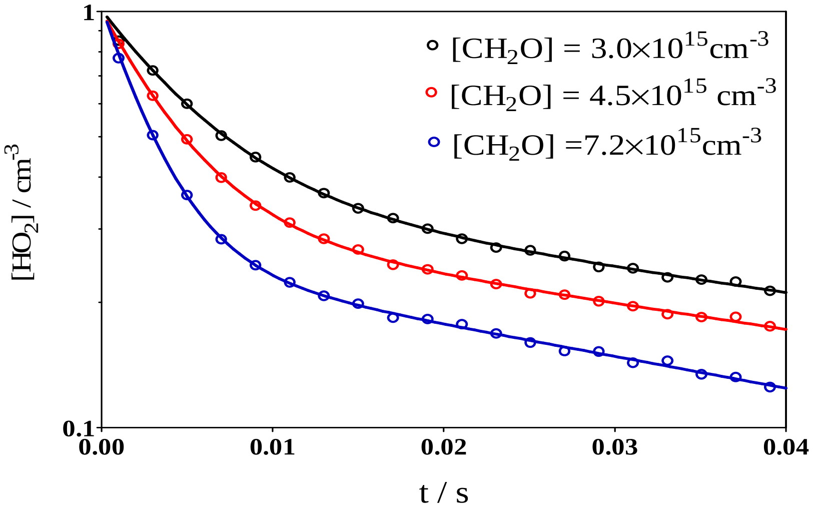

Figure 3. 8: Normalized HO_2 decay profiles as a function of formaldehyde concentration at 51 Torr total pressure, 297K and ~76 mJ cm^{-2} photolysis energy. Absolute, initial HO_2 concentrations were 2.0 / 2.5 / 2.7 $\times 10^{12}$ molecules cm^{-3} for lowest to highest formaldehyde concentration. Full lines represent fit to bi-exponential decay.

It can be clearly seen from Figure 3. 8 that not only the HO_2 decay becomes faster with increasing formaldehyde concentration, but also that the importance of the first, fast decay, i. e. $\%_{fast}$, increases with increasing formaldehyde: this behaviour, i.e. a decrease in the HO_2 equilibrium concentration, is expected for an equilibrium reaction. The bi-exponential fits of these three HO_2 decay profiles returned the following fit-parameters (from lowest to highest formaldehyde concentration): k_{fast} = 177±8 / 250±10 / 346±13 s^{-1}, k_{slow} = 13.3±1.3 / 14.6±1.3 / 15.6±1.2 s^{-1}, $\%_{fast}$ = 64.2±1.4 / 69.4 ±2.0 / 75.0 ±0.7 (errors are statistical only, 95% confidence interval). These results can be converted, using the above equations, into rate and equilibrium constants: k_1 = 4.04±0.4 / 3.86 / 3.65×10^{-14} $cm^3 molecule^{-1} s^{-1}$, k_{-1} = 64±6, 77, 83 s^{-1} and $K_{equilibrium}$ = 6.3±0.6 / 5.04 / 4.37 x 10^{-16} $molecule^{-1}$ cm^3. It can be seen that there is a systematic trend in the rate- and equilibrium constants: it seems that the HO_2-equilibrium concentration increases with increasing initial radical and/or formaldehyde concentration. This trend has been observed in all measurements. In order to be sure that the observed decay signals were purely due to HO_2 radicals, i.e. that the observed trend was not caused by an unexpected absorption of another species such as the adduct, experiments were performed by tuning the detection wavelength off any HO_2 absorption line so as to observe the possible absorption due to unknown species formed after the photolysis pulse (offline signal). However, no absorption signal was observed, confirming that the recorded decay profiles were very selective to HO_2 absorption and free of any other absorbing species at the wavelength of detection.

In the above described series of experiments, both the radical concentration and the formaldehyde concentration changed simultaneously. In order to separate the roles of both species in this systematic trend, we have performed experiments with identical formaldehyde concentration and different photolysis energy so as to vary the radical concentration only.

3.2.3.2 HO_2 decay as a function of photolysis laser energy

In order to investigate the influence of radical concentration on the evolution of the HO_2 decay, several series of experiments were performed by changing the photolysis laser energy at the same CH_2O and H_2O_2 concentration, typically varying the photolysis energy between 30 and 75 mJ cm^{-2}. The result of one such series is shown inFigure 3. 9:

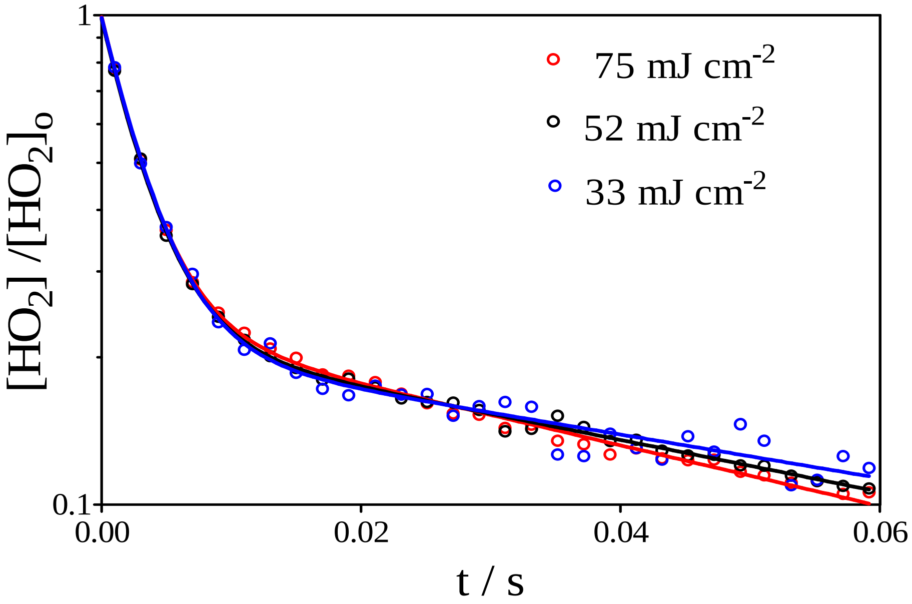

Figure 3. 9: HO_2 concentration time profiles as a function of photolysis laser energy at 51 Torr, 297 K and $[CH_2O] = 7.2 \times 10^{15}$ molecules cm^{-3}. Signals have been normalized by the photolysis energy for better comparison

Two observations can be made from Figure 3. 9:

- the HO_2 equilibrium concentration increases with increasing photolysis energy, visible through a decrease in the $\%_{fast}$ value obtained from bi-exponential fits. In the example of Figure 9, $\%_{fast}$ decreases from 78.8±1.2 to 77.6±0.6 to 76.3±0.5 (error is statistical only, 95% confidence interval) from lowest to highest photolysis energy. At identical k_{fast} and formaldehyde, this results in an apparently decreasing equilibrium constant with increasing initial radical concentration. The trend is therefore the same as in the experimental series with changing formaldehyde concentration and we can conclude that the initial radical concentration somehow influences the HO_2 equilibrium concentration.

- the bi-exponential fits of the three HO_2 decay profiles show that the slope of the slow HO_2 decay slightly increases with increasing photolysis laser energy. The slope in the example of Figure 3. 9 decreases from 14.6±0.7 to 12.6±0.8 to 10.5±2.1 from highest to lowest photolysis energy. The same trend has been observed from the bi-exponential fits in Figure 3. 8, the values of k_{slow} were found to decrease with decreasing formaldehyde concentration. The slow decay of the HO_2 radical concentration represents the loss of both radicals, HO_2 and $HOCH_2O_2$, out of the equilibrium, due to a cross-reaction of HO_2 with $HOCH_2O_2$, the self-reaction of both radicals as well as diffusion of both radicals out of the detection zone. As known from our experience with HO_2 measurements under similar experimental conditions, the loss due to diffusion can be well represented by an exponential decay at short reaction times. However, the diffusion of HO_2 is not expected to increase with increasing radical concentration. Therefore we conclude that the change in the initial radical concentration is at the origin of the slow decay.

3.2.3.3 Fitting HO_2 decays by a complex model

From the above results, i.e. changing formaldehyde concentration and the photolysis energy, we conclude that, the systematic trend in the apparent rate- and equilibrium constants is due to secondary chemistry, not taken into account when treating the equilibrium by the simple model described above. We therefore have re-analyzed the HO_2 decays using a more complex model taking into account some secondary chemistry.

Possible candidates for such reactions are the radical forming pathway of R2: this pathway for the reaction between the adduct $HOCH_2O_2$ and the HO_2 radical leads (under our conditions) rapidly to the formation of two new HO_2 radicals, i.e. one additional HO_2 radical that could impact on the observed equilibrium concentration. This pathway has been estimated by Jenkins et al.[8] to 20% and by Ngyuen et al. [10] to 15% of the total rate.

Another candidate is the self-reaction of the adduct, which has according to Burrows et al. [7] two different pathways:

$$2\ HOCH_2OO \rightarrow 2\ OHCH_2O + O_2 \qquad (R14a)$$

$$\rightarrow HCOOH + CH_2(OH)_2 + O_2 \qquad (R14b)$$

with $k_{14} = 5.9\times10^{-12}$ cm^3 molecule^{-1}s^{-1} and a branching ratio of 88% for the channel (R14a). The alkoxy radicals, formed in (R14a) will, in the presence of O_2, rapidly be transformed into formic acid and HO_2 radicals.

In order to verify if the observed HO_2 decays at short reaction times <10 ms, and with this the apparent HO_2 equilibrium concentration, are influenced by these two secondary reactions, a more complete mechanism was considered and simulations of the HO_2 decay profiles were performed using a home made “reaction simulator” : a lab view based numerical integrator which uses levenberg-marquardt algorithm. The mechanism used to simulate the HO_2 decay profiles is listed in Table 3. 2

Reaction	No.	k / cm^{3}molecule^{-1}s^{-1}	Reference
$OH + H_2O_2 \rightarrow HO_2 + H_2O$	R7	1.7×10^{-12}	[15]
$OH + CH_2O \rightarrow H_2O + HCO$	R13	8.5×10^{-12}	[15]
$HCO + O_2 \rightarrow HO_2 + CO$	R15	5.2×10^{-12}	[31]
$H + O_2 \rightarrow HO_2$	R16	2.95×10^{-14}	[30]
$2 HO_2 \rightarrow H_2O_2 + O_2$	R9	1.7×10^{-12}	[32]
$CH_2O + HO_2 \rightarrow HOCH_2O_2$	R1	3.3×10^{-14}	This work
$HOCH_2O_2 \rightarrow CH_2O + HO_2$	R-1	55 s^{-1}	This work
$HOCH_2O_2 + HO_2 \rightarrow$ Product $\rightarrow OH + HOCH_2O + O_2$	R2a-d R2c	9.6×10^{-12} 2.4×10^{-12}	[8, 33]
$2 HOCH_2O_2 \rightarrow$ Products $\rightarrow 2 HOCH_2O + O_2$	R 14a R 14b	7×10^{-13} 7×10^{-12}	This work
$HOCH_2O + O_2 \rightarrow HCOOH + HO_2$	R 5	3.5×10^{-14}	[6]
$HO_2 \rightarrow$ Diffusion	R12	7 s^{-1}	estimated
$HOCH_2O_2 \rightarrow$ Diffusion	R13	6 s^{-1}	estimated

Table 3. 2: The mechanism used for the simulation of the HO_2 decay profiles at 297 K

The rate constant for the diffusion of the HO_2 radical, R12, has been estimated by plotting the rate constants k_{slow} from the bi-exponential fits versus initial radical concentration and extrapolating versus zero radical concentration: k_{slow} includes the loss of radicals by diffusion out of the observation volume, but also due to loss of radicals by self-and cross reactions (R2 and R14). This extrapolation leads to an average value of 7 s^{-1} for all experimental series performed in this study, a value typically found for the diffusion of HO_2 radicals at around 50 Torr in this experimental set-up. The $HOCH_2O_2$ radical being bigger than the HO_2 radical, a slightly lower diffusion constant has been estimated based on the HO_2 diffusion loss rate. Using this mechanism, all HO_2 concentration time profiles carried out at 297 K could be simulated with a unique rate and equilibrium constant for the reaction of HO_2 with formaldehyde, namely $k_1 = 3.3 \times 10^{-14}$ cm^3 $molecule^{-1}s^{-1}$, $k_{-1} = 55$ s^{-1}, and hence $K_{eq} = 6.0 \times 10^{-16}$ $cm^3molecule^{-1}$. Different simulations are presented in Figure 10 in order to demonstrate the impact of the rate constants and branching ratios of (R2) and (R14) on the HO_2 concentration-time profiles.

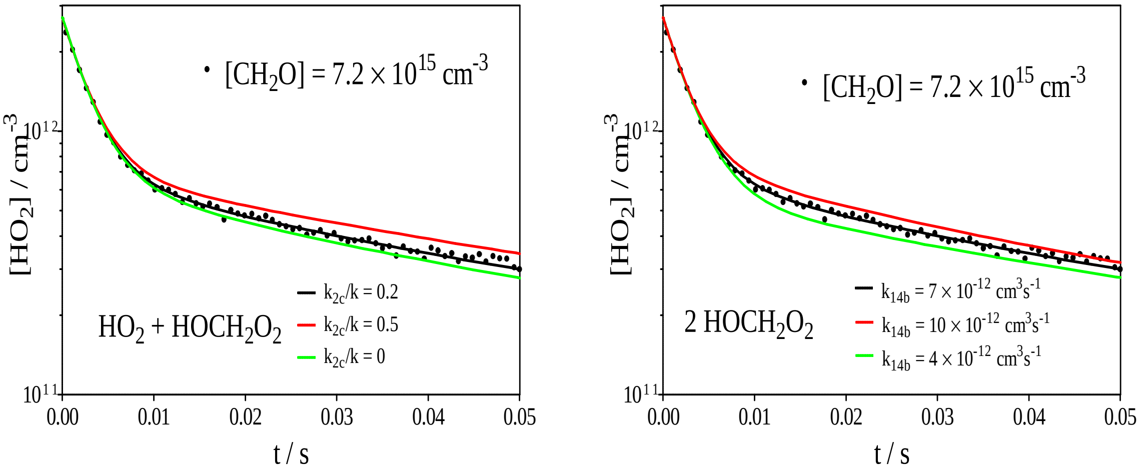

Figure 3. 10: Left graph, R2. Black line with the rate constants and branching ratios such as shown in table 2, red (upper) line $k_{2c}/k_2 = 0.5$, green (lower) line $k_{2c}/k_2 = 0$. Right graph:R14: black line with the rate constants and branching ratios such as shown in table 2, red (upper) line $k_{14b} = 10\times10^{-12}$ $cm^3molecule^{-1}s^{-1}$, green (lower) line $k_{14b} = 3\times10^{-12}$ $cm^3molecule^{-1}s^{-1}$

It can clearly be seen that both reactions have a stronger impact on the apparent HO_2 equilibrium concentration than on the HO_2 decay rate at longer reaction times. In order to reproduce all HO_2 concentration time profiles with one set of rate constants, the rate constant of R14b had to be slightly increased (7×10^{-12} $cm^3molecule^{-1}s^{-1}$) compared to the only available rate constant in the literature (5.5×10^{-12} $cm^3molecule^{-1}s^{-1}$) (Burrows et al. 1989).

3.2.3.4 Temperature dependence of the equilibrium constant

Experiments have been performed at different reaction temperatures so as to observe the change in the equilibrium constant as a function of temperature. Hence, a series of experiments were performed at 4 different temperatures between 292 and 306 K: at each temperature, the photolysis laser energy was varied between 35 and

75 mJ cm^{-2} for two or three different concentrations of formaldehyde, as explained in the above section. In the next step, the whole set of experiments was repeated at a different reaction temperatures. Typical experimental conditions employed for the measurements were $[CH_2O] = (1.5 – 7) \times 10^{15}$ molecules cm^{-3}, $[H_2O_2] = (1\text{-}1.5) \times 10^{14}$ molecules cm^{-3}, Laser energy = 30 - 75 mJ cm^{-2} leading to initial HO_2 concentrations of $(0.6 – 2.5) \times 10^{12}$ molecules cm^{-3}. The measured HO_2 decay profiles were subsequently fitted to the model described in

Table 3. 2. Figure 3. 11 represents the HO_2 decay profiles obtained with a formaldehyde concentration of around 5×10^{15} molecules cm^{-3} and 75 mJ cm^{-2} photolysis energy at different reaction temperature.

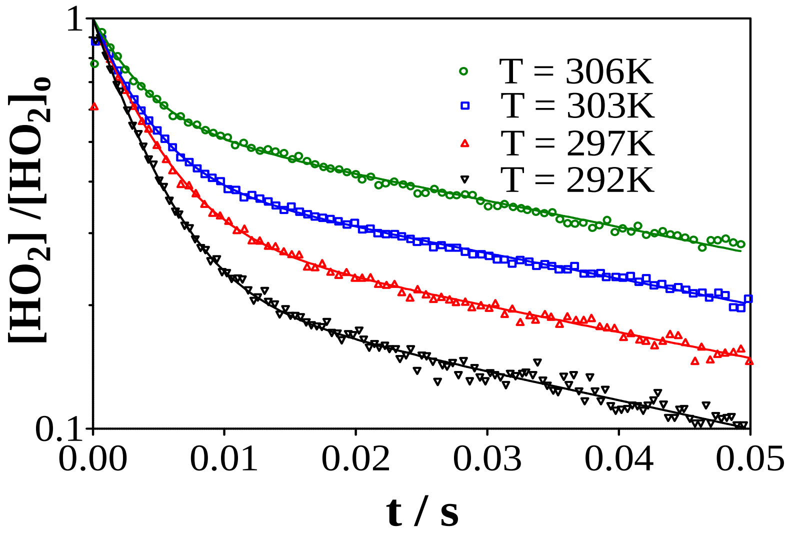

Figure 3. 11: Normalised HO_2 concentration time profiles as a function of reaction temperature.

It can be seen from Figure 3. 11 that the two decay slopes of the HO_2 concentration time profiles are clearly distinguishable at lower reaction temperatures (292 K) whereas with the increase in temperature it seems as if the second slope merges into the first slope and at reaction temperature of 306 K it becomes difficult to clearly distinguish the two slopes. In reality, it is not the slopes that change or merge together, but it is the back dissociation of $HOCH_2O_2$ that becomes faster with increasing temperature and hence the equilibrium concentration of HO_2 radicals become higher and higher. As a result the time window within which we can observe the forward reaction becomes smaller and smaller. This process limits the upper temperature range that can be exploited under our experimental conditions. On the other end, it would have been interesting to perform experiments at temperatures below 292 K: the back dissociation of $HOCH_2O_2$ slows down, which would allow obtaining higher concentrations of $HOCH_2O_2$ and thus a higher sensitivity to its reaction with HO_2 radicals and its self-reaction. Also, the equilibrium constant could have been evaluated over a larger temperature range. Unfortunately, with the present configuration of the experimental system it was not possible to reach temperatures below 292 K. So the temperature range over which the equilibrium could be studied was rather limited. Hence, HO_2 decay profiles have been measured at four different temperatures (292, 297, 303 and 306K), using two or three different initial formaldehyde concentrations at each temperature and three different photolysis energies at each CH_2O concentration. The forward (k_1) and the back dissociation (k_{-1}) and hence the equilibrium constant ($K_{equilibrium}$) have been determined at each reaction temperature from fitting the profiles to the full model.

The measured rate constants and the equilibrium constant such as obtained from these experiments for the different temperatures are presented in Table 3. 3**.**

T / K	**k_1 * (cm^3 $molecule^{-1}$ s^{-1})**	**k_{-1}* / s^{-1}**	**K_{eq} # ($molecule^{-1}$ cm^3)**
292	$(3.4 \pm 0.5) \times 10^{-14}$	35 ± 3.5	$(9.7 \pm 2.4) \times 10^{-16}$
297	$(3.3 \pm 0.5) \times 10^{-14}$	55 ± 5	$(6.0 \pm 1.45) \times 10^{-16}$
303	$(3.1 \pm 0.5) \times 10^{-14}$	90 ± 10	$(3.4 \pm 0.93) \times 10^{-16}$
306	$(3.0 \pm 0.5) \times 10^{-14}$	150 ± 20	$(2.0 \pm 0.6) \times 10^{-16}$

**: Error bar for k_1 and k_{-1} represents the range necessary to fit all experiments. #: Error bar for K_{eq} represents the total error combining both statistical and experimental error*

Table 3. 3: Experimentally measured k_1 and k_{-1} as a function of reaction temperature

The following temperature dependant expressions for the rate constants are obtained from a linear regression. However, given the very small temperature range accessible in our study, the obtained parameters are not reliable for extrapolation to other temperatures.

$$k_1 = 3.7 \times 10^{-15} \exp (637\ K/T)\ cm^3 molecule^{-1} s^{-1} \qquad \textbf{(E15)}$$

$$k_{-1} = 1.4 \times 10^{15} \exp (-9200\ K/T)\ s^{-1} \qquad \textbf{(E16)}$$

3.2.4 A comparison of the measured k_1, k_{-1} and K_{eq} with literature

The rate and equilibrium constants for the reaction between CH_2O and HO_2 have been measured several times at ambient temperature, but only once as a function of temperature. Veyret et.al. obtained the following Arrhenius equations:

$$k_1 = 7.7 \times 10^{-15} \exp (625\ K/T)\ cm^3 molecule^{-1} s^{-1} \quad \textbf{(E17)}$$

$$k_{-1} = 2.0 \times 10^{12} \exp (-7000\ K/T)\ s^{-1} \quad \textbf{(E18)}$$

Figure 3. 12 are shown the data for the association reaction from the literature together with the values measured in this work.

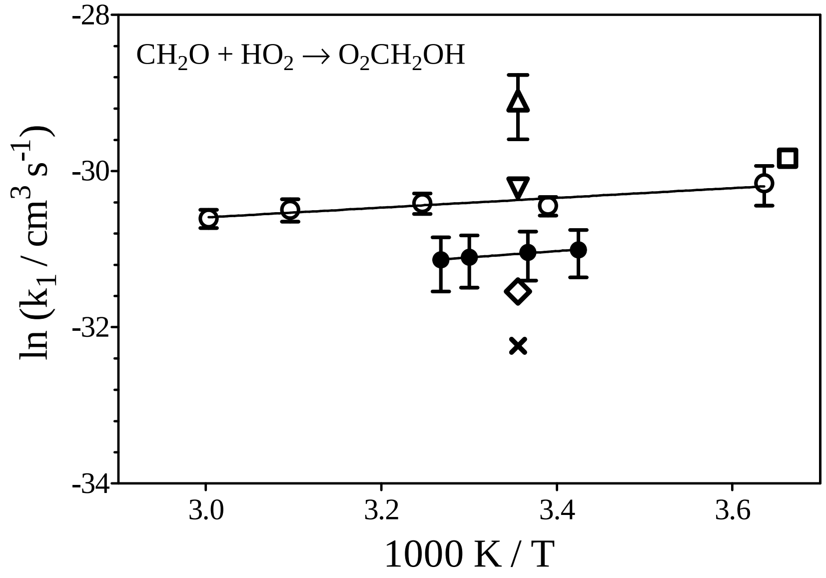

Figure 3. 12: Rate constants for the forward reaction k_1: (Δ) Morrison et al. [34], (□)Barnes et al.[9]), (∇) Mc Adams et al., [35],(◊)Thrush et al.[36], (×) Su et al., [1], (o) Veyret et al., [6], (●) this work (error bars for this work represent 30%)

The literature data at room temperature spread over more than one order of magnitude for the different studies. A comparison of the only temperature dependant study with the values obtained in this work show, that both studies find slightly negative temperature dependence. The absolute values obtained in our work are however systematically slower by around a factor of 2 compared to the work of Veyret et al. [6]. The available values for the back dissociation reaction are shown in Figure 3. 13. It can be seen that the rate constant obtained by Su et al. is very much slower than the other data. A comparison of our values with the only other temperature dependant study shows again, that the rate constants measured in this work are slower by around a factor of 2 compared to Veyret et.al. [6].

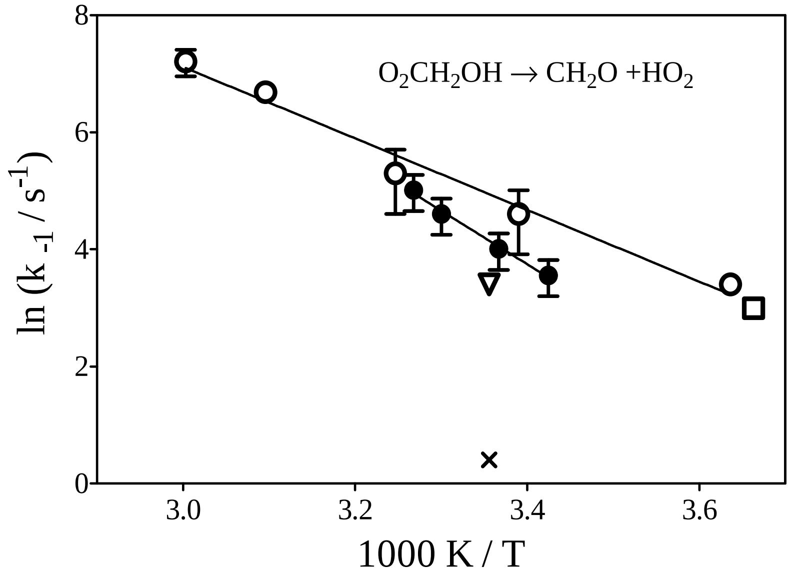

Figure 3. 13: Rate constants for the back reaction k_{-1}: (□)Barnes et al.[4]), (∇)Mc Adams et al., [35], (×) Su et al., [1], (o) : Veyret et al., [6], (●) this work (error bars for this work represent 30%)

The cause of the disagreement in the rate constants is not very clear. In this work, the rate constants were measured in a fairly direct manner, the major possible error in determining the rate constants being an error in determining of the formaldehyde concentration: the concentration was measured by its absorption at 6624.779 cm^{-1}, using the cross section (4.2 x 10^{-22} $molecule^{-1}cm^{-2}$) measured as a part of this study such as discussed in section 3.2.2. The estimated uncertainty on the measured absorption cross section is around ±20% and hence the observed disagreement of a factor of ~2 on the rate constants (k_1 and k_{-1}) can barely be explained by an error in the formaldehyde concentrations. Also, any error in the formaldehyde concentration would have a direct impact on the equilibrium constant: these values are however in excellent agreement with the value of Veyret et al. and Barnes et al. using the experimentally determined absorption cross section at 50 Torr (seeTable 3. 1). Another explanation could be found in the possibility that the reaction measured under our conditions (50 Torr He) is still in the fall-off range, while it is already in the high-pressure limit under the conditions of Veyret et al. (85 to 170 Torr of air). The rate constant of a comparable reaction, the decomposition of the ipropoxy radical, has been studied in a large range of pressure (10 – 45000 Torr He [37]) , and it was found that the reaction is still in the fall-off range. Therefore a factor of 2 in the rate constants between 50 Torr He and 85 Torr air is not completely unexpected. However, no pressure dependence was found by Veyret et al. in their pressure range, which is rather unlikely if the reaction at 50 Torr He would still be far in the fall-off. On the other hand, the raw data such as shown by Veyret et al. present a rather poor S/N ratio as well as a dead time of several hundred µsec due to the photolysis flash. It is therefore questionable if the time resolution of the experimental set-up was sensitive enough to obtain reliable rate constants: rise times of a few 100 µsec (pseudo-first order rate constant of up to 6000 s^{-1}) are expected under the high formaldehyde concentrations used in their experiments (up to 9×10^{16} molecules cm^{-3}).

The equilibrium constants K_{eq} such as obtained from the rate constants k_1 and k_{-1}, are in excellent agreement with the values obtained by Veyret et al.[6] and by Barnes et al.[9], as can be seen in Figure 3. 14. The equilibrium constant by Zabel et.al.[5] as well as the values from McAdam and Su et.al.[1] however are in poor agreement.

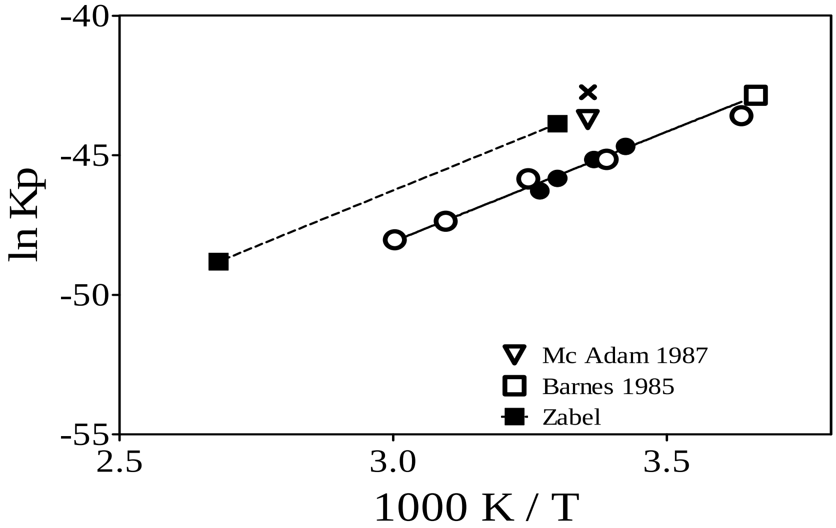

Figure 3. 14: Equilibrium constant as a function of temperature: same symbols as Figure 3. 12: (■)Zabel et al. Chem Phys Letter 1987, full line IUPAC recommended value for the equilibrium constant

A plot of the equilibrium constant as a function of temperature, the so-called van't Hoff plot, allows determining the change in the entropy (ΔS^0) and the change in the enthalpy (ΔH^0).

$$\ln K_p = -\frac{\Delta H^0}{RT} + \frac{\Delta S^0}{R} \qquad \textbf{(E19)}$$

where $K_p = K_{eq} \times (R \times T)^{\Delta n}$, T= temperature (K), R = gas constant in ($cm^3 atm K^{-1} mol^{-1}$) $\Delta n = \Sigma_{\text{number of products}} - \Sigma_{\text{number of reactants}}$, ΔH^0= the standard enthalpy change of the system at a given temperature T, and ΔS^0= standard entropy change of the system. Since the equilibrium constant was measured in this study over a small temperature range (292 K – 306 K) only, the determination of ΔH^0 over this small temperature range may not be reliable. However, it can be seen from Figure 3. 14 that the experimental data are in excellent agreement with values such as recommended by IUPAC.

3.3 Conclusion

The present study focuses on the chemistry of CH_2O + HO_2 radicals. In order to investigate the title reaction, it was necessary to measure absolute concentrations of formaldehyde. We decided to employ our cw-CRDS set-up and use the well-structured absorption features of formaldehyde in the near infrared for quantifying the formaldehyde concentration within the reactor. Since the formaldehyde absorption cross sections under the experimental conditions of this study in the near IR region were not known, experiments were performed to measure the absolute cross sections of two selected absorption lines of formaldehyde. It has been known that formaldehyde is a molecule difficult to handle as the monomer easily adsorbs on surfaces and also polymerizes. Hence, it is therefore not straightforward to prepare gas mixtures with a known concentration of formaldehyde. This difficulty was bypassed by applying a method that allows determining *in-situ* the concentration of formaldehyde through its reactivity against OH-radicals. The absorption spectrum of formaldehyde at two selected absorption lines of formaldehyde in the near IR region at 11 and 50 Torr He pressure was measured. These absorption peaks were fitted to a Voigt profiles from which the value of absorption coefficient at the maximum of the absorption peak was calculated. A plot of absorption coefficient vs formaldehyde concentration was plotted and the absorption cross section of formaldehyde was obtained from the linear regression. The pressure broadening of formaldehyde in He was determined from both pressures and by using the theoretical value of Doppler broadening for formaldehyde. The obtained cross sections of formaldehyde both at 11 and 50 Torr He at two different absorption lines were found to be ~ 2 times lower than the only values known in the literature (Staak et al. [23]). The observed disagreement was explained based on the possible errors in the formaldehyde concentration measurements of Staak et al. which were purely based on the measurement of formaldehyde pressure in a static cell.

The measured absolute cross sections were used to measure the formaldehyde concentrations employed in the kinetic study of $CH_2O + HO_2$ reaction using laser photolysis coupled to cw-CRDS technique. The reaction kinetics of $CH_2O + HO_2$ radicals were directly monitored by measuring absolute concentration - time profiles of HO_2 radicals as a function of photolysis laser energy and formaldehyde concentration at 297 K. The whole set of experiments were repeated at four different temperatures from 292 K – 306 K and the recorded time resolved HO_2 profiles were fitted to a model containing 14 reactions from which a consistent set of rate constants for all concentrations, laser photolysis energies and temperatures was obtained. The rate constant for the association reaction, the back dissociation rate constant and the equilibrium constant were determined at all four reaction temperatures employed in this study. The determination of the equilibrium constant was restricted to a small temperature range due to experimental limitations. While the measured values of K_{eq} were found to be in good agreement with earlier measurements from Veyret et al. and Barnes et al., the measured rate constant k_1 and k_{-1} were found to be ~ 2 times slower than the rather indirect measurements of Veyret et al and Barnes et al. [3, 5, 6, 9], on which the IUPAC committee is based for their recommendation.The reason for the observed disagreement is not known: it can be speculated that the HO_2 kinetic measurements could have been affected due to the significant absorption of the $HOCH_2O_2$ at the wavelengths at which HO_2 kinetics were recorded. Also, the time resolution of their experimental set-up may be not fast enough to reliably determine the fast kinetics. The use of cw-CRDS techniques employed in this study allowed a more direct and selective determination of HO_2 kinetics and hence the rate constants (k_1 and k_{-1}) and the equilibrium constant.

However, the reliable determination of the rate constant for the reaction of $HOCH_2O_2$ + HO_2 as well as the self-reaction of the $HOCH_2O_2$ radical was not possible for two reasons: (a) both reactions lead to a partial regeneration of HO_2 radicals and have thus only a limited impact on the HO_2 concentration time profile and (b) with the maximum radical concentrations employed in this study, both reactions occur relatively slowly at longer reaction times at which the diffusion of HO_2 radicals out of the detection zone becomes significant and the effect of HO_2 loss through both reactions (HO_2 + $HOCH_2O_2$ and $HOCH_2O_2$ self-reaction) is masked by the loss of HO_2 radicals due to diffusion. However, the reactions play a role in the determination of the equilibrium constant and rate constants in good agreement with an earlier determination by Veyret et al. allowed to simulate the HO_2 profiles under all experimental conditions.

3.4 Future Work

- The equilibrium constant needs to be validated over a lager temperature range.
- In order to do so, the experimental system needs to be modified with a better controlled heating and especially a cooling system that allows experiments over a larger temperature range, especially below room temperature.
- Better experimental conditions (especially lower temperatures) needs to be achieved so as to slow down the back dissociation of $HOCH_2O_2$ which would allow higher concentrations of $HOCH_2O_2$ in the reaction system and hence the better sensitivity can be achieved for the reaction of $HOCH_2O_2$ + HO_2. The possibility of OH production from the above reaction could then be evaluated.
- In order to verify the pressure dependence of the rate constants k_1 and k_{-1}, experiments must be carried out at different pressures. This would clarify whether or not; the difference in pressure is the cause of the observed disagreement between the rate constants measured in this study and those measured by Veyret et al.

3.5 References

1. F. Su, J.G. Calvert, J.H. Shaw, J. Phys. Chem. 83, 3185–3191 (1979).
2. H. Niki, P.D. Maker, C.M. Savage, L.P. Breitenbach: Chem. Phys. Lett. 72, 71–73 (1980).
3. B. Veyret, J.C.Rayez, R. Lesclaux, J. Phys. Chem. 86, 3424–3430 (1982).
4. I. Barnes, , K.H. Becker, E.H. Fink, A. Reimer, F. Zabel, H. Niki, Chem. Phys. Lett. 115, 1–8 (1985).
5. F. Zabel, K.A. Sahetchian, C. Chachaty, Chem. Phys. Lett. 134, 433–437 (1987).
6. B. Veyret, R. Lesclaux, M.T. Rayez, J.C. Rayez, R.A. Cox, G.K. Moortgat, J. Phys. Chem. 93, 2368–2374 (1989).
7. J.P. Burrows, G.K. Moortgat, G.S. Tyndall, R.A. Cox, M.E. G.D. Jenkin, Hayman, B. Veyret, J. Phys. Chem. 93, 2375–2382 (1989).
8. M.E. Jenkin, M.D. Hurley, T.J. Wallington, Phys. Chem. Chem. Phys. 9, 3149 (2007).
9. I. Barnes, K.H. Becker, E.H. Fink, A. Reimer, F. Zabel, H. Niki, Chem. Phys. Lett. 115, 1–8 (1985).
10. T.L. Nguyen, L. Vereecken, J. Peeters, J. Z. Phys. Chem. 224, 1081–1093 (2010).
11. J. Thiebaud, A. Aluculesei, C. Fittschen, J. Chem. Phys. 126, 186101–186101–2 (2007).
12. M. Staak, E.W. Gash, D.S. Venables, A.A. Ruth, J. Molec. Spect. 229, 115–121 (2005).
13. G.L. Vaghjiani, A.R. Ravishankara, J. Chem. Phys. 92, 996–1003 (1990).
14. G. Vaghjiani, A. Ravishankara: J. Geophys. Res. 94, 3487–3492 (1989).
15. R. Atkinson, D.L. Baulch, R.A. Cox, J.N. Crowley, R.F. Hampson, R.G. Hynes, M.E. Jenkin, M.J. Rossi, J. Troe, J. Atmos. Chem. Phys. 4, 1461–1738 (2004).
16. O. Johansson, J. Bood, M. Alden, U. Lindblad: Appl. Phys. B: Lasers and Optics. 97, 515–522 (2009).
17. D.L. Baulch, C.J. Cobos, R.A. Cox, C. Esser, P. Frank, T. Just, J.A. Kerr, M.J. Pilling, J. Troe, R.W. Walker, J. Warnatz: J. Phys. Chem. Ref. Data. 21, 411–429 (1992).

18. R. Atkinson, D.L. Baulch, R.A. Cox, J.N. Crowley, R.F. Hampson, R.G. Hynes, M.E. Jenkin, M. J. Rossi, J. Troe: Atmos. Chem. Phys. 6, 3625–4055 (2006).

19. A. Aluculesei, A. Tomas, C. Schoemaecker, C. Fittschen, Applied Physics B: Lasers and Optics. 92, 379–385 (2008).

20. C. Jain, P. Morajkar, C. Schoemaecker, B. Viskolcz, C. Fittschen, J. Phys. Chem. A. 115, 10720–10728 (2011).

21. M. Wojdyr: J. Appl. Cryst. 43, 1126–1128 (2010).

22. N. Ibrahim, J. Thiebaud,, J. Orphal, C. Fittschen: J. Mol. Spectrosc. 242, 64–69 (2007).

23. M. Staak, E.W. Gash, M. Staak, E.W. Gash: J. Mol. Spectrosc. 229, J. Mol. Spectrosc (2005).

24. M. Djehiche, A. Tomas, C. Fittschen, P. Coddeville: Environ. Sci. Technol. 45, 608–614 (2011).

25. C. Bahrini, O. Herbinet, P.-A. Glaude, C. Schoemaecker, C. Fittschen, F.d.r. Battin-Leclerc: Chem. Phys. Lett. 534, 1–7 (2004).

26. IUPAC Subcommittee on Gas Kinetic Data Evaluation – Data Sheet P1. (2002).

28. R. Atkinson, D.L. Baulch, R. A. Cox, J.N. Crowley, R.F. Hampson, R.G. Hynes, M.E. Jenkin, M.J. Rossi, J. Troe, .Atmos. Chem. Phys. 6, 3625–4055 (2006).

29. R. Atkinson, D.L. Baulch, R. A. Cox, J.N. Crowley, R.F. Hampson, R.G. Hynes, M.E. Jenkin, M.J. Rossi, J. Troe, J. Atmospheric Chemistry and Physics Discussions. 3, 6179–6699 (2003).

30. R.X. Fernandes, K. Luther, J. Troe, V.G. Ushakov, Phys. Chem. Chem. Phys. 10, 4313–4321 (2008).

31. R. Atkinson, D.L. Baulch, R. A. Cox, J.N. Crowley, R.F. Hampson, R.G. Hynes, M.E. Jenkin, M.J. Rossi, J. Troe: J. Atmos. Chem. Phys. 4, 1461 – 1738 (2004).

32. IUPAC suncommittee on Gas Kinetic Data Evaluation-Data Sheet HOx14. (2001).

33. T.L. Nguyen, L. Vereecken, J. Peeters, Z. Phys. Chem. 224, 1081–1093 (2010).

34. B. M. Morrison J. Heicklen: J. photochem. 15, 131 (1981).

35. K. McAdams, B. Veyret, R. Lesclaux, Chem. Phys. Lett. 133, (1987).

36. B.A. Thrush, G. S.Tyndall, J. Chem. Soc.-Faraday Trans. 2. 78, 1469 (1982).

37. P. Devolder, C. Fittschen, A. Frenzel, H. Hippler, G. Poskrebyshev, F. Striebel, Phys. Chem. Chem. Phys. 1, 675–681 (1999).

Chapter 4

248 nm photolysis of Acetaldehyde: quantum yields of H and HCO radicals

4 248 nm photolysis of acetaldehyde: Quantum yields of H and HCO radicals

4.1 Present understanding of the acetaldehyde photochemistry

Acetaldehyde is one of the important carbonyl compounds present in the atmosphere as its photodecomposition by sunlight generates free radicals which further influence the photochemistry of the troposphere [1]. The different sources by which acetaldehyde is emitted to the atmosphere has already been discussed in Chapter 1 section 1.3. Recent studies on atmospheric measurements of OVOCs by Singh et. al [2], revealed that acetaldehyde concentrations up to 100 ppt are found at altitudes of ~12 km. In a very recent study, average annual concentrations of 430±190 ppt are found for CH_3CHO in the tropic remote marine boundary layer [3] between 2006 and 2011. Current atmospheric models underestimate the CH_3CHO concentration by a factor of 10, rising to 40 during summer. This shows, that the sources and sinks of acetaldehyde are still not well understood. Hence it is important to further investigate the decomposition of acetaldehyde and its influence on the tropospheric chemistry.

The primary photodecomposition of CH_3CHO has been the subject of many experimental and theoretical studies since the early work of Leighton and Blacet [4]. Recently, Calvert et al. [5] have reviewed the studies on the photochemistry of acetaldehyde, which can occur by the following pathways:

$CH_3CHO + h\nu \rightarrow CH_3CHO^*$

$CH_3CHO^* \rightarrow CH_3 + HCO \qquad \lambda_{threshold} = 337\ nm \qquad \Phi_1$ (R1a)

$\rightarrow CH_4 + CO \qquad$ all $\lambda \qquad \Phi_2$ (R1b)

$\rightarrow CH_3CO + H \qquad \lambda_{threshold} = 320\ nm \qquad \Phi_3$ (R1c)

$\rightarrow CH_2CO + H_2 \qquad \lambda_{threshold} = 1027\ nm$ (R1d)

When acetaldehyde absorbs UV radiation (σ_{248nm} = (1.03±0.11)×10^{-20} cm^2 $molecule^{-1}$[6]), the increase in the internal energy raises the molecule from S_0 electronic ground state to the first excited electronic singlet state S_1, followed by subsequent energy redistribution by processes such as fluorescence, intersystem crossing (ISC) from S1 to neighboring triplet state T1, dissociation to form products and deactivation by collision quenching. In a more recent investigation, Moortgat et al.[7] have investigated the photolysis of acetaldehyde in the wavelength range of 255 - 335 nm and provided the wavelength dependent quantum yields for the products CO, CH_4 and CO_2. Based on the stable end product analysis using GC/FID, they have also calculated the quantum yields for the three photolysis processes R1a, R1b and R1c in the above mentioned wavelength range as follows:

$$\Phi_1 = \Phi\,(CO) - \Phi\,(CH_4)$$

$$\Phi_2 = \Phi\,(CH_4)$$

$$\Phi_3 = \Phi_{diss} - \Phi\,(CO)$$

$$\text{where } \Phi_{diss} = \Phi_1 + \Phi_2 + \Phi_3$$

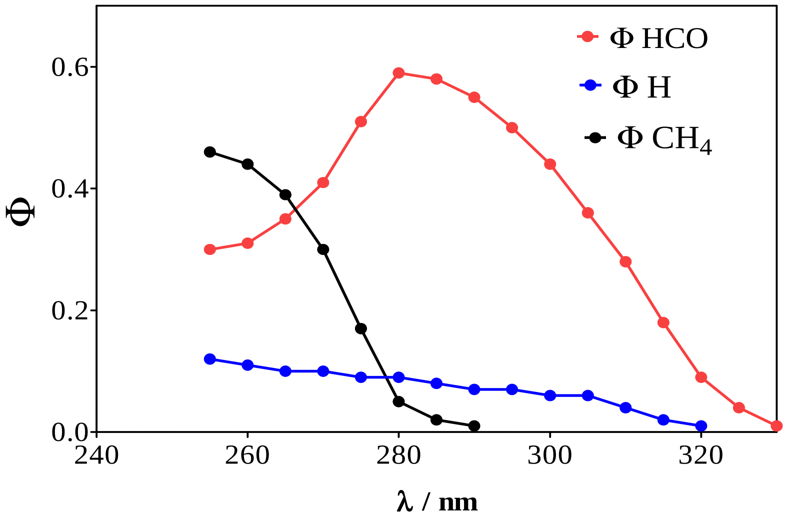

Figure 4. 1: Wavelength dependence of the quantum yield in air near atmospheric pressure [7]

Figure 4. 1 presents the wavelength dependent quantum yields at near atmospheric pressures measured by Moortgat et al. [7]. The radical forming

channels (R1a and R1c) are endothermic (the enthalpy changes, ΔH^o_{298}, are 355.3 and 373.5 kJ mol^{-1}, respectively) and the molecular channel (R1b) is exothermic and accessible to all wavelengths (ΔH^o_{298} = - 19.5 kJ mol^{-1}). The molecular channel (R1d), even though thermodynamically possible, has not been observed in the studies of Horowitz et al.[8] and the absence of H_2 product in the recent studies by Moortgat et al. [7] lead to an estimation of an upper limit for this channel ($\phi_{1d} \leq 0.01$). The quantum yields for the three primary photolysis channels reported by Moortgat et al., even though based on the observations of a series of experiments that were performed under different experimental condition, can be considered rather indirect: the quantum yields of the primary photolysis channels were assigned based on the measurement of stable end product analysis which requires an accurate and complete knowledge of the oxidation mechanism. Any error in the reaction mechanism could in turn lead to errors in the assigned quantum yields of the primary photolysis channels. Hence it is useful to measure the quantum yields of the primary photolysis channels in a more direct way.

Interestingly, two of the acetaldehyde photolysis channels produce HCO (R1a) and H atoms (R1c), both of which react with O_2 to produce HO_2 radicals.

$$HCO + O_2 \longrightarrow HO_2 + CO \qquad (R2)$$

$$H + O_2 \longrightarrow HO_2 \qquad (R3)$$

However, the rate constants for HCO + O_2 ($k_2 = 5.2 \times 10^{-12}$ $cm^3 molecule^{-1} s^{-1}$) [9] is two orders of magnitude greater than H + O_2 ($k_3 = 2.64 \times 10^{-14}$ $cm^3 molecule^{-1} s^{-1}$ at 50 Torr O_2) . This means that the contribution of HCO and H atoms to the evolution of the HO_2 concentration could be selectively obtained if one can measure time resolved absolute concentrations of HO_2 radicals. This provides the motivation for the present work as we can measure selectively absolute time resolved concentration profiles of HO_2 radicals using 248 nm excimer laser photolysis coupled to cw-CRDS technique.

4.2 Results and Discussion

The 248 nm photolysis of acetaldehyde was investigated by measuring the amount of HO_2 radicals that were produced in reaction R2 and R3. A mixture of CH_3CHO/He at a desired concentration was prepared in a glass balloon by filling a balloon with up to 100 Torr of CH_3CHO, far below the vapour pressure of acetaldehyde (754.4Torr at 293 K), and subsequent dilution with He. CH_3CHO is rather difficult to handle and subject to polymerisation. In order to verify the concentration of the CH_3CHO/He mixture, we have occasionally co-photolysed CH_3CHO and H_2O_2 at 248 nm and followed the decay kinetics of OH radicals in presence of large excess of CH_3CHO using LIF, thus measuring absolute CH_3CHO concentrations in a similar manner as in case CH_2O concentration determination discussed in the previous chapter 3. Using the OH decay rate and the well known rate constant for OH + CH_3CHO ($k=1.5 \times 10^{-11}$ $cm^3molecules^{-1}s^{-1}$), the concentration of CH_3CHO employed in the measurements were calculated. A good agreement (±15%) was obtained between the CH_3CHO concentration calculated from the OH decays and the one calculated using the concentration of CH_3CHO in the balloon. CH_3CHO (sigma Aldrich 99.99%), O_2 (Praxiar, 6.0), He (Praxiar, 6.0) were used without any further purification. All gas mixtures were introduced to the reactor using calibrated mass-flow controllers (Tylan FC260). The pressure within the cell was kept constant with a pressure controller (Leybold MR16) and monitored with a 8 – 1000 Torr baratron (M*K*S).

4.2.1 HO_2 radical concentration as a function of O_2

As explained earlier, the photolysis of CH_3CHO takes place via three major channels, two of which lead to the generation of the radicals HCO, H, CH_3 and CH_3CO. The HCO and H atoms produced in photolysis channels R1a and R1c were converted to HO_2 radicals through R2 and R3 by adding O_2 to the reaction mixture. The concentration – time profiles of the HO_2 radicals were measured as a function of O_2 concentration using cw-CRDS technique. It is known that CH_3CO in presence of O_2 leads to the production of OH radicals [10]. Hence LIF technique was employed in order to detect these OH radicals. However, under the experimental conditions of this study, [CH_3CHO] = (0.5 - 1.6) x 10^{16} cm^{-3} molecules, [O_2] = (0.017 - 3) x 10^{17} cm^{-3} molecules, the high CH_3CHO concentrations have possibly decreased OH concentration to below our detection limit (10^9 cm^{-3}) through their fast reaction with OH radicals. Hence, no OH radicals could be monitored using LIF. The experimental system employed in this study for the simultaneous measurement of OH and HO_2 using laser photolysis coupled to LIF and cw-CRDS has already been discussed in Chapter 2, section 2.1.6. The O_2 concentration in these experiments was carefully varied in order to understand the oxygen dependence of the HO_2 concentration, so that both reaction (R1a) and (R1c) could be observed directly and selectively as explained earlier. The effect of the O_2 concentration on the measured HO_2 concentration-time profile is discussed in the next section.

4.2.1.1 HO_2 concentration –time profile under low O_2 concentration

A typical HO_2 concentration-time profile under low O_2 condition is shown in Figure 4. 2

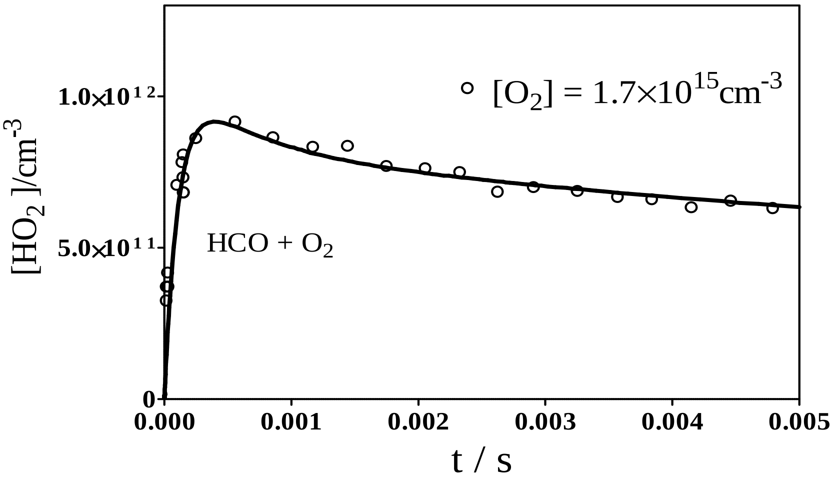

Figure 4. 2: HO_2 concentration time profile at 50 Torr under low O_2 condition. [CH_3CHO]= 1.6×10^{16} molecules cm^{-3}, [O_2] = 1.7×10^{15} molecules cm^{-3}, photolysis laser energy = 24.1±2 $mJcm^{-2}$.

The HO_2 decay profiles were simulated using a home made “reaction simulator”: the lab view based numerical integrator which uses the levenberg-marquardt fitting algorithm. Since the reaction of HCO + O_2 (k_5 = 5.2 x 10^{-12} cm^3 $molecule^{-1}$ s^{-1} [11]) is ~100 times faster than H + O_2 (k_3 = 2.6 x 10^{-14} cm^3 $molecule^{-1}$ s^{-1} at 50 Torr [12]), under low O_2 conditions of 1.7 x 10^{15} cm^{-3}, the rising profile of HO_2 radicals represents the kinetics of HCO + O_2 reaction forming HO_2. The H + O_2 kinetic is much slower and hence cannot be observed on the given time scale. The complete mechanism is listed in Table 4. 1. Hence, the experiments under low O_2 concentration allow selective determination of HCO quantum yields.

Reaction		Rate constant $cm^3molecule^{-1}s^{-1}$	Reference
$CH_3CHO + h\nu_{248nm} \rightarrow CH_3 + HCO$	R1a	Φ = 0.20±06	estimated
$\rightarrow CH_4 + CO$	R1b		
$\rightarrow CH_3CO + H$	R1c	Φ = 0.17±06	estimated
$HCO + O_2 \rightarrow HO_2 + CO$	R2	5.2×10^{-12}	[11]
$H + O_2 + M \rightarrow HO_2 + M$	R3	See text	[12]
$CH_3 + O_2 + M \rightarrow CH_3O_2 + M$	R4	See text	[13, 14]
$CH_3CO + O_2 + M \rightarrow OH + X^*$	R5a	See text	[10]
$CH_3CO + O_2 + M \rightarrow CH_3C(O)O_2$	R5b		
$CH_3O_2 + CH_3O_2 \rightarrow 2CH_3O + O_2$	R6a	1.3×10^{-13}	[9]
$\rightarrow (CH_3O)2$	R6b	$\}2.2\times10^{-13}$	
$\rightarrow HCHO + CH_3OH + O_2$	R6c		
$CH_3O + O_2 \rightarrow CH_2O + HO_2$	R7	2×10^{-15}	[15]
$CH_3O_2 + HO_2 \rightarrow CH_3OOH + O_2$	R8	5.2×10^{-12}	[9]
$CH_3CHO + OH \rightarrow CH_3CO + H_2O$	R9	1.4×10^{-11}	[9]
$CH_3O_2 + CH_3C(O)O_2 \rightarrow CH_3O + CH_3CO_2 + O_2$	R10a	9.9×10^{-12}	[9]
$\rightarrow CH_3COOH + CH_2O + O_2$	R10b	1.1×10^{-12}	
$CH_3C(O)O \rightarrow CH_3 + CO_2$	R11	5.4×10^{4}	[16]
$CH_3C(O)O_2 + HO_2 \rightarrow CH_3C(O)OOH + O_2$	R12a	5.47×10^{-12}	[9]
$\rightarrow CH_3C(O)OH + O_3$	R12b	2.1×10^{-12}	
$\rightarrow CH_3C(O)O + O_2 + OH$	R12c	6.16×10^{-12}	

$2CH_3C(O)O_2 \rightarrow 2CH_3C(O)O + O_2$	**R13**	1.6×10^{-11}	[9]
$CH_3 + CH_3 \rightarrow C_2H_6$	**R14**	6×10^{-11}	[17]
$HO_2 + HO_2 \rightarrow H_2O_2$	**R15**	1.7×10^{-12}	[18]
$CH_3O + CH_3CHO \rightarrow CH_3CO + CH_3OH$	**R16**	7×10^{-14}	[19]
$HO_2 + CH_3CHO \rightarrow CH_3CH(OH)O_2$	**R17**	2.1×10^{-14}	**estimated**
$CH_3CH(OH)O_2 \rightarrow HO_2 + CH_3CHO$	**R-17**	**1370**	**estimated**
$2CH_3CH(OH)O_2 \rightarrow 2CH_3CH(OH)O + O_2$	**R18a**	5.4×10^{-12}	[7]
$\rightarrow CH_3COOH + CH_3CHO + H_2O + O_2$	**R18b**	6.0×10^{-13}	
$2CH_3CH(OH)O_2 + CH_3O_2 \rightarrow CH_3CH(OH)O + O_2 + CH_3O$	**R19a**	1.8×10^{-12}	[7]
$\rightarrow CH_3COOH + CH_3OH + O_2$	**R19b**	1.2×10^{-12}	
$CH_3C(O)O_2 + CH_3CH(OH)O_2 \rightarrow CH_3CH(OH)O + CH_3 + CO_2 + O_2$	**R20**	1×10^{-11}	[7]
$CH_3CH(OH)O + O_2 \rightarrow CH_3COOH + HO_2$	**R21**	3.5×10^{-14}	[7]
$CH_3CH(OH)O_2 + HO_2 \rightarrow CH_3CH(OH)OOH + O_2$	**R22**	1.2×10^{-11}	[7]
$CH_3 + HO_2 \rightarrow OH + CH_3O$	**R23a**	3.2×10^{-11}	**estimatd**
$\rightarrow CH_4 + O_2$	**R23b**	5×10^{-12}	[20]
$H + CH_3CHO \rightarrow CH_3CO + H_2$	**R24**	1.1×10^{-13}	[21]
$H + HO_2 \rightarrow 2OH$	**R25**	7.2×10^{-11}	[11]
$HCO + H \rightarrow H_2 + CO$	**R26**	1.8×10^{-10}	[22]
$HCO + HO_2 \rightarrow$ **Products**	**R27**	5×10^{-11}	[23]
$HCO + CH_3 \rightarrow CH_4 + CO$	**R28**	2×10^{-10}	[23]
$CH_3O_2 + H \rightarrow OH + CH_3O$	**R29**	1×10^{-10}	[23]
$X + HO_2 \rightarrow$ **Products**	**R30**	9×10^{-12}	**estimated**
$CH_3 + CH_3CHO \rightarrow CH_4 + CH_3CO$	**R31**	4.9×10^{-18}	[17]
$H + CH_3 \rightarrow CH_4$	**R32**	$5.9\times10^{-29}\times$ [N]	[17]
$HO_2 \rightarrow$ **diffusion**	**R33**	$10 s^{-1}$ at 10Torr $7 s^{-1}$ at 50 Torr $5 s^{-1}$ at 90 Torr	**estimated**

Table 4. 1: Mechanism used to simulate the HO_2 profiles obtained from the acetaldehyde photolysis at 248 nm in presence of O_2. ** (**X**) represents an unknown product formed along with OH and (**N**) represents the number density at a give pressure.*

Under the acetaldehyde concentration of [CH_3CHO] = 1.67 x 10^{16} molecules cm^{-3}, the HO_2 radicals as soon as they are formed in the system, react rapidly with CH_3CHO in an equilibrium reaction forming $CH_3CH(OH)O_2$. This equilibrium will be discussed later separately in section 4.2.2.3 at the end of this chapter. Apart from the reaction of HO_2 with CH_3CHO, the decay the HO_2 decay profile was found to be sensitive mainly to the reaction of HO_2 with CH_3 radicals. CH_3 radicals are produced from the photolysis of CH_3CHO through channel (R1a). Hence the amount of CH_3 produced from photolysis is equal to the HCO concentration. However, the amount of CH_3 radicals available for the reaction with HO_2 depends on the amount of CH_3 lost through reactions other than with HO_2. The possible reactions of CH_3 radicals are listed in Table 4. 1. The loss of CH_3 radicals through its reaction with CH_3CHO is insignificant as the rate of this reaction is very slow ($k'_{CH3+CH3CHO} = 0.079\ s^{-1}$ [17]) and hence cannot be observed on the given time scale. The reaction of CH_3 radicals with O_2 to form CH_3O_2 is well known and its rate constant is pressure dependant under our conditions. The rate constant has been measured several times, but the rate constant under our experimental conditions (10 and 50 Torr He) has not been reported so far. Therefore we have constructed a fall-off curve in Helium as shown in Figure 4.3.

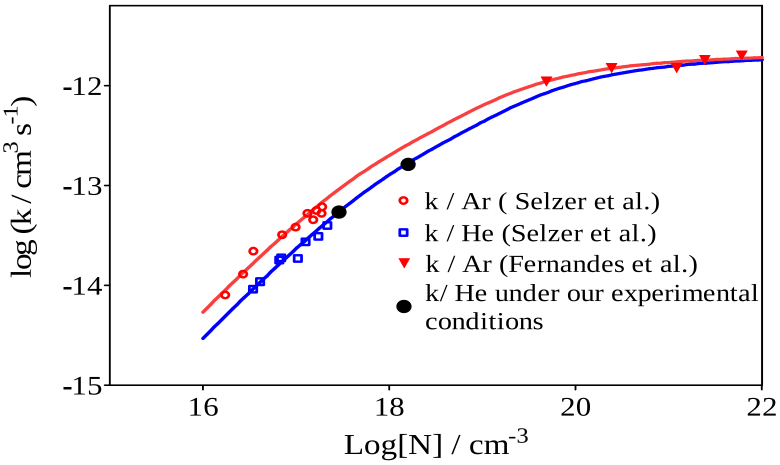

Figure 4. 3: Fall-off curve for the CH_3+O_2 reaction constructed using experimental values from reference [13]

Selzer et al. [14] have measured the rate constant in the pressure range 1 to 7 Torr using Helium and Argon as bath gas, while Fernandes et al. [13] have studied the reaction at high pressure (2 to 1000 bar) in Argon and N_2. Combining their values with Selzer et al., they obtained a high pressure limiting rate constants for CH_3 + O_2 of k_∞= 2.2 × 10^{-12} cm^3 $molecule^{-1}s^{-1}$ and a low pressure limiting rate constant for both, N_2 and Ar, of $k_{0,Ar,N2}$ =7×10^{-31} cm^6 $molecule^{-2}s^{-1}$ by using F_C=0.33 in the well-known Troe formalism [24]. In order to obtain the rate constant under our experimental conditions, to be used in our model, we have constructed a fall-off curve for k_{CH3+O2} in He by using the high-pressure value such as obtained by Fernandes et al. and a slightly lower broadening coefficient for Helium of F_C=0.3. The best fit to the experimental values of Selzer et al. in Helium is obtained with a low pressure limiting rate constant of $k_{0,He}$= 3.8×10^{-31} cm^6 $molecule^{-2}s^{-1}$ as shown in Figure 4. 3 . This results in rate constants of 5.4×10^{-14} cm^3 $molecule^{-1}s^{-1}$ and 1.63 × 10^{-13} cm^3 $molecule^{-1}s^{-1}$ in 10 and 50 Torr He, respectively, as summarized in Table 4. 2

Pressure (Torr)	**k_{CH3+O2} in He at 298K $cm^3 molecule^{-1}s^{-1}$**
10	5.4 x 10^{-14}
50	1.63x10^{-13}

Table 4. 2: Rate constant for CH_3+O_2 in He at two different pressures obtained from the plot of log k v/s log [P] using the fall off formalism from reference [13] .

Minor losses of CH_3 radicals also occur through its very fast reaction with HCO radicals ($k_{CH3+HCO}$= 2 x 10^{-10} $cm^3 molecule^{-1}s^{-1}$). However, HCO radicals are rapidly converted to HO_2 radicals even under the low oxygen condition to form HO_2 (more details in section 4.2.2.1). Hence, the loss of CH_3 radicals through this channel is only minor, especially during experiments with low radical concentration, i.e. low CH_3CHO concentration or low photolysis energy.

Under low O_2 concentration, the HO_2 decay profiles are influenced by its reaction with CH_3 radicals because under these conditions CH_3 radicals have a relatively long lifetime. This reaction can proceed via two different pathways, one generating new radicals (OH + CH_3O) and one leading to stable species (CH_4 + O_2) [20]. The reaction of CH_3 + HO_2 has been investigated through theoretical calculations by Jasper et al. [20]. They have determined rate constants for both channels and have obtained at 300 K a rate constant of k_{23} = 3.5 x 10^{-11} $cm^3 molecule^{-1}s^{-1}$ with a branching ratio of 0.72 for the radical channel R23a. The first experimental determination of the above reaction has recently been reported by Hong et al. [25]. They have determined the rate constant for k_{23a} = (6.8±1.4) x 10^{-12} $cm^3molecule^{-1}s^{-1}$ and k_{23b}= (4.4 ±2.1) x 10^{-12} $cm^3molecule^{-1}s^{-1}$ at reaction temperatures between 1000 and 1200 K, in excellent agreement with the reported values of Jasper et al. [20]. The simulation of the HO_2 profiles yielded a rate constant $k_{CH3+HO2}$ = (3.7±1.7) x 10^{-11} $cm^3molecule^{-1}s^{-1}$ under our experimental conditions, again in very good agreement with the theoretical calculations of Jasper et al. The branching ratios for the two channels R 23a and R23b could not be determined as we are not sensitive to the products of this reaction: even the radicals products OH and CH_3O will be, under the low O_2 concentrations, only slowly converted into HO_2 radicals. We therefore have implemented in our model the branching ratio such as proposed by Jasper et al. into the model listed in Table 4. 1 and the rate constant $k_{CH3+HO2}$ was determined by fitting to the full model. The sensitivity of the measured rate constant will be discussed later in the section 4.2.2.1. In order to observe the effect of high oxygen concentration, experiments were performed by changing the O_2 concentration in the reaction mixture. The results obtained are discussed in the next section.

4.2.1.2 HO_2 concentration- time profiles under high O_2 concentrations

Typical HO_2 profiles as a function of O_2 are shown in Figure 4. 4.

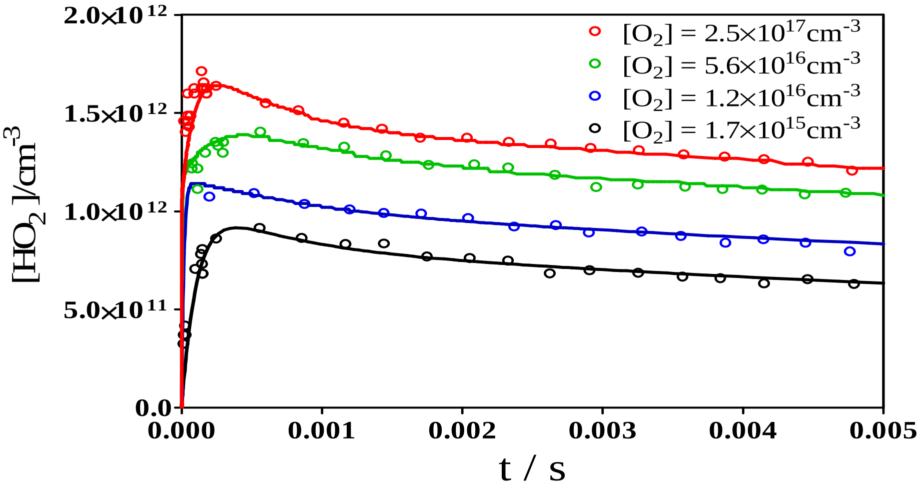

Figure 4. 4: HO_2 concentration time profiles as a function of O_2 at 50 Torr. [CH_3CHO] = 1.6 × 10^{16} molecules cm^{-3}, at photolysis laser energy of 24.1±2 mJ cm^{-2}. The open circle (o) represents experimental data and (–) represents the simulation obtained using the mechanism in Table 4. 1

An increase in O_2 concentration leads to a significant increase on the rate of the HCO + O_2 reaction. The reaction becomes so fast at O_2 concentrations of 5.6 x 10^{16} molecules cm^{-3} that the rising kinetic of HCO + O_2 can no longer be resolved under the time resolution of our instrument as can be seen in Figure 4. 4. Instead, we observed an initial HO_2 concentration which corresponds to the initial HCO radical concentration. Indeed, under these O_2 concentrations, the possible loss reactions for HO_2 or HCO become negligible and the observed initial HO_2 concentration corresponds to the yield of HCO formation, R1a. Also under these O_2 concentrations, a new kinetic corresponding to the H + O_2 reaction begins to appear on the measurement time scale. The kinetics of H + O_2 becomes clearly visible with further increase in the O_2 concentration up to 2.5 x 10^{17} molecules cm^{-3}.

Under these conditions the measured HO_2 concentration at short reaction times (<1ms) corresponds to the total HO_2 concentration, which is the sum of HCO + O_2 and H + O_2 forming HO_2. It is important to note that under these experimental conditions, significant amount of H atoms are lost through its reaction with CH_3CHO ($k'_{CH3CHO+H}$= 1760 s^{-1}). With the increase in the oxygen concentration, more and more H atoms are converted in to HO_2 radicals. However, even at the highest O_2 concentration employed in this study, ~20% of the total H atoms react with CH_3CHO to form CH_3CO + H_2. In addition to this, the increasing O_2 concentration also increases the scavenging effect of O_2 on CH_3 radicals, thus forming CH_3O_2 radicals. The reaction of CH_3O_2 + HO_2 ($k_{CH3O2\ +\ HO2}$ = 5.2 x 10^{-12} $cm^3molecule^{-1}s^{-1}$ [9]) being ~8 times slower than that of CH_3 + HO_2 ($k_{CH3\ +\ HO2}$ = (3.7 ±1.6) x 10^{-11} $cm^3molecule^{-1}s^{-1}$) results in less HO_2 being consumed on the measured time scale. However, this effect is counter balanced by the reaction of $CH_3C(O)O_2$ (acetyl peroxy) radicals with HO_2 (k_{12} = 1.37x10^{-11} $cm^3molecule^{-1}s^{-1}$ [9]). The reaction of $CH_3C(O)O_2$ radicals with HO_2 is known to proceeds via three reaction channels (see Table 4. 1) of which channel R12c generates OH radicals. These OH radicals once formed in the reaction system are rapidly consumed by CH_3CHO molecules present in large excess, leading to the formation of CH_3CO which in presence of O_2 regenerates $CH_3C(O)O_2$ radicals. In order to obtain better simulations, the rate constant for the reaction channel R12c had to slightly adjusted to 1x10^{-11} cm^3 $molecule^{-1}s^{-1}$ compared to the recommended value of 6.2

x 10^{-12} $cm^3 molecule^{-1} s^{-1}$ [9] . Apart from the reaction of $CH_3C(O)O_2$ with HO_2, there are other major loss channels of $CH_3C(O)O_2$ such as $CH_3C(O)O_2$ self reaction and the reaction with CH_3O_2 radicals which leads to loss of $CH_3C(O)O_2$ radicals from the radical pool. Since the mechanism could explain the observed HO_2 profiles under all experimental conditions, i.e. initial CH_3CHO concentrations, O_2 concentration and photolysis energy, the quantum yields for HCO and H atom can thus be obtained selectively by performing experiments under different O_2 concentrations. However, there are several factors which could affect the measured HO_2 concentration and hence the HCO and H yields which needs to be taken into account. An average value of the measured quantum yields of HCO and H atoms at 248 nm are presented in Figure 4. 5 along with the wavelength dependent quantum yields measured by Moortgat et al. [7]. The error bar represents a sum of both statistical and experimental error.

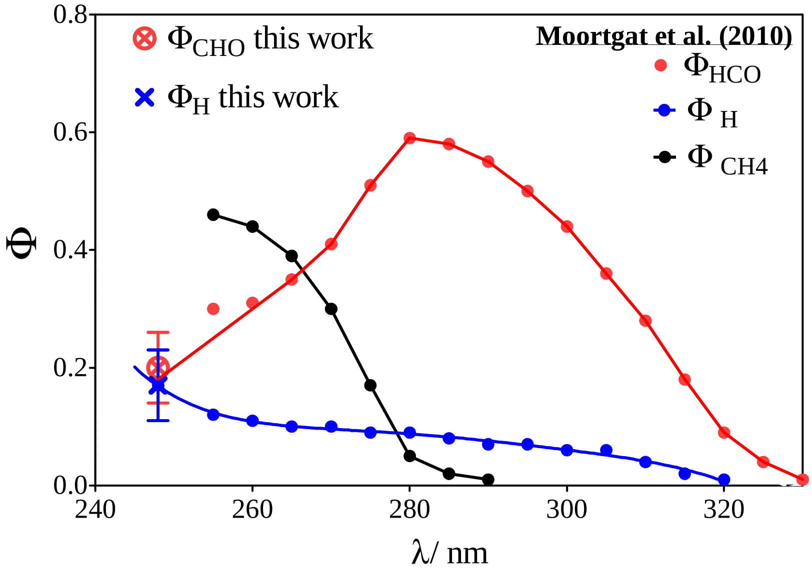

Figure 4. 5: Quantum yield of HCO and H at 248 nm (measured in this work) along with those measured by Moortgat et al. [7] at various wavelength.

4.2.2 Factors affecting the HCO and H quantum yields

Since the measured quantum yields of H and HCO depend on the amount of HO_2 radicals that have been detected using cw-CRDS, it is important to understand the different factors such as radical - radical reactions that consume H, HCO and HO_2. The equilibrium of $CH_3CHO + HO_2$ directly affects the measured HO_2 concentration and the pressure at which the experiments have been carried out could also be a factor contributing to the HO_2 concentrations as some of the reactions such as H + O_2 are pressure dependent. The effect of all the above parameters on the HCO and H atom quantum yields will be discussed in the next section.

4.2.2.1 Radical- radical reactions

The possible losses of HCO radicals through other radical-radical reactions such as H, CH_3 and HO_2 would lead to a decrease in the concentration of HO_2 radicals detected in the system. Such reactions are especially important under low O_2 concentrations, when the HCO lifetime is longer and under high photolysis energy when the overall radical concentration is high. Hence, HO_2 profiles were measured under low O_2 conditions as a function of photolysis laser energy at 50 Torr He. The radical-radical reactions discussed above (R25-R28) were added to the reaction model and HO_2 profiles were re-simulated to account for these losses. Figure 4. 6 shows different HO_2 profiles obtained as a function of photolysis laser energy.

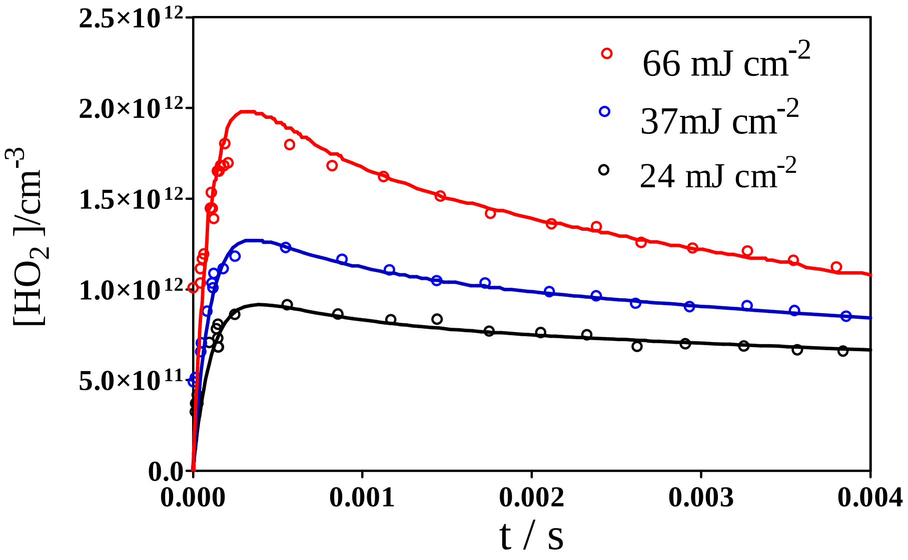

Figure 4. 6: HO_2 concentration-time profiles as a function of photolysis laser energy at 50 Torr. [CH_3CHO]= 1.67×10^{16} molecules cm^{-3}, [O_2] = 1.7×10^{15} molecules cm^{-3}.

As expected, the increase in the photolysis laser energy leads to an increase in the concentration of HCO radicals and H atoms which results in an increase in the measured HO_2 concentration. In order to understand the effect of change in the initial radical concentration on the HO_2 profile, a complete mechanism listed in Table 4. 1 was considered for simulations. Even though not all the reactions listed in Table 4. 1 have direct influence on the HO_2 profiles on the time scales considered here (<5 ms), yet they are considered in the model as these radical-radical reactions contribute to the change in the concentration of those radicals which react with HO_2 and hence need to be accounted for.

It can be seen from Figure 4. 6, that the model reproduces very well the measured HO_2 profiles under different initial radical concentration. This was expected as even at the lowest O_2 concentration employed in this study (1.7×10^{15} cm^{-3}), the pseudo first order rate constant, $k'_{HCO+O2} = 8840\ s^{-1}$ which is much greater $k'_{HCO+H} = 360\ s^{-1}$, $k'_{HCO+CH3} = 400\ s^{-1}$, $k'_{HCO+HO2} = 100\ s^{-1}$, $k'_{H+HO2} = 144\ s^{-1}$. The above pseudo first order rate constants were calculated assuming approximate concentration of [H], [CH_3] and [HO_2] = 2×10^{12} molecules cm^{-3}. All the above loss reactions together account for <10% of the HCO radicals being consumed. In reality, this is highly over estimated as concentrations of the above radicals (H, and CH_3) undergoing reaction with HCO will be much lower than the assumed value of 2×10^{12} molecules cm^{-3}, as there are other loss channels for the radicals H, and CH_3 as already discussed in the earlier section. Nonetheless, even these minor losses were accounted for during the simulations.

The increase in the photolysis laser energy results in an increase in the CH_3 radical concentration produced from the photolysis of acetaldehyde. This results in an increased sensitivity of the HO_2 profiles against the rate constant of the reaction of $CH_3 + HO_2$. Figure 4. 7 presents the results of the sensitivity test obtained by simulating the HO_2 profiles with three different rate constants chosen for $CH_3 + HO_2$ reaction. As can be seen clearly from Figure 4. 7 best simulation of the HO_2 profile is obtained with $k_{CH3+HO2} = 3.7 \times 10^{-11}$ cm^3 molecule^{-1}s^{-1}. Since consistent values for the rate constant $k_{CH3+HO2}$ are obtained under different experimental conditions, we extract a value for the $k_{CH3+HO2} = (3.7 \pm 1.7) \times 10^{-11}$ cm^{3}molecule^{-1}s^{-1}. It is trivial that the above rate constant value depends directly on the rate constant chosen for CH_3CHO + HO_2 radicals. However, the effect of CH_3 + HO_2 is only selective under low oxygen concentration while the reaction of CH_3CHO + HO_2 is independent of O_2. Hence, it is not possible to obtain good simulation without accounting for the reaction of CH_3 + HO_2.

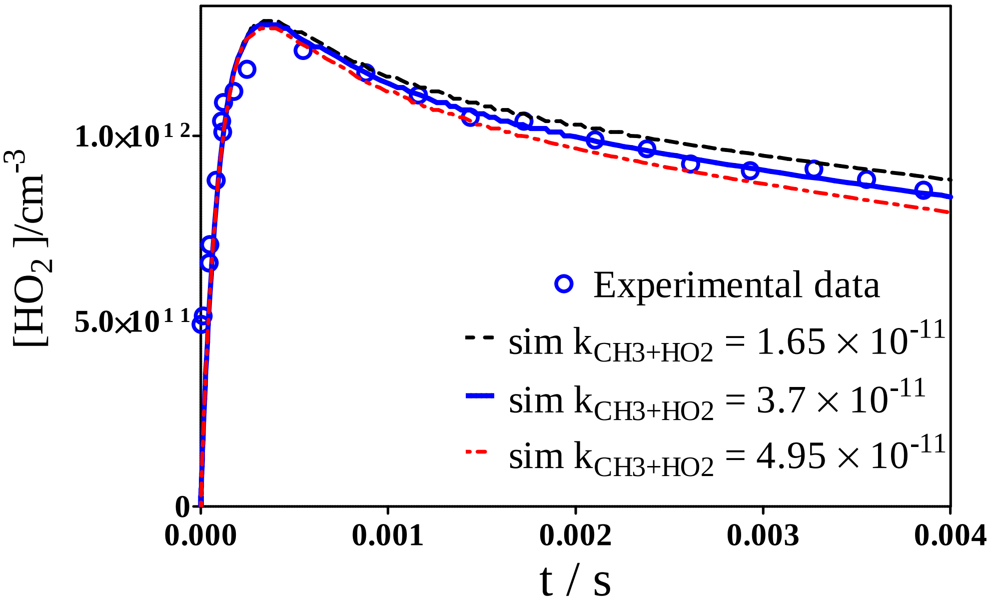

Figure 4. 7: Sensitivity test for CH_3+HO_2 rate constant obtained by simulating the HO_2 profile under low O_2 condition at 50 Torr. [CH_3CHO]=1.6×10^{16} molecules cm^{-3}, [O_2] = 1.7×10^{15} molecules cm^{-3} and laser energy = 37.1 mJcm^{-2}.

Similar experiments were performed by measuring HO_2 radical concentration as a function of photolysis laser energy at different O_2 concentrations. The chemistry under high O_2 concentrations from which the H atom yield has been obtained, remains unaffected by the change in the concentration of H and CH_3 as these radicals are immediately converted into HO_2 and CH_3O_2 in presence of O_2 as already explained in the earlier section. At the highest O_2 concentration employed in this study (2.5 x 10^{17} molecules cm^{-3}), k_{H+O2} = 8750 s^{-1}at 50 Torr and k'_{CH3+O2} = 35000 s^{-1}at 50 Torr respectively. It is important to mention here that the value of the rate constant for k_{H+O2} = 3.5 x 10^{-14} cm^3 molecule^{-1}s^{-1} at 50 Torr used in these simulations is slightly higher than the reported value of 2.6 x10^{-14} cm^3 molecule^{-1}s^{-1} [13]. The high rate constant value was necessary to fit the fast rise of HO_2 radicals under high O_2 concentration in all experimental conditions. A possible explanation is that in our system the O_2 and the CH_3CHO concentration are relatively high and not negligible against the He concentration (50 Torr ≈ 1.5×10^{18} cm^{-3}). Their collision efficiency is much higher than the collision efficiency of He, and therefore they should lead to an increase in the rate constants of pressure dependant reactions such as H + O_2.

4.2.2.2 HO_2 concentration-time profiles at different pressure

Since the mechanism listed in Table 4. 1 explains all the measured HO_2 profiles under different experimental condition such as O_2 concentration and photolysis laser energy at 50 Torr He, it was important to verify that the same model validates experiments at different pressures as well. Some of the reactions listed in Table 4. 1 are pressure dependent namely, H + O_2 and CH_3 + O_2. In addition to this, the branching ratio for the OH producing channel of the CH_3CO + O_2 reaction is favoured at low pressure. Hence, the entire set of experiments to measure HO_2 concentration profiles under different experimental conditions such as different O_2 concentration, photolysis laser energy and acetaldehyde concentration was repeated at 10 Torr He. The HO_2 concentration- time profiles as a function of O_2 concentration is shown in Figure 4. 8.

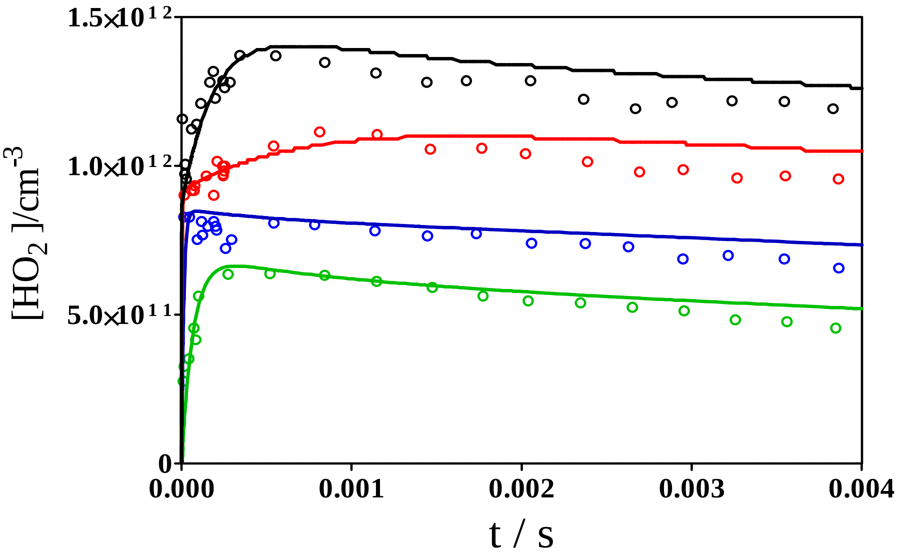

Figure 4. 8: HO_2 concentration time profiles under different O_2 concentration at 10 Torr, simulated using the mechanism listed in Table 4. 1. $[O_2]$ = 0.27, 1.5, 6.1 and 28×10^{16} molecules cm^{-3} from bottom to top, $[CH_3CHO] = 5.3\times10^{15}$ molecules cm^{-3}, laser energy = 67±2 $mJcm^{-2}$.

As can be seen from Figure 4. 8, the simulations obtained using the mechanism listed in Table 4. 1, reproduce very well the HO_2 profiles at short reaction times (<1 ms) under different O_2 concentrations. However, the observed HO_2 profiles decay faster at longer reaction time (> 1ms) compared to the simulations. This effect is found to increase with the increase in the O_2 concentration. Most of the rate constants listed in Table 4. 1 were obtained from either the recommendations of the IUPAC committee or from the NIST gas kinetic database [26]. An error in the extrapolation of a pressure dependant rate constant is not likely to be the reason of this disagreement: the rate constant for CH_3 + O_2 at 10 Torr was obtained from the fall-off curve plotted in Figure 4. 3. The fall-off is based on the experimental values measured by Selzer et al. at pressures less than 10 Torr and hence a large error in the extrapolation is not likely. Also, under higher O_2 concentrations, CH_3 radicals are rapidly converted into CH_3O_2 radicals (k'_{CH3+O2}= 15000 s^{-1}). Hence, any error in k_{CH3+O2} would not explain the faster decays of HO_2 at all O_2 concentrations. The same is true for the rate constant k_{H+O2} = 9 x 10^{-15} cm^3 $molecule^{-1}s^{-1}$ at 10 Torr: again, the rate constant was obtained by simulating the rise of HO_2 under different O_2 concentration and the obtained value, even thought slightly higher than the reported value of 6 x 10^{-15} cm^3 $molecule^{-1}s^{-1}$, is still comparable.

Another possible reaction influencing the HO_2 profile in the present system at low pressures could be the possible reaction of the co-product (X) of the OH forming channel R5a that might react with HO_2. Indeed, the co-product of the OH-forming channel in R5 is still not identified with certainty. As known from the literature [10], the OH yields from the CH_3CO + O_2 reaction increases with the decrease in pressure and so does the concentration of “X”. At 10 Torr (k_5 = 2 x 10^{-12} $cm^3molecule^{-1}s^{-1}$ [10]), ~ 76% of the total reaction of CH_3CO + O_2 leads to formation of OH (and “X”), while this yield is only 37 % at 50 Torr. Hence, a reaction between the product “X” and HO_2 would have a stronger impact on HO_2 profiles at lower pressure. Also, with the increase in O_2 concentration, the rate of CH_3CO + O_2 increases, i.e. the build-up of “X” becomes faster at higher O_2 concentration. This increases the observed effect of X + HO_2 on the time scale observed in our experiments. Hence by simulating the HO_2 profiles under different O_2 concentration, all experimental HO_2 profiles were best reproduced by a second order rate constant k_{X+HO2} = 9 x 10^{-12} $cm^3molecule^{-1}s^{-1}$. The simulations of the same HO_2 profiles as Figure 4.8. are shown in Figure 4. 9. As can be seen from Figure 4. 9, the reaction of X + HO_2 only contributes to the slight increase in the decay rate of HO_2 and does not have any significant effect on the measured quantum yield of HCO and H atoms obtained by simulating the HO_2 profiles at short reaction time (<1 ms).

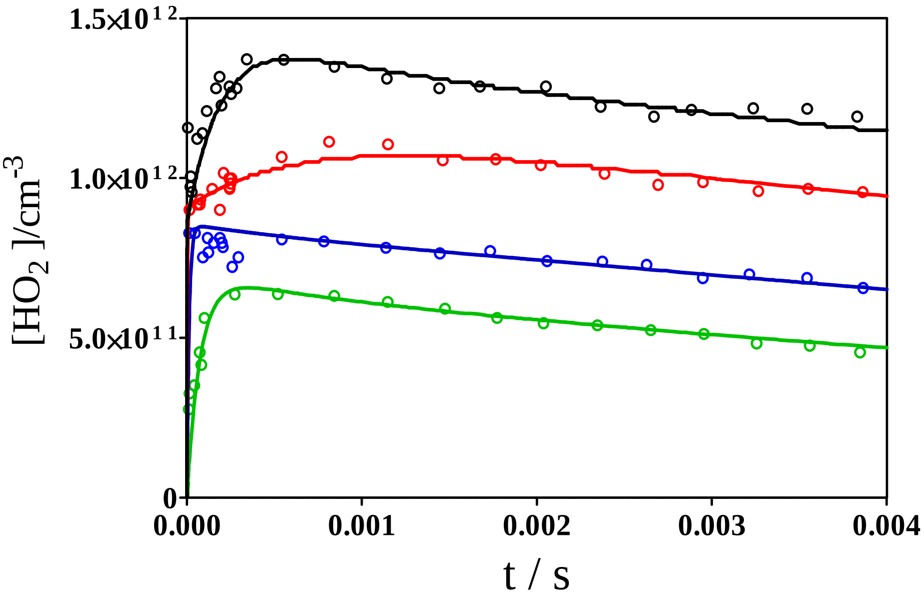

Figure 4. 9: Same HO_2 concentration-time profile as Figure 4.8, simulated including the reaction of X + HO_2, (k_{X+HO2} = 9 ×10^{-12} $cm^3molecule^{-1}s^{-1}$ to the existing mechanism listed in Table 4. 1.

The HO_2 profiles at 50 Torr were re-simulated taking into account the reaction of X + HO_2. Due to a significant decrease in the amount of X formed at 50 Torr, (~37% of the total reaction $k_{CH3CO+O2}$ = 2.8 x 10^{-12} $cm^3molecule^{-1}s^{-1}$ [10]) the change in the HO_2 decay rate induced by the addition of X + HO_2 reaction to the reaction model, was not as pronounced as at 10 Torr. However, the resulting decays were now slightly faster than before and hence, the rate constants for the reaction channel R12c which was earlier adjusted to 1 x 10^{-11} $cm^3molecule^{-1}s^{-1}$, was now readjusted to the original values (6.2 x 10^{-12} $cm^3molecule^{-1}s^{-1}$) recommended by IUPAC . The effect of X + HO_2 becomes almost insignificant at 90 Torr, as the amount of X produced at 90 Torr is ~20% of the total rate constant

($k_{CH3CO+O2}$ = 3.4 x 10^{-12} $cm^3molecule^{-1}s^{-1}$ at 90 Torr [10]). A comparison between the model simulations of HO_2 profiles at 10, 50 and 90 Torr with and without k_{X+HO2}= 9 x 10^{-12} $cm^3molecule^{-1}s^{-1}$ at each pressure is shown in Figure 4. 10.

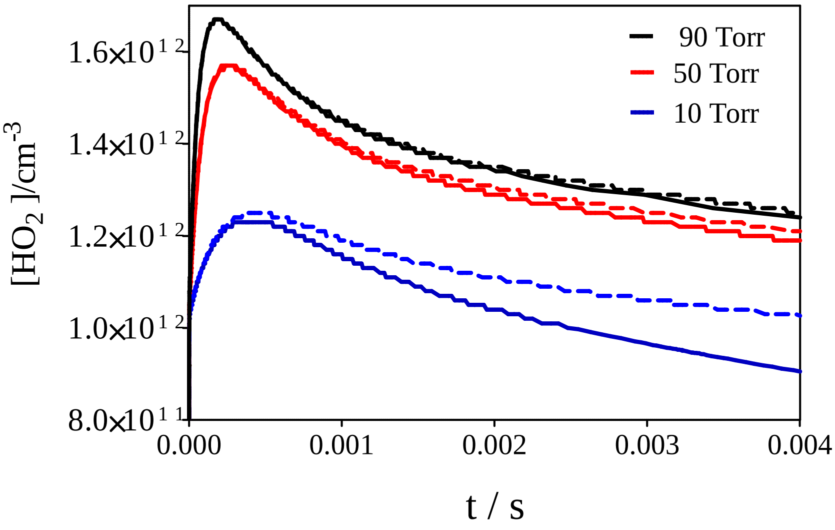

Figure 4. 10: Model simulations of HO_2 profiles at 10, 50 and 90 Torr in He. The solid line (—) indicates a simulation with $k_{X+HO2} = 9 \times 10^{-12}$ cm^3 $molecule^{-1}s^{-1}$ and (- -) indicates the simulation with $k_{X+HO2} = 0$, $[CH_3CHO] = 1.67\times10^{16}$ molecules cm^{-3}, $[O_2] = 2.5\times10^{17}$ cm^{-3} and laser energy = 24±2 $mJcm^{-2}$

The addition of $X+HO_2$ reaction not only explains the behaviour of all the measured HO_2 profiles under different pressure but it also validates the rate constant and the branching ratio for the reaction of $CH_3C(O)O_2$ + HO_2 as recommended by NIST. Since, similar quantum yields for HCO and H atoms were obtained from the simulations of the HO_2 profiles at different pressures, we can conclude that the quantum yields of HCO and H is independent of pressure in the range of 10-90 Torr in He. However, for better evaluation of the X + HO_2 reaction, it was important to perform experiments at pressures < 10 Torr. This was limited by the off set of our pressure gauge and hence could not be verified.

4.2.2.3 Equilibrium constant of $CH_3CHO+HO_2 \leftrightarrow CH_3CH(OH)O_2$ reaction

The equilibrium of CH_3CHO + HO_2 reaction has been experimentally explored my several research groups, Moortgat et al. [27], Crawford et al. [28] and Tomas et al.[29]. Many of these studies agree on the approximate value of the equilibrium constant K_{eq}= ~2 x 10^{-17} cm^3molecule^{-1} at 298 K. However, a large disagreement exists when it comes to the rate constants of the association reaction of CH_3CHO + HO_2 (k_{17}) and the back dissociation reaction (k_{-17}). The first estimate of k_{17} was provided by Moortgat et al. [27] by measuring the products of the CH_3CHO photolysis using FTIR and UV spectroscopy. They have reported k_{17} = 1 x 10^{-15} cm^3 molecule^{-1}s^{-1} assuming k_{-17}= 100 s^{-1} based on the yield of CH_3COOH. Contradicting the above results, in 1999, Crawford et al. [28] estimated k_{17} = 5 x 10^{-14} cm^3molecule^{-1}s^{-1}. Two years later (2001), another investigation of the title reaction was carried out by Tomas et al. [29] using flash photolysis time resolved UV spectroscopy. They have obtained from their study an equilibrium constant K_{eq} = 3 x 10^{-17} cm^3molecule^{-1} at 298 K with the rate constants being k_{17} = 4.4 x 10^{-14} cm^3molecule^{-1}s^{-1} and k_{-17} = 1470 s^{-1}. The above results were used by Moortgat et al. [7] in 2010 to explain the yields of the stable products obtained from the photolysis of CH_3CHO at different wavelengths (see Figure 4. 1). However, they had to lower the rate constant k_{17} to 1.5 x 10^{-14} cm^3molecule^{-1}s^{-1} in order to obtain better agreement to their experimental data.

Since the present work involves measurement of time resolved absolute concentrations of HO_2 radicals, produced from the photolysis of CH_3CHO, the system allows us to investigate directly the equilibrium constant of CH_3CHO + HO_2 reaction. Under the experimental conditions of this study, [CH_3CHO] = (0.5-1.67) x 10^{16} cm^{-3}, [HO_2]= ~2 x 10^{12} cm^{-3} at 298 K, HO_2 radicals rapidly react with CH_3CHO to enter an equilibrium forming $CH_3CH(OH)O_2$ radicals. In order to obtain reliable values of the rate of association reaction, it was important to perform experiments under different CH_3CHO concentrations.

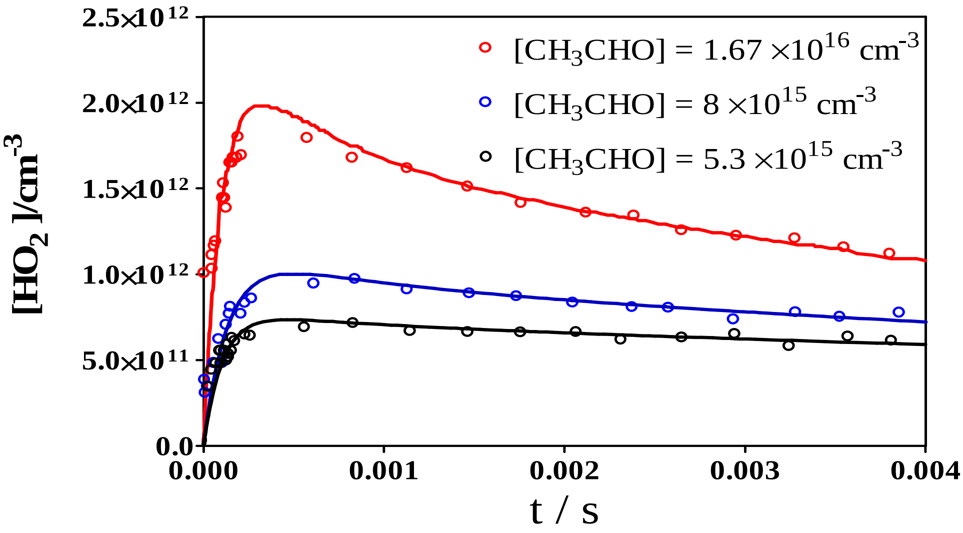

Figure 4. 11: HO_2 concentration time profiles as a function of CH_3CHO concentration. $[O_2]$ = 1.7 × 10^{15} cm^{-3}, photolysis laser energy = 66mJcm^{-2} at 50 Torr and 297K.

Figure 4. 11 presents different HO_2 concentration-time profiles measured as a function of CH_3CHO concentration. The HO_2 profiles under different acetaldehyde concentrations were simulated using the mechanism listed in Table 4. 1 and the rate constants k_{17} = 2.1 x 10^{-14} cm^3molecule^{-1} s^{-1} and k_{-17} = 1370 s^{-1} were obtained leading to an equilibrium constant K_{eq}= (1.5 ±0.4) x 10^{-17} cm^3 molecule^{-1} at 297 K. The measured rate constants were validated under different experimental conditions such as photolysis laser energy, O_2 concentration and pressure (see Figure 4. 4, Figure 4. 9 and Figure 4. 11). Even though, the equilibrium constant does not depend on the change in the above parameters, the HO_2 decay profiles does show significant change to the change in photolysis laser energy, O_2 etc. Since we were able to simulate all the HO_2 profiles under different experimental conditions with consistent set of rate constants for k_{17} and k_{-17}, we are confident that we can extract a reliable value of the equilibrium constant. The sensitivity test for k_{17} and k_{-17} is shown in Figure 4. 12 and Figure 4. 13, respectively. It can be seen from Figure 4. 12 and Figure 4. 13 that the best simulations under different O_2 conditions are obtained with k_{17} = 2.1 x10^{-14} cm^3molecule^{-1}s^{-1} and k_{-17} = 1370 s^{-1}. A similar observation was made from the experiments carried out at different photolysis laser energy. The measured value of k_{17} = 2.1 x 10^{-14} cm^3molecule^{-1}s^{-1} is in excellent agreement with the latest measurements of Moortgat et al., k_{17} = 1.5 x 10^{-14} cm^3molecule^{-1}s^{-1} [7].

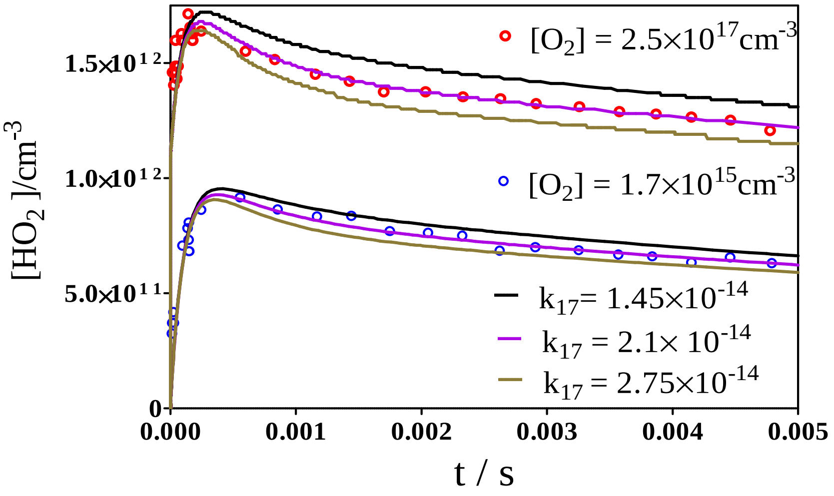

Figure 4. 12: Sensitivity test for k_{17}, three different rate constants were used for simulating the HO_2 profiles under two different O_2 concentrations using k_{-17} = 1370 s^{-1}. [CH_3CHO] = 1.67×10^{16} molecules cm^{-3}, photolysis laser energy = 24 mJcm^{-2} at 50 Torr.

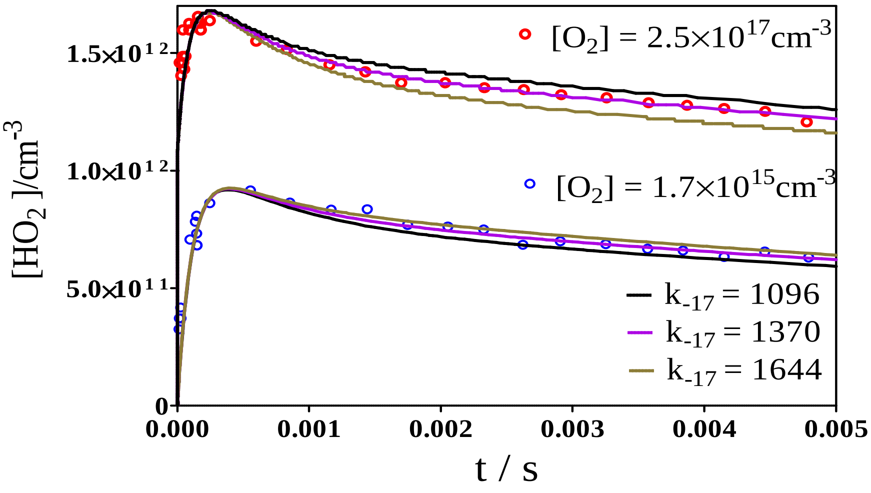

Figure 4. 13: Sensitivity test for k_{-17}, three different rate constants were used for simulating the HO_2 profiles under two different O_2 concentrations with k_{17} = 2.1 ×10^{-14} cm^{3}molecule^{-1}s^{-1}. [CH_3CHO] = 1.67×10^{16} molecules cm^{-3}, photolysis laser energy = 24 mJcm^{-2} at 50 Torr.

The measured value of the equilibrium constant K_{eq} = (1.5 ±0.4) x 10^{-17} cm^{3}molecule^{-1} is consistent with the value of ~ 2 x 10^{-17} cm^3 molecule^{-1}, well-accepted in the literature. However, the rate constant of the association reaction k_{17} and the equilibrium constant K_{eq} measured in this study do not agree with the values of the most recent experimental data obtained by Tomas et al. [29]: Figure 4.14 shows a simulation of HO_2 profiles with two different O_2 concentrations, comparing the values obtained in this work with those from Tomas et al.

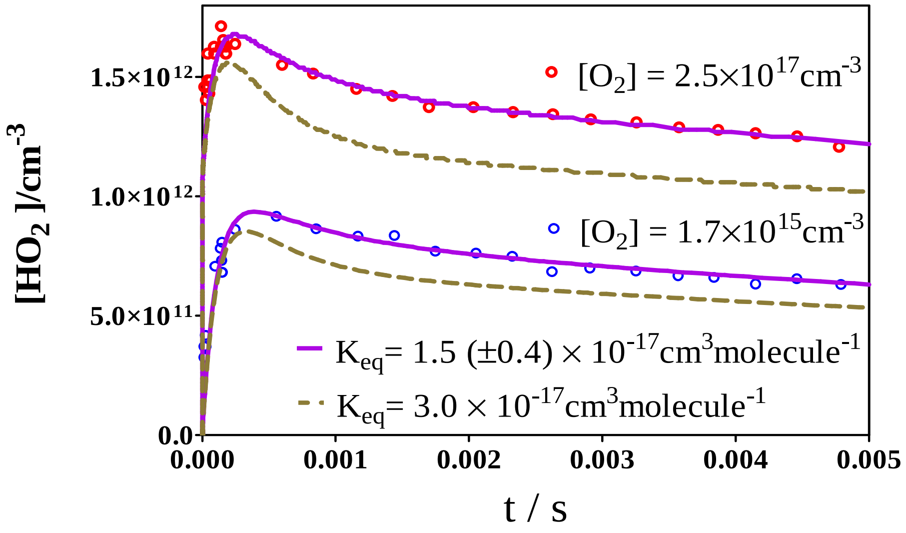

Figure 4. 14: A comparison between the simulations of HO_2 profiles under two different O_2 concentration, obtained using the Keq = 1.5×10^{-17} cm^{3}molecule^{-1}measured in this work and K_{eq} = 3 ×10^{-17} cm^{3}molecule^{-1} obtained from the work of Tomas et al. [29]. [CH_3CHO] = 1.67 ×10^{16} molecules cm^{-3}, photolysis laser energy = 24±2 mJcm^{-2} at 50 Torr.

However, the disagreement is not surprising as the rate constant k_{17} is estimated with an uncertainty of a factor of 2 in the measurements of Tomas et al. In order to validate the measured equilibrium constant, it was important to perform experiments at lower reaction temperatures as the back dissociation of $CH_3CH(OH)O_2$ at 297 K is very fast (k_{-17} = 1370 s^{-1}). An increase in reaction temperature would make the back dissociation even faster and hence would slow down the HO_2 decays substantially making it more difficult to observe k_{17} within the time window of our measurement. Hence experiments at lower reaction temperatures were desired. However, with the present configuration of the experimental setup this was not possible.

4.3 Conclusion

In the present work, the 248 nm photolysis of acetaldehyde was investigated. The HCO and H atoms produced through two of the known photolysis channels were converted into HO_2 radicals in presence of O_2 and the absolute time resolved HO_2 profiles were measured using cw-CRDS technique. The HO_2 profiles were simulated using a well known mechanism of acetaldehyde photolysis system in presence of O_2. The measured quantum yields of HCO and H atoms are 0.20 (±0.02) and 0.17 (±0.02) respectively. Different experimental conditions such as photolysis laser energy, O_2 concentration, acetaldehyde concentration and pressure were varied and their effect on the measured quantum yields were studied.

It was observed through simulations that the HO_2 radicals formed in the reaction system react with CH_3CHO (present in large excess) to enter an equilibrium forming $CH_3CH(OH)O_2$. The rate constant of the association reaction (k_{17} = $2.1 x 10^{-14}$ $cm^3 molecule^{-1} s^{-1}$), the rate constant of back dissociation (k_{-17} = $1370 s^{-1}$) and the equilibrium constant (K_{eq} = 1.5 (±0.4) x 10^{-17} $cm^3 molecule^{-1}$ were determined at 297K by simulating the HO_2 profiles under different experimental conditions mentioned above. The measured values of k_{17} and K_{eq} were found to be in good agreement with those reported by Moortgat et al. (k_{17} = 1.5 x 10^{-14} $cm^3 molecule^{-1} s^{-1}$ and K_{eq} = 2 x 10^{-17} $cm^3 molecule^{-1}$ [7]). In order to better evaluate the equilibrium constant, it would be necessary to perform experiments under lower reaction temperatures. However, this was not possible with the present configuration of the experimental setup.

Apart from the HO_2 + CH_3CHO equilibrium, the decay of HO_2 radicals were mainly sensitive to the reaction of CH_3 +HO_2, especially under low O_2 conditions ($1.7x10^{15}$ cm^{-3}). The rate constant for the reaction of CH_3 + HO_2 was determined by measuring HO_2 profiles under different experimental conditions mentioned above and by simulating the HO_2 decays at low O_2. The measured rate constant $k_{CH3+HO2}$ = (3.7 ±1.7) x 10^{-11} cm^3 $molecule^{-1} s^{-1}$ was found to be in good agreement with the reported values of 3.5 x 10^{-11} $cm^3 molecule^{-1} s^{-1}$ obtained by theoretical methods by Jasper et al.[20] and recently confirmed experimentally for the first time by Hong et al. [25] at high temperatures.

The decay of HO_2 radicals at low pressure (10 Torr) were found to be faster than those predicted by the known reaction model. The effect was found to slightly increase with the increase in O_2. Since this effect was clearly visible at lower pressures (10 Torr) and with the increase in pressure the effect was relatively less significant, it can be speculated that the reaction of an unknown product (X) formed as a co-product to the OH radical in the reaction of CH_3CO+O_2 radicals, could react with HO_2. This assumption was found to explain very well the observed HO_2 profiles under different O_2 concentrations, CH_3CHO concentrations and at different pressures and also indirectly validated the rate constant and the branching ratios for the CH_3CO+O_2 reaction recommended by IUPAC. However, this channel needs further investigation and no conclusive, definitive results can be drawn about this reaction at this stage of the work. Nonetheless, this reaction only affects the decays of HO_2 at long reaction times and has no influence on the measured quantum yields of HCO and H atoms.

4.4 Future work

- The study of quantum yield measurement of HCO and H atoms can be extended to other photolysis wavelengths in order to compare and verify the HCO and H atom yields measured by Moortgat et al.[7].
- The rate constant of CH_3 + HO_2 need to be re-measured under high CH_3 radical concentration, so as to obtain better sensitivity to validate this reaction channel.
- The equilibrium constant of HO_2 + CH_3CHO reaction needs to be validated over a larger temperature range.
- The suspicious reaction of the unknown product (X) with HO_2 needs more detailed investigation, especially under very low pressures in order to verify if the decay rate of HO_2 increases further with decrease in pressure or not. This would help to validate the existence of this suspicious reaction.

4.5 References

1. J. G. Calvert, J. N. Pitts: Photochemistry. Wiley, New York (1966).

2. H. B. Singh, L. J. Salas, R. B. Chatfield, E. Czech, A. Fried, J. Walega, M. J. Evans, B. D. Field, D. J. Jacob, D. Blake, B. Heikes, R. Talbot, G. Sachse, J. H. Crawford, M. A. Avery, S. Sandholm, H. Fuelberg. J. Geophys. Res. D. 109, (2004).

3. K.R. Read, L. Carpenter, S.R. Arnold, R. Beale, P. Nightingale, J.R. Hopkins, A.C. Lewis, J.D. Lee, L. Mendes, S. Pickering, J. Environ. Sci. Technol. (2012).

4. F. E. Blacet, P. A. Leighton, J. Am. Chem. Soc. 55, 1766 (1933).

5. J.G. Calvert, R.G. Derwent, J.J. Orlando, G.S. Tyndall, T.J. Wallington: Mechanism of atmospheric oxidation of alkanes. Oxford University Press, Oxford, New York, (2008).

6. S.P. Sander., J. Abbatt, J.R. Barker, J.B.Burkholder, R.R.Friedl, D.M. Golden, R.E.Huie, C.E.Kolb, M.J.Kurylo, J.K.Moortgat, V.L.Orkin, P.H.Wine. JPL Publication 10-6, Evaluation No. 17. (2011).

7. G.K. Moortgat, , H. Meyrahn, P. Warneck, Chem.Phys.Chem. 11, 3896–3908 (2010).

8. A. Horowitz, C.J. Kershner, J.G. Calvert, J. Phys. Chem. 86, 3094–3105 (1982).

9. R. Atkinson, D.L. Baulch, R.A. Cox, J.N. Crowley, R.F. Hampson, J.A. Kerr, M.J. Rossi, J. Troe: Atmos. Chem. Phys. 6, 3625–4055 (2006).

10. S.A. Carr, M.T. Baeza-Romero, M.A. Blitz, M.J. Pilling, D.E. Heard, P.W. Seakins, Chem. Phys. Lett. 445, 108–112 (2007).

11. R. Atkinson, D.L. Baulch, R.A. Cox, J.N. Crowley, R.F. Hampson, R.G. Hynes, M.E. Jenkin, M.J. Rossi, J. Troe, Atmos. Chem. Phys. 4, 1461–1738 (2004).

12. R.X. Fernandes, K. Luther, J. Troe, V.G. Ushakov, Phys. Chem. Chem. Phys. 10, 4313–4321 (2008).

13. R. X. Fernandes, K. Luther, J. Troe. J. Phys. Chem. A. 110, 4442–4449 (2006).

14. K. D. Bayes, E. A. Selzer. J. Phys. Chem. 87, 392–394 (1983).

15. IUPAC Subcommittee on Gas Kinetic Data Evaluation – Data Sheet RO_1. (2003).

16. Y.Z. Zhou, S. Li, Q.S. Li, S.W. Zhang, THERMOCHEM. 854, 40–45 (2008).

17. D.L. Baulch, C.J. Cobos, R.A. Cox, C. Esser, P. Frank, Th. Just, J.A. Kerr, M.J. Pilling, J. Troe, R.W. Walker, J. Warnatz, J. Phys. Chem. Ref. Data. 21, 411 – 429 (1992).

18. S.P. Sander, J. P.D. Abbatt, J.R. Barker, JPL publications. 10–6 (2011).

19. C. Fittschen, B. Delcroix, N. Gomez, P. Devolder, J. de Chimie Physique et de Physico-Chimie Biologique. 95, 2129–2142 (1998).

20. A. W. Jasper, S. J. Klippenstein, L. B. Harding: Fall Meeting of the Western States Section of the Combustion Institute Sandia National Laboratories, , Livermore, CA 17/10 (2007).

21. K. Ohmori, A. Miyoshi, H. Matsui, N. Washida, J. Phys. Chem. 94, 3253–3255 (1990).

22. G. Friedrichs, J.T.Herbon, D.F. Davidson, R.K. Hanson, Phys. Chem. Chem. Phys. 4, 5778–5788 (2002).

23. W. Tsang, R.F. Hampson, J. Phys. Chem. 15, (1986).

24. J.Troe, J. Phys. Chem. 83, 114–126 (1979).

25. Z. Hong, F. Davidson, K.-Y. Lam, R.K. Hanson, Combustion and Flame. 159, 3007–3013 (2012).

26. R. Atkinson, D.L. Baulch, R.A. Cox, J.N. Crowley, R.F. Hampson, R.G. Hynes, M.E. Jenkin, M.J. Rossi, J. Troe, Atmos. Chem. Phys. 6, 3625–4055 (2006).

27. G.K. Moortgat, R.A. Cox, G. Schuster, J.P Burrows, G.S. Tyndall, J. Chem. Soc., Faraday Trans. 2. 85, 809–829 (1989).

28. M.A. Crawford, T.J. Wallington, J.J. Szente, M.M. Maricq, J.S. Francisco, J. Phys. Chem. A. 103, 365–378 (1999).

29. A. Tomas, E. Villenave, R. Lesclaux, J. Phys. Chem. A. 105, 3505–3514 (2001).

Chapter 5

OH initiated oxidation of Hexamethyl benzene

5 OH initiated oxidation of Hexamethylbenzene

5.1 The present understanding of the OH initiated oxidation mechanism of aromatic compounds

Aromatic hydrocarbons are a major class of anthropogenic compounds emitted into the troposphere, with major sources being automobile exhaust, petroleum refining processes, and industrial solvent evaporation [1]. The mono-aromatic compounds (i.e. mainly benzene, toluene, xylene and trimethylbenzenes) may account for up to 20-40% of the total non-methane hydrocarbon content of the atmosphere especially in urban areas [1]. This individual class of compounds may reside in the atmosphere at low ppb levels. However, their high reactivity towards OH radicals makes them one of the major contributors to photochemical smog and ozone formation [2], [3].

5.1.1 Initial stages of aromatic oxidation

The dominant loss processes of these mono-aromatics in the troposphere are their gas-phase reactions with OH radicals. Depending on their degree of alkylation, such a process can proceed either by H-atom abstraction from a substituent group or by OH addition to the aromatic ring, the H-atom abstraction accounting at ambient temperature for less than 10% of the overall OH radical reactions for toluene, xylenes, and trimethylbenzenes [3], [4]. The major primary oxidation product is hydroxycyclohexadienyl radical or its alkylated derivatives formed by addition of an OH radical on aromatic ring, at the ortho, meta or para positions. The ortho OH addition to the aromatic ring has been considered to be the dominant channel [2, 5]. A simplified reaction scheme that explains the primary oxidation steps in case of Toluene is shown in Figure 5. 1.

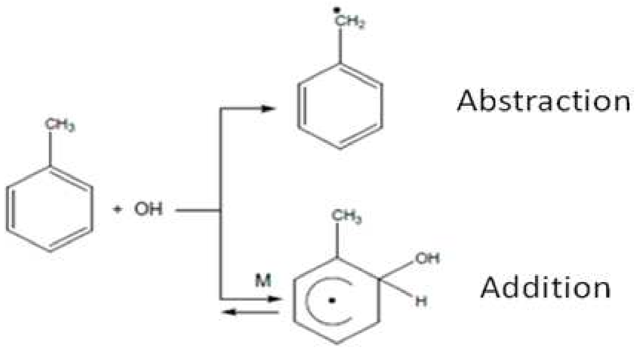

Figure 5. 1: Primary oxidation steps involved the OH initiated oxidation of Toluene [6]

5.1.2 Primary product yields from aromatic oxidation

Various studies have been performed so far on the OH initiated oxidation of aromatic compounds and the identification of potential products. These are summarized in the reviews on aromatic oxidation mechanisms in reference [1], [3]. In case of benzene, it has been understood that the reaction kinetics of aromatic-OH adduct with O_2 are consistent with the reversible formation of peroxy radicals [7]. Another possibility is the irreversible reaction of aromatic-OH adduct with O_2, directly forming products. However, the major problem in validating this pathway is that both the above pathways lead to the formation of phenol for benzene and cresol in case alkyated monoaromatics as the primary ring retained product of aromatic oxidation. Average phenol yields (0.53± 0.15) [8, 9] have be obtained from various studies and are well established. An example of the latest OH initiated benzene oxidation mechanism has been shown in Figure 5. 2.

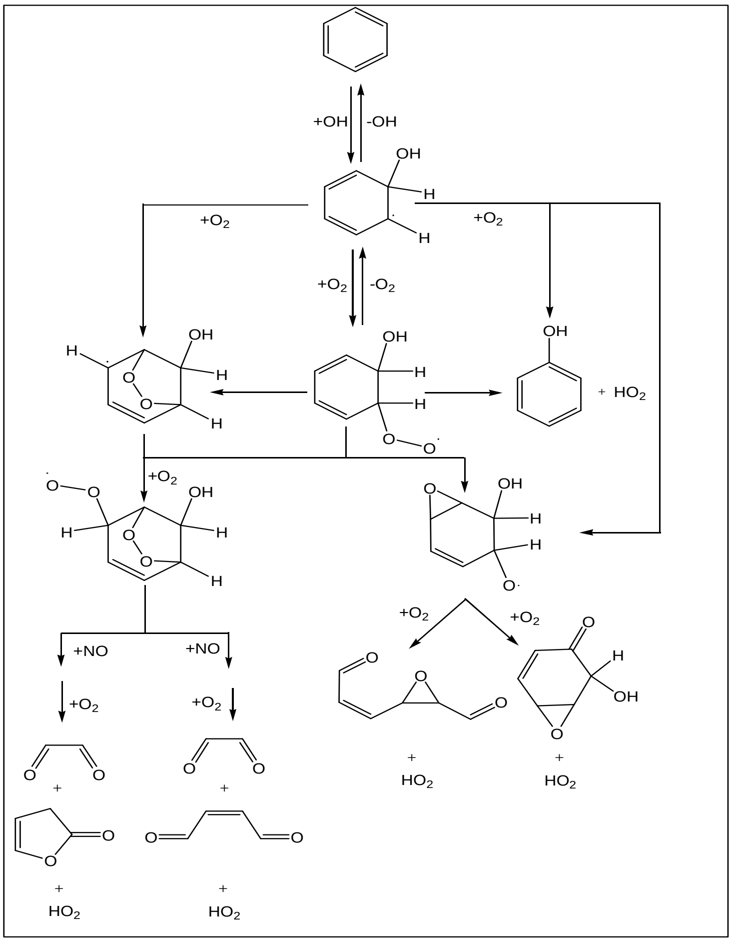

Figure 5. 2: The latest mechanism of the OH initiated oxidation of benzene leading to various products, reproduced from reference [8].

However, in case of alkylated aromatics, cresol yields for toluene and dimethyl phenol yields for p-xylene have been found to vary depending on the NOx concentration in various studies and hence are more uncertain [10]. Other ring cleavage products such as glyoxals and methyl glyoxals for benzene and toluene respectively, have been determined in various studies [1]. Recent work carried out by Volkamer et al. [11] at EUPHORE chamber has quantified the glyoxal yields from benzene, toluene and p-xylene oxidation to be 0.35, 0.39 and 0.40 respectively.

However due to the lack of knowledge about the intermediates of the ring cleavage process, the oxidation chemistry of the aromatic compounds is still very uncertain and no definite conclusions can be drawn about fate of the peroxy radicals and their subsequent degradation products. Hence, with the present knowledge of the OH initiated oxidation of aromatic compounds, the Master Chemical Mechanism (MCM) still over predicts the ozone and under predicts OH production in environmental simulation chamber studies [1]. Hence, the incomplete knowledge of the oxidation pathways of aromatics lead to uncertain predictions of ozone, Secondary Organic Aerosol (SOA) formation, and the oxidative capacity in urban air.

5.1.3 The search of missing channels in the oxidation mechanism

The uncertain predictions of ozone and SOA highlight towards the possibility that some of the fairly important channels in the initial steps of the OH initiated oxidation mechanisms of aromatic compounds could be still missing or are not properly accounted for. Recently, many new investigations have been performed with the aim of identifying these missing channels in OH initiated oxidation of aromatics. A possibility of one of such missing channel is the ipso addition of OH to the aromatic ring. Figure 5. 3 represents the possible ipso addition channel in case of toluene.

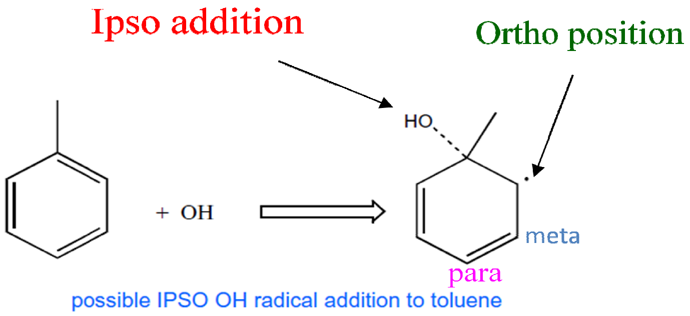

Figure 5. 3: A reaction scheme representing the possibility of OH addition at the ipso position on Toluene.

The ortho addition of OH onto the aromatic ring has been considered to be the dominant channel in the currently accepted MCM model whereas the ipso addition has been considered to be of less importance so far. The importance of such a channel has recently been discussed in the literature for methylated benzenes by Johnson et al. [5] with respect to combined DFT and statistical calculations for toluene, leading to 3% of ipso addition and from their recorded UV spectra of Ar-OH adducts, no evidence for the ipso channel was found. An ipso-to-methyl addition on p-cresol was found by Schuler et al. (2002) to occur with a probability of 12%, forming 4-hydroxy-4-methyl-2,5-cyclohexadiene-1- one as a final product in the liquid phase. Recently, Noda et al. [12] made use of chemical ionization mass spectrometry to demonstrate de-alkylation from the reaction of OH radicals with toluene and o-, m- and p-xylenes at (154 ± 4) Torr total pressure. De-alkylation yields of 5.4 ±1.2% of the toluene reaction (detected as phenol) and 4.5 ± 3.2%, 11.2 ± 3.8% and 4.3 ± 3.1% of the o-, m- and p-xylene reactions (detected as cresols) respectively, were found. These lastest results were found to be in contradiction with the new measurements of Aschmann et al. [13] leading to less than 1% of de-alkylation in the case of OH + *m*-xylene reaction. Moreover, tri-exponential OH decays have been measured by Koch et al. [6] in case of Mesitylene + OH reaction suggesting the possibility of ipso addition.

With the aim of investigating the ipso addition channel, OH initiated oxidation of hexamethyl benzene has been studied recently by Koch et al. [6] and Berndt and Boge et al [14]. The rate constant of HMB + OH reaction was measured by Berndt and Boge et al. [14] using relative rate method where they have measured the disappearance of HMB by its reaction with OH with respect to a known reference reaction of mesitylene + OH. Koch et al. [6] re-investigated the above rate constant in a more direct way by following the decay of OH in presence of HMB by using flash photolysis coupled to resonance fluorescence technique. Their measured rate constant is in excellent agreement with the one measured by Berndt and Boge et al.[14]. Even though HMB is unimportant in the atmosphere, it serves a very good model compound to study the OH ipso addition channel as all the six carbons on the aromatic ring in case of HMB are substituted by methyl groups. Hence, if at all, OH radical adds onto the HMB, it would definitely lead to the formation of HMB-OH (ipso) adduct as shown in Figure 5. 4.

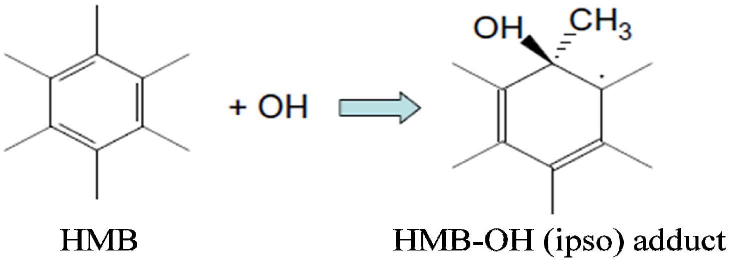

Figure 5. 4: A reaction scheme representing the formation of HMB-OH (ipso) adduct.

This provides the motivation for the present investigation to record the UV spectrum of HMB-OH (ipso) adduct and to measure and understand its decay kinetics using Laser photolysis coupled to time resolved UV spectroscopy and Discharge fast flow tube coupled to TOF-MS.

5.2 Results and Discussion

In order to understand the OH initiated oxidation of HMB, kinetic experiments were performed during the course of this thesis using two different experimental techniques. This chapter will discuss in detail the results obtained using the Laser photolysis coupled to time resolved UV spectrometry where the HMB-OH adduct spectrum and its decay kinetics were investigated. The reaction of OH + HMB was also investigated by J.C Loison, using discharge fast flow tube coupled to TOF-MS to understand the kinetics and the product distribution. I have participated in some of these experiments. These results will be discussed briefly in this chapter. From the knowledge of the possible primary products of OH initiated oxidation of HMB obtained from the TOF- MS studies, a global mechanism that could simulate the UV kinetic measurements has been proposed and the disagreement between the two studies is discussed at the end of this chapter.

5.2.1 Discharge fast flow tube coupled to TOF-MS

As mentioned in the introduction of this chapter, the OH initiated oxidation of aromatic compounds can proceed either by OH addition on to the aromatic ring or via H abstraction from one of the substituent groups. In case of HMB, this would either lead to the formation of Hexamethyl hydroxy cyclohexadienyl (HMB-OH) adduct or the H abstraction product, pentamethyl benzene (PMB). In order to investigate the branching ratio for these two channels, experiments were performed using discharge fast flow tube coupled to TOF-MS by J.C Loison. The experimental technique used has already been discussed in Chapter 2 section 2.2.

The product distributions from the reaction of OH (and OD) radicals with HMB were studied and to follow the progress of the reactions, the concentrations of products were monitored by their mass spectra. The adiabatic ionisation energies for different products were theoretically calculated using Electron propagator theory and the absolute ionisation cross sections were calculated from the model of Koizumi [15–18]. It is not desired to discuss these calculations in detail from the thesis point of view but more details on these calculations can be found in the reference [18*]. Typical VUV (10.54 eV) Single Photon Ionization

(SPI) mass spectra of HMB + OD, recorded at T = 344 K, 379 K and 433 K are presented in Figure 5. 5.

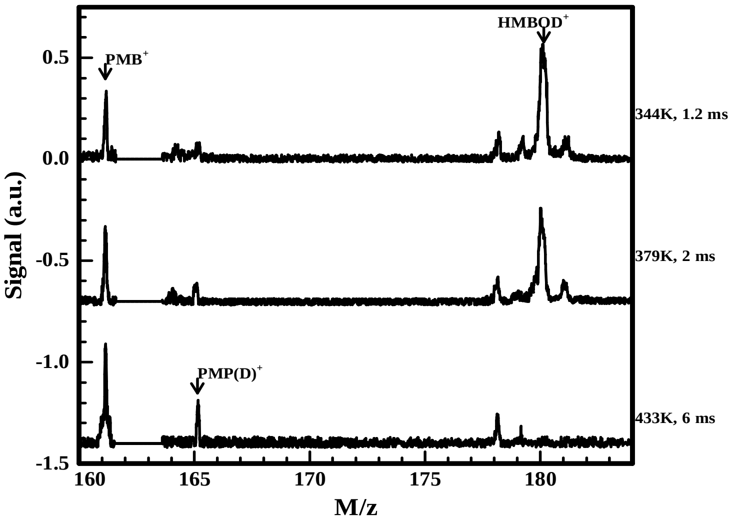

Figure 5. 5: Typical high sensitivity VUV (10.54 eV) Single Photon Ionization difference mass spectra of (HMB + OD) at 343 K (top), 379 K (middle) and 433 K (bottom). [OD] initial concentration was equal to 2 $\times 10^{12}$ molecules cm^{-3} and [HMB] concentration was equal to 3 $\times 10^{13}$ molecules cm^{-3}.

As can be seen from Figure 5. 5, the main observed peaks are PMB$^+$ and HMBOD$^+$. It is evident from the Figure 5. 5, that the HMB-OD is the main product at the lower temperatures. With the increase in the temperature the HMB-OD$^+$ peak intensity decreases and that of the PMB$^+$ increases. This was a clear indication of the existence of the equilibrium: HMB+OH $\leftrightarrow$ HMB-OH. Since at lower temperatures (330 K), the back dissociation was fairly slow, the amount of PMB$^+$ signal obtained was used as a measure for the direct H abstraction branching ratio (without equilibrium). The increase in the amount of PMB$^+$ ion peak with the increase in temperature was attributed to the increase in the back dissociation of HMB-OD to form HMB + OH and its subsequent reaction leading to H abstraction forming more PMB. The abstraction branching ratio was also evaluated by adding NO_2 to the reaction system, so as to form the HMB-OHNO$_2$ adduct and freeze the back dissociation. This allowed the estimation of direct H abstraction free of equilibrium in a better way. However, the estimation of addition of OH to HMB i.e. $k_{addition}$ was complicated by some secondary chemistry and hence $k_{addition}$ was calculated as the difference of the total rate constant (k_{total}) for the reaction of HMB+OH from reference [6], and the estimated $k_{abstraction}$. More details about the secondary chemistry can be found in reference [18*]. A product branching ratio of HMB-OH (90%) and PMB (10%) was estimated at 373 K. The only other detected product of HMB oxidation at short reaction time <10 ms was Pentamethyl phenol (PMP). This product was detected in small amounts (~4%) at high reaction temperatures of 433 K while at lower temperatures (≤373 K) the amount was negligible. Typical traces of the variations of HMB-OH and PMB concentrations recorded as a function of the distance "d" (or time) (from the extremity of the injector to the skimmer) for the (HMB + OH) reaction at 379 K are presented in Figure 5. 6. Each point on the graph represents one individual experiment at a fixed reaction time. The solid line corresponds to a fit of simulations using the mechanism listed in Table 5. 1.

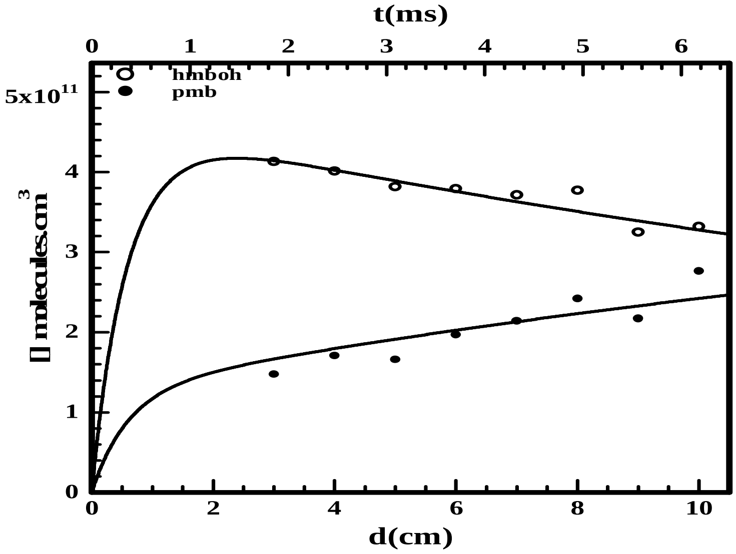

Figure 5. 6: Relative traces of the ion signal as a function of the distance d in the reactor for the (HMB + OD) reaction: (•): m/z = 180 (HMB-OD$^+$), (○): m/z = 161 (PMB$^+$). The OD initial concentration was equal to 1.6 ×10^{12} molecules cm^{-3} and the HMB concentration was equal to 3.0 ×10^{13} molecules cm^{-3}.

Reaction	Rate constant (cm^3 molecule^{-1} s^{-1})	Reference
HMB + OH → Products	$k_{total} = 1 \times 10^{-10}$	[6, 14]
HMB + OH → PMB + H_2O	$k_{abstraction} = 3.1 \times 10^{-11} \exp(-300/T)$	estimated
HMB + OH → HMB-OH	$k_{addition} = k_{total} - k_{abstraction}$	calculated
HMB-OH → HMB + OH	$k_{back} = 3.1 \times 10^{14} \exp(-10740/T)\ s^{-1}$	estimated
HMB-OH → PMP + CH_3	$K_{loss} = 2.4 \times 10^{12} \exp(-10200/T)\ s^{-1}$	estimated

**The mechanism presented here is a very simplified form of the actual complex mechanism that involves secondary reaction and other losses of HMB-OH and PMB (refer article [18*])*

Table 5. 1: Mechanism used to simulate the TOF-MS experiments

While the TOF-MS experiments were being conducted by J.C. Loison, new experiments were performed on the HMB+OH reaction system using Laser photolysis coupled to time resolved UV spectroscopy, in order to record the UV absorption spectrum of the HMB-OH adduct and also to measure its decay kinetics in presence and in absence of O_2.

5.2.2 Laser photolysis time resolved UV spectrometer

To record the UV-absorption spectrum of the HMB-OH adduct and to investigate its decay kinetics, experiments were performed using the laser flash photolysis technique. The HMB–OH adduct was formed by the reaction of OH (from the laser flash photolysis of H_2O_2 at 248 nm) with hexamethylbenzene and subsequently monitored by time-resolved UV absorption spectrometry in the wavelength range 265 to 340 nm. The details of the experimental technique, the calibration procedure to measure the OH concentration as well as the HMB concentration has already been discussed in chapter 2 section 2.2. Typical UV decay signals are shown in Figure 5. 7. Scattering of the laser pulse radiation produced a dead-time of 20 – 40 μs, indicating that the decay signals had to be extrapolated back to time zero (the time of the laser pulse) to determine the initial absorption.

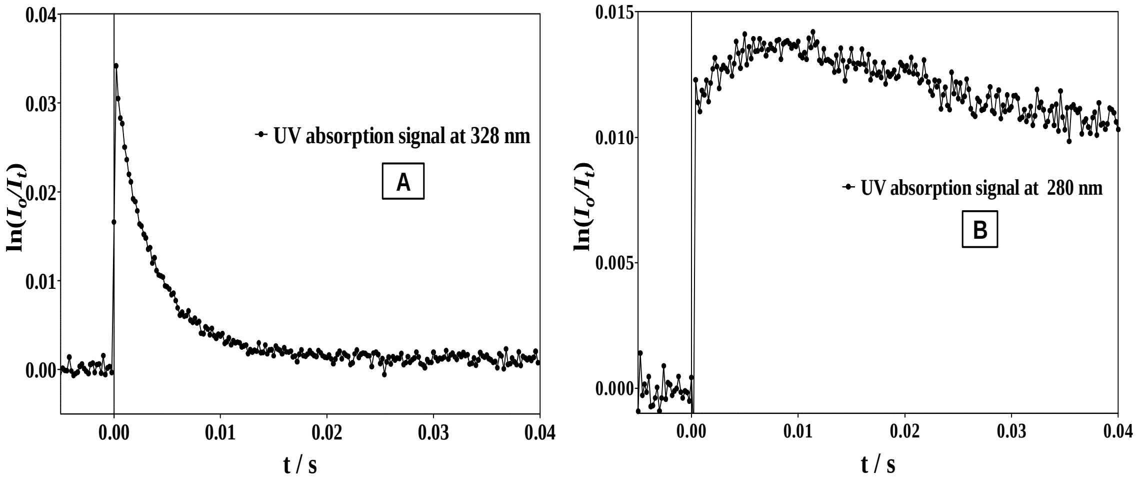

Figure 5. 7: Typical UV decay signals obtained using laser photolysis coupled to time resolved UV spectrometer at 328 nm and 280 nm in absence of O_2. $[H_2O_2] = (6 - 8) \times 10^{15}$ molecules cm^{-3} $[HMB] = (1.5 - 2) \times 10^{15}$ molecules cm^{-3}, $[OH]_0 = (2\text{-}3) \times 10^{15}$ molecules cm^{-3}, T = 373 ±4 K and Pressure = 760±10 Torr.

As it can be seen from Figure 5. 7A and Figure 5. 7B, that the shapes of the absorption signals at 328 nm and 280 nm are completely different. The absorption signals at wavelengths >300 nm showed fast decay profiles as can be seen from Figure 5. 7A, whereas those at wavelengths <300 nm had a formation profile of the absorbing species and its subsequent decay. While the formation of the 280 nm absorbing species happens on the same timescale as the decay of the 328 nm absoprbing species, its subsequent decay is much slower and not be observed at 328 nm, as can be seen from Figure 5. 7A and B. Clearly, these were absorptions due to two or more different absorbing species produced from the reaction of OH radicals with HMB. Since HMB-OH (major) and PMB (minor) were the two product detected in the TOF-MS measurements, it was likely that the two different absorption profiles observed in the UV measurements were due to HMB-OH and PMB absorptions separated in wavelength.

Hence, the initial absorbance values (immediately after the laser flash), has been attributed to the spectrum of the HMB-OH adduct as a function of wavelength and was obtained considering the branching ratios of HMB-OH to PMB of 90% to 10% respectively. The concentrations of HMB-OH and PMB were calculated accordingly from the initial OH concentration, determined using the $C_2H_5O_2$ calibration procedure. The obtained spectrum of HMB-OH adduct is as shown in Figure 5. 8.

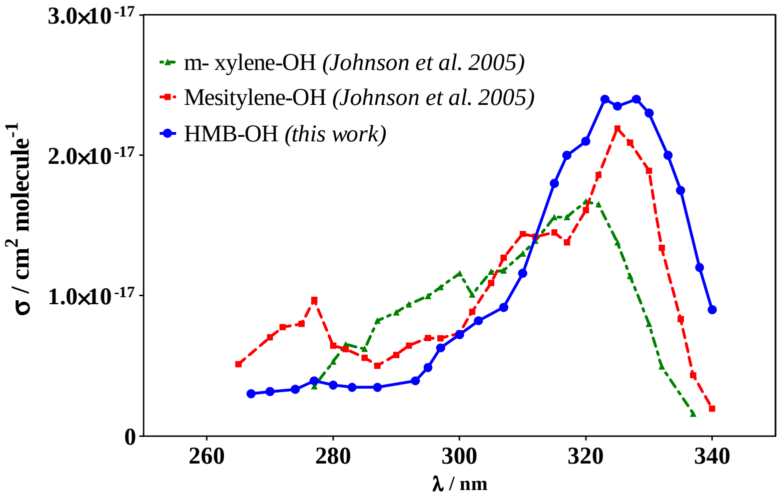

***Figure 5. 8: HMB-OH adduct spectrum obtained from the initial absorbance values as a function of wavelength. The above spectrum is already corrected for the absorption due to PMB** (PMB cross sections were assumed to be the same as that of benzyl radical [19] and concentration was calculated as the 10% of the total initial OH concentration)*

The measured HMB-OH adduct spectrum was found to have a close resemblance to the previously reported m-xylene-OH adduct and the mesitylene-OH adduct spectrum. Thgis is an evidence that the HMB-OH adduct is one of the product of the OH initiated oxidation of HMB.

5.2.2.1 HMB-OH adduct kinetics in absence of O_2

In order to confirm the branching ratios of the HMB-OH and PMB obtained from the TOF-MS studies, it was necessary to simulate the time resolved UV signals with the mechanism listed in Table 5. 1. The rate constants were calculated from Table 5. 1for the reaction temperature of 373 K at which the UV measurements were carried out. However, with these values it was not possible to simulate the UV decays. Figure 5. 9 shows a model simulation of the UV decay signal, simulated using the rate constants at 373 K, obtained from the TOF-MS studies.

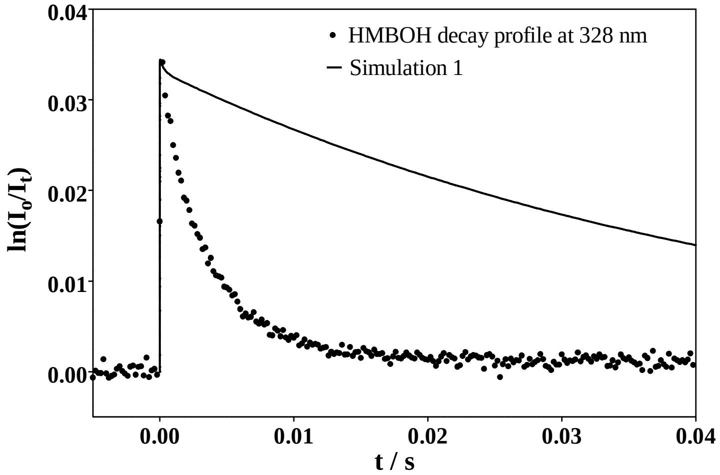

Figure 5. 9: Typical simulation of the HMB-OH adduct signal at 328 nm obtained using the mechanism listed in Table 5. 1

As can be seen from Figure 5. 9 the HMB-OH adduct signal decays very rapidly even at short reaction times <15 ms whereas according to the TOF-MS studies, the HMB-OH adduct is apparently more stable and decays relatively slowly under similar measurement time scales. The only significant loss of the HMB-OH adduct in TOF-MS measurements is through the back dissociation leading to HMB+OH and subsequent abstraction reaction, ie. a loss of the adduct through leaking out of the equilibrium into the abstraction path. However, the value of back dissociation estimated at 373 K through TOF-MS studies was too small to explain the loss of HMB-OH observed in UV measurements.

Since the product branching ratios estimated in the TOF-MS studies, failed to explain the fast decays of HMB-OH, new branching ratios of 70% and 30% for PMB and HMB-OH respectively, were assumed as in a trial an error method, maintaining the total rate constant of HMB+OH reaction to $1.1\text{x}10^{-10}$ cm^3 $\text{molecule}^{-1}\text{s}^{-1}$ as measured by Koch et al. and Berndt and Boge et al. [6, 14]. The back dissociation of the HMB-OH adduct was estimated by simulating the decays of HMB-OH adduct at higher wavelengths at around 328 nm. The proposed mechanism is presented in Table 5. 2. With this mechansim it was possible to simulate all the time resolved UV decay profiles from 265 to 340 nm. The two typical of those simulated profiles are shown in Figure 5. 10 and Figure 5. 11

Reaction	**Rate constant**	**Reference**
$H_2O_2 + h\upsilon \rightarrow 2OH$	$\Phi_{248} = 2$	[20, 21]
$OH + H_2O_2 \rightarrow HO_2 + H_2O$	1.7×10^{-12} cm^3 molecule^{-1} s^{-1}	[22]
$HO_2 + HO_2 \rightarrow H_2O_2 + O_2$	1.65×10^{-12} cm^3 molecule^{-1} s^{-1}	[22]
$\text{HMB} + OH \rightarrow \text{PMB} + H_2O$	7×10^{-11} cm^3 molecule^{-1} s^{-1}	estimated
HMB + OH → HMB-OH	3×10^{-11} cm^3 molecule^{-1} s^{-1}	estimated
HMB-OH → HMB + OH	(350 ± 20) s^{-1}	estimated
$\text{HMB-OH} + HO_2 \rightarrow \text{PRODUCT2}$	1.8×10^{-10} cm^3 molecule^{-1} s^{-1}	[23]*
PMB + PMB → BIPMB	$(3 \pm 0.3) \times 10^{-13}$ cm^3 molecule^{-1} s^{-1}	estimated

**The rate constant for HMB-OH +HO_2 has been assumed to be the same as for Toluene-OH +HO_2*

Table 5. 2: Mechanism used to simulate the time resolved UV decay profiles of HMB-OH

As can be seen from Figure 5. 10, the HMB-OH experimental decays were nicely simulated with back dissociation rate constant of 350 s^{-1}. It was observed through simulations that the formation profile observed at around 280 nm could be explained if the back dissociation of HMB-OH leading to HMB + OH were undergoing an H abstraction, leading to an increase in PMB formation. This would lead to an enhanced loss of HMB-OH out of equilibrium.

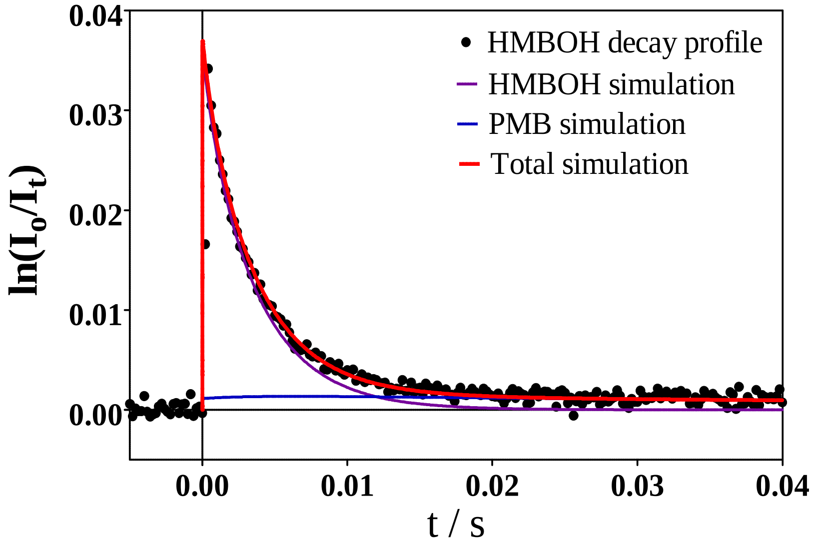

Figure 5. 10: UV decay profiles at 328 nm simulated using the mechanism listed in Table 5. 2. (•) represents experimental data and (—) represents simulation at 373 K.

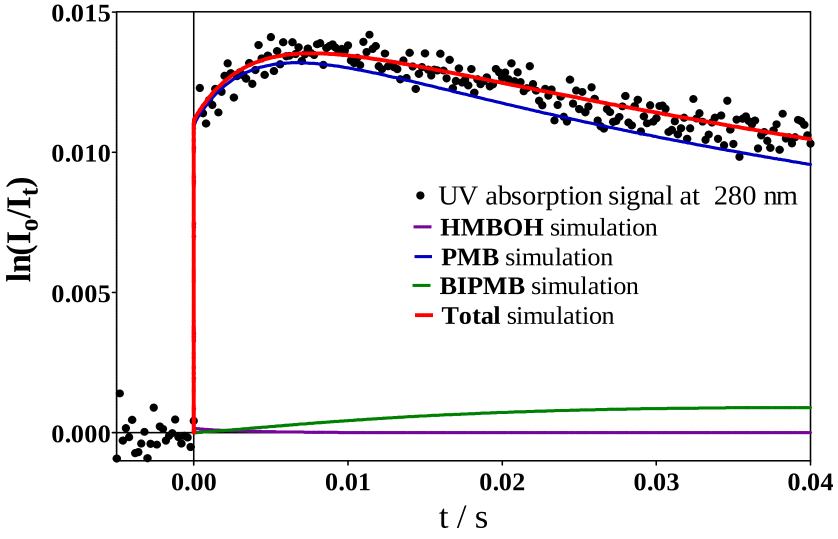

Figure 5. 11: UV decay profiles at 280 nm simulated using the mechanism listed in Table 5. 2. (•) represents experimental data and (—) represents simulation at 373 K.

With such an assumption, it was possible to simulate both the signal at 328 nm as well as the initial rise at 280 nm. The subsequent decay at 280 nm was attributed to the loss of PMB by self recombination reaction, either leading to Pentamethyl bi-benzyl (BIPMB) or some other unknown product. A second order rate constant of 3 x 10^{-13} cm^3 $molecule^{-1}s^{-1}$ was needed in order to simulate the 280 nm decay profiles. If we compare the literature values for the rate constant for benzyl radical self reaction, the estimated range of values available in the NIST database vary from 4 x 10^{-12} to 3 x 10^{-11} cm^3 $molecule^{-1}s^{-1}$ [24], [25]. Considering the steric hindrance for such a self recombination reaction of PMB, the estimated value of 3 x 10^{-13} cm^3 $molecule^{-1}s^{-1}$ is not unimaginable. It is important to note that in case of TOF-MS studies, the initial OH concentration employed in these measurements was 2 x 10^{12} molecules cm^{-3} and hence under such low radical concentrations even if the PMB self recombination reaction occurred, it would proceed at a much longer reaction time outside the measurement time window of the TOF-MS studies and would not have appeared in the mass spectra. Since it was possible to simulate all the time resolved UV decay profiles as a function of wavelength with one global mechanism, just by varying the absorption cross section of HMB-OH and PMB, it allowed us to obtain the UV spectrum of the HMB-OH adduct and PMB through simulation. The new HMB-OH and PMB spectrum are shown in and the cross section values are shown in Figure 5.12 and the cross sction values are listed in Table 5.3.

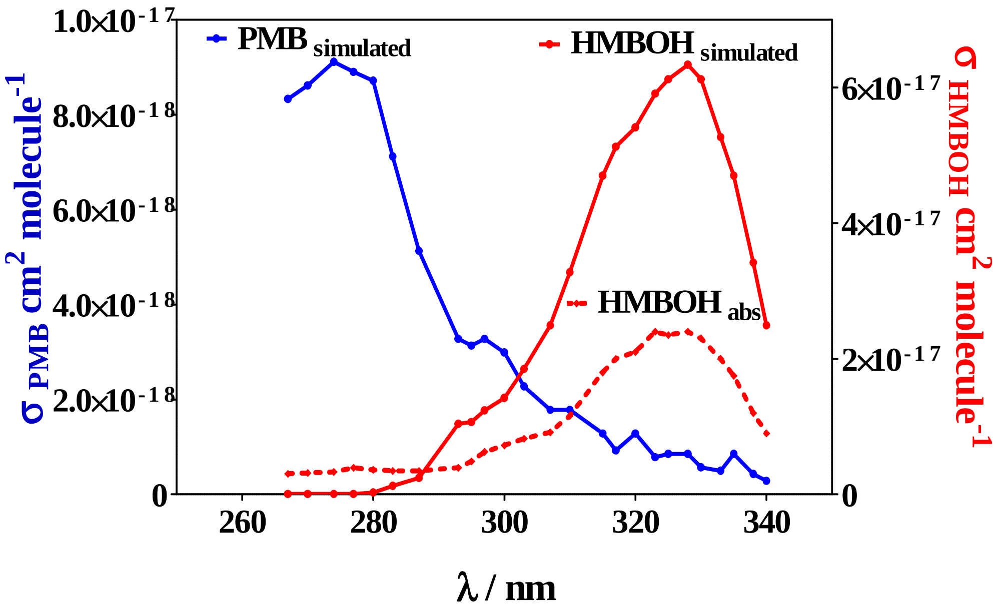

Figure 5. 12: HMB-OH $_{simulated}$ and PMB $_{simulated}$ are the spectra obtained from the simulations of the UV decay signals using the mechanism listed inTable 5. 2. HMB-OH $_{abs}$ represents the HMB-OH spectrum obtained using the initial absorbance as shown in Figure 5. 8.

λ /nm	**σ (HMB-OH)/ cm^2 $molecule^{-1}$**	**λ /nm**	**σ (HMB-OH)/ cm^2 $molecule^{-1}$**
267	7×10^{-20}	310	3.28×10^{-17}
270	7×10^{-20}	315	4.7×10^{-17}
274	7×10^{-20}	317	5.13×10^{-17}
277	7×10^{-20}	320	5.41×10^{-17}
280	2.85×10^{-19}	323	5.91×10^{-17}
283	1.28×10^{-18}	325	6.13×10^{-17}
287	2.42×10^{-18}	328	6.34×10^{-17}
293	1.04×10^{-17}	330	6.12×10^{-17}
295	1.07×10^{-17}	333	5.27×10^{-17}
297	1.24×10^{-17}	335	4.7×10^{-17}
300	1.42×10^{-17}	338	3.42×10^{-17}
303	1.85×10^{-17}	340	2.49×10^{-17}
307	1.29×10^{-17}		

Table 5. 3: Cross section values for HMB-OH adduct obtained using the mechanism listed in Table 5. 2.

If we compare the HMB-OH spectrum obtained from the initial absorbance value (Figure 5. 8) with one obtained from simulations (

Figure 5. 12), we see that the form of the spectrum remains approximately the same with a strong absorption at around 328 nm, except that the estimated cross section values are ~ 3 times higher in the later case, as the initial concentration of the HMB-OH adduct in this model is lower by the same amount due to the changed branching ratio between addition and abstraction reaction. The form of the HMB-OH adduct spectrum obtained both from the simulations and by considering the initial absorption values, agree very well with the reported spectra of m-xylene-OH and mesitylne-OH.

A comparison between the PMB spectrum obtained from simulations and the one reported in the literature [19] for benzyl radicals is shown in Figure 5. 13. The cross section values estimated for PMB are very similar to those of benzyl radicals except that we do not observe the sharp absorption peak at around 306 nm. No definite explanation for this disagreement can be given at this stage of the work. It could be that the spectrum of PMB in reality is completely different than that of benzyl radical. Another possibility is that the product that we think as PMB is not a benzyl type radical but some other unknown product. However, the problem with this kind of an assumption is that no product other than HMB-OH and PMB were detected in the TOF-MS measurements. Moreover, till date there is no reported spectrum of PMB in the literature to the best of our knowledge and hence the presence of PMB in the UV measurements cannot be confirmed.

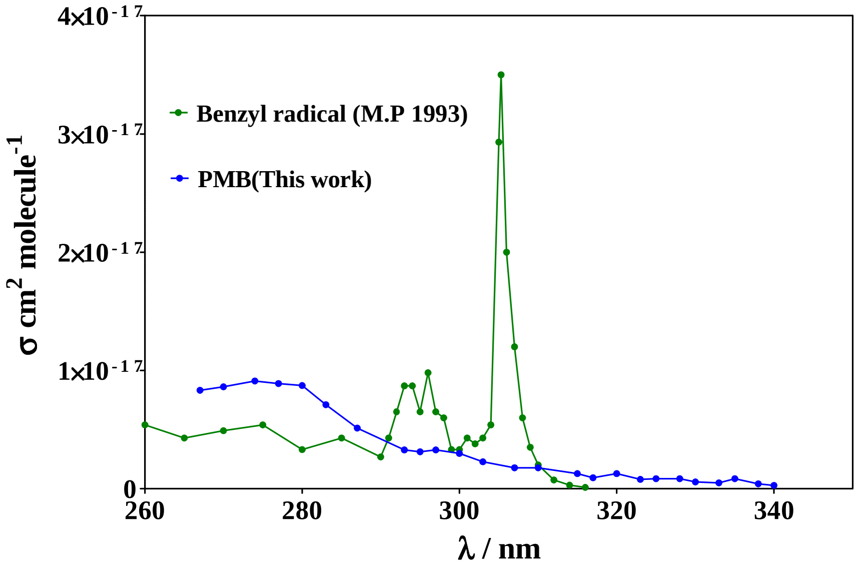

Figure 5. 13: A comparison between the Pentamethyl benzyl radical (PMB) spectrum obtained from simulations with that of Benzyl radical spectrum from reference [19].

It is important to note that the value of the cross sections estimated from the UV measurement are strongly dependent on the branching ratios chosen for the $k_{abstraction}$ and $k_{addition}$ channels and hence any uncertainty in these values could render a big error in the estimated cross section of both HMB-OH and PMB. Since the decay kinetics of HMB-OH depends on the value of the product of the equilibrium constant of HMB + OH reaction ($K_{equilibrium}$) and the rate constant for the H abstraction channel ($k_{abstraction}$), it is possible to find many different combinations of values that allow to simulate the observed decay profiles. Hence the uncertainty here is not the experimental uncertainty (<±10% due to the experimental noise) but rather the uncertainty of the chosen mechanism. In order to validate the mechanism, more experiments would be necessary especially at different temperatures so that the equilibrium constant could be determined and then the abstraction channel could be extracted in a more reliable way. However, high concentration of HMB was a perquisite condition of the UV experiments in order to have HMB + OH as the dominant reaction compared to H_2O_2 + OH, for which it was necessary to heat HMB to 373 K and hence the UV experiments were carried out at 373 K. The lower reaction temperatures were not desired so as to avoid condensation of HMB in the reactor. Temperatures higher than 380 K were not possible with the existing configuration of the experimental setup and hence it was not possible to validate the back dissociation and branching ratios.

5.2.2.2 HMB-OH adduct kinetics in presence of O_2

In order to measure the decay kinetics of HMB-OH adduct in presence of O_2, experiments were performed by adding O_2 to the HMB+OH system. HMB-OH adduct decays were recorded as a function of O_2 concentration at 328 nm where the absorption cross section of HMB-OH adduct has a maximum. The recorded decay profiles with and without O_2 are shown in Figure 5. 14.

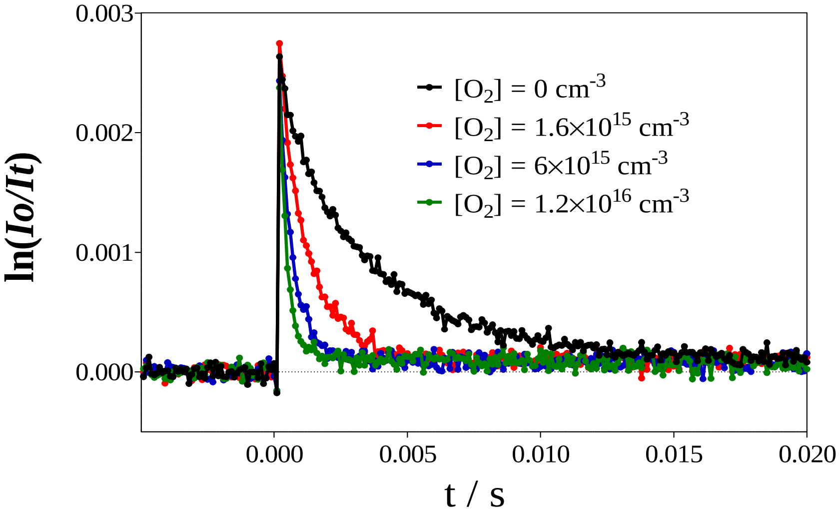

Figure 5. 14: UV decay signal of HMB-OH adduct recorded at 328 nm at 373K without and with different O_2. (Y - axis has been devided by the photolysis laser energy (12-15) mJ cm^{-2} in order to account for the change in the initial OH concentration)

According to the previous reports on OH initiated oxidation of benzene and toluene, Bohn et al. [7] and Johnson et al. [2] have observed an increase in the Ar-OH adduct UV absorption signal upon addition of the aromatics. The increase of the signal was linear with the concentration of the aromatic hydrocarbon. They attributed this phenomenon to an additional OH production from the photosensitized decomposition of H_2O_2 after collision with excited aromatic hydrocarbon. It has also been reported in the above two articles that the additional OH-production could be suppressed by addition of O_2. In the case of HMB we could not vary the HMB concentration in order to verify if such process also takes place for HMB, but as we did not observe any decrease in the adduct absorption signal upon addition of O_2 we can assume that such additional OH production does not take place in this system. As can be seen from Figure 5. 14 the absorption signals in presence and in absence of O_2 have similar values of initial absorbance at time zero, hence, it was not necessary to re-measure the entire spectrum in presence of O_2. It can be seen clearly from Figure 5. 15 that the HMB-OH adduct decay kinetics become faster with increase in the O_2 concentration. With the present understanding of the aromatic-OH adduct reactivity in presence of O_2, the Ar-OH adduct is known to react either via addition and formation of HMB-OH peroxy radical (HMB-OH-O_2) or it could directly form products [26]. Figure 5. 15 shows a typical simulation of the HMB-OH adduct signal at 328 nm in presence of O_2, simulated using the mechanism listed in Table 5. 4.

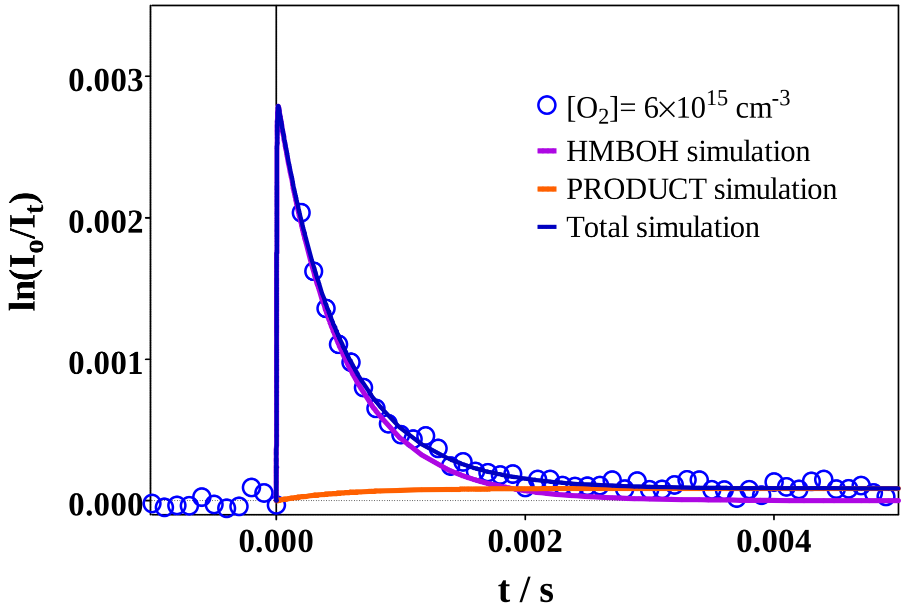

Figure 5. 15: Typical HMB-OH adduct decay signal recorded at 328 nm and 373K in presence $[O_2] = 6 \times 10^{15}$ molecules cm^{-3}, simulated using the mechanism listed in Table 5. 4.

Reaction	Rate constant at 373 K and 760 Torr	References
$H_2O_2 + h\upsilon \rightarrow 2OH$	$\Phi_{248} = 2$	[20, 21]
$OH + H_2O_2 \rightarrow HO_2 + H_2O$	1.7×10^{-12} cm^3 molecule^{-1} s^{-1}	[22]
HMB + OH → HMB-OH	3×10^{-11} cm^3 molecule^{-1} s^{-1}	estimated
HMB-OH → HMB + OH	350 s^{-1}	estimated
HMB + OH → PMB +H_2O	7×10^{-11} cm^3 molecule^{-1} s^{-1}	estimated
HMB-OH + O_2 → PRODUCT	$(2.9\pm0.4) \times 10^{-13}$ cm^3 molecule^{-1} s^{-1}	estimated
PMB + O_2 → PRODUCT1	1.4×10^{-12} cm^3 molecule^{-1} s^{-1}	[27]*
HMB-OH + HO_2 → PRODUCT2	1.8×10^{-10} cm^3 molecule^{-1} s^{-1}	[23]
$HO_2 + HO_2 \rightarrow H_2O_2 + O_2$	1.65×10^{-12} cm^3 molecule^{-1} s^{-1}	[22]

* *The rate constant k_{PMB+O2} has been assumed to be the same as for $k_{Bezyl+O2}$ because firstly, no rate data for this reaction is available in the literature at the moment and secondly, not a great change in the rate is expected as the reaction occurs at the radical site located at the substituted carbon.*

Table 5. 4: Reaction mechanism used for the analysis of HMB-OH decays at 328 nm in presence of O_2

It was observed through simulations that the HMB-OH adduct decays rapidly after the addition of small amounts of O_2 leading to some product formation which also absorbs as can be seen as a residual absorption in Figure 5. 15. At this stage of the work, the residual absorption at 328 nm cannot be assigned to one particular species as not much is known about the product yields of the OH initiated oxidation of HMB. In a recent investigation on the HO_2 production from a series of methylated aromatic-OH adducts in presence of O_2, Nehr et al. [28] have observed HO_2 production from the reaction of HMB-OH adduct with O_2. In a similar investigation of the HMB-OH adduct decomposition using TOF-MS, Berndt and Boge et al. [14] have observed the m/z peaks corresponding to the hexamethyl-2-4-cyclohexadienone which they have attributed to the loss of H atom from the HMB-OH adduct leading to the ketonic product. The possibility of the H atom loss from HMB-OH adduct is not unimaginable and moreover, it also explains the prompt HO_2 yields from the OH initiated oxidation of HMB in presence of O_2 as observed by Nehr et al. [28]. Hence it is possible that such a product could account for the observed residual absorption, however, no definite conclusions can be drawn at this stage.

Another possiblity is that the reaction of HMB-OH + O_2 leads to the formation of HMB-OH-O_2. However, it is most unlikely that the observed product under our experimental condition could be HMB-OH-O_2, firstly because, most of the peroxy radicals are known to absorb at shorter wavelengths of ≤ 280 nm [29] and the observed absorption of the PRODUCT at 328 nm ($\sigma = (1\pm0.2) \times 10^{-18}$ cm^2 $molecule^{-1}$) is not expected for peroxy radicals. Secondly, the aromatic-OH-O_2 radicals exist an equilibrium reaction forming HMB-OH + O_2 as reported by Bohn et al. [7, 23]. If this was the case for the HMB-OH adduct, than the residual absorption of the HMB-OH adduct decay signal at 328 nm would represent the equilibrium concentration of HMB-OH adduct and one would expect a significant change in the residual signal with a change in the O_2 concentration. However, in case of the experimentally measured HMB-OH decay profiles in presence of O_2, no change in the residual absorption with changing O_2 concentration has been observed (see Figure 5. 16.)

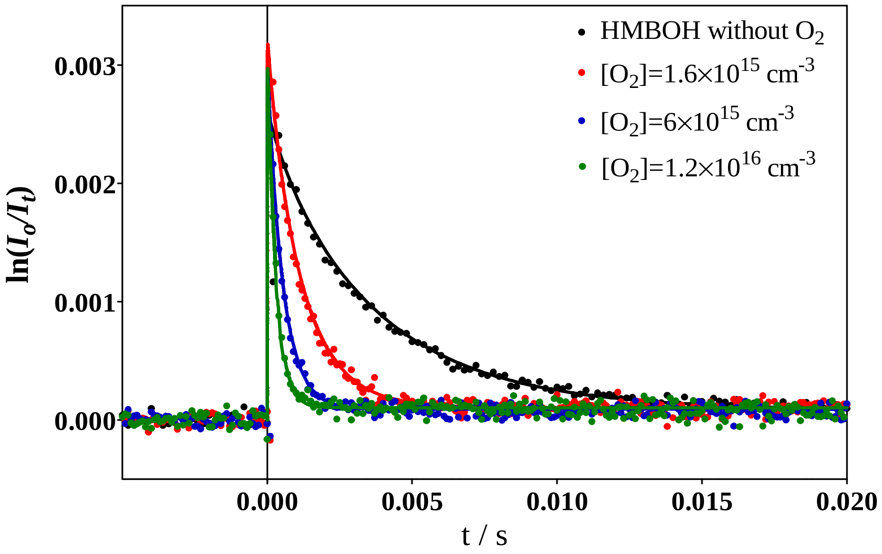

Figure 5. 16: HMB-OH adduct decay with and without O_2, simulated using the mechanism listed in Table 5. 4. [HMB-OH] = (2-3) $\times10^{13}$ cm^{-3} and $[O_2]$ = (0.16, 0.6, 1.2) $\times10^{16}$ cm^{-3} for the green, red and blue curves respectively.

The HMB-OH adduct decay profiles at 328 nm at different O_2 concentrations, simulated using the mechanism listed in Table 5. 4, are presented in Figure 5. 16. The second order rate constant $k_{HMB-OH+O2}$, obtained from the simulations is equal to (2.9±0.4) × 10^{-13} cm^3 moleculce $^{-1}s^{-1}$, a value found to be in good agreement (within th errors bars) with the value of 1.8 x 10^{-13} cm^3 $molecule^{-1}$ s^{-1} measured by Koch et al. [6] Since it was possible to simulate time resolved UV decay profiles of HMB-OH both with and without O_2 with the branching ratios and the mechanism proposed in Table 5. 4, with good agreements on the rate constants for the HMB-OH+O_2 reaction, we can conclude that the proposed mechanism is self consistent and explains all the UV measurements. However, this mechasim remains in complete disagreement with the one proposed by loison et al. [18*] and Koch et al. [6] for the HMB-OH system without O_2

5.2.2.3 The possible cause of the disagreement between the TOF-MS and UV measurements

If one assumes that the branching ratios obtained from the UV measurements were the good ones, than the obvious question would be; what could be the possible cause of the complete disagreement with TOF-MS measurements of [18*] and that of Koch et al. [6]. A few of the possible causes are discussed in this section.

1) It is important to note that in the TOF-MS experiments the concentration of HMB was measured relative to a known propene concentration assuming that the ionisation cross section for the HMB at 10.54 eV is same as that of benzene, toluene and xylene (30± 5) x 10^{-18} cm^{-2} [18*]. Also, the ionisation cross section for HMB-OH and PMB, to our knowledge, does not exist in the literature. The ionisation cross sections were calculated from the model of Koizumi which works well for radicals such as phenyl, formy and vinyl etc. [18*]. If these cross sections were ~7 times different than those assumed for the reactants and the products, than this would explain the observed disagreement on the PMB branching ratio in the TOF-MS and UV measurements (TOF-MS: 10% and UV measurements: 70%). However, such a big error on the cross sections might be difficult to imagine and also it wouldn’t explain why Koch et al. have observed similar results.

2) The major difference between the two studies was that in the UV measurements the 248 nm photolysis of H_2O_2 was used as the OH precursor whereas in case of TOF-MS studies, the OH radicals were produced by the reaction of $F+H_2O$. The use of H_2O_2 precursor leads to the production of HO_2 radicals by the reaction of OH + H_2O_2. However, in presence of large excess of HMB, the competing reaction to form HO_2 was negligible (~3.3%) and hence even with a high rate constant, as high as 1.8×10^{-10} cm^3 $molecule^{-1}$ s^{-1} for the reaction of HMB-OH + HO_2 (value taken similar to Toluene-OH + HO_2 from reference [23]), it could never explain the experimentally observed fast decays of HMB-OH adduct (~313 s^{-1}).

3) Another possible complication of the reaction system could arise from the recently discovered formation of HO_2 radical from the reaction of aromatic hydrocarbons, excited at 248 nm in the presence of O_2. Jain et al. [30–32] have observed the HO_2 radical formation from the 248 nm excitation of a series of methylated aromatic compounds in presence of O_2. They have attributed it to a 2 photon excitation of aromatic hydrocarbons and its subsequent chemistry with O_2 and have given an empirical equation for an estimation of such HO_2 formation. It has also been speculated from the same studies that it is not only HO_2 that is produced from the two photon absorption process by the aromatics but also some other unknown radical species (X) as a co-product in at least equal amounts as HO_2 (for more details refer [30]). Even though they did not investigate HMB, such a production of unknown species (X) could also be expected from HMB. Since the UV experiments were carried out in absence of O_2, the direct production of HO_2 without a source of O_2 can be ruled out. However, the unknown species (X) itself could be present, even in absence of O_2. In order to estimate the impact of (X), the amount of initial (X) radicals that could have been produced under our experimental conditions were calculated from the equation in reference [30] assuming that the amount of (X) produced is equal to the amount of HO_2.

$$[HO_2] = [X] = 2 \times 10^{-6} \times E^2 \times [HMB] \qquad (E1)$$

where E is the photolysis energy in mJ cm^{-2}.

Typical experimental conditions used in this work ([HMB] = 2×10^{15} molecules cm^{-3}, E = 15 mJ cm^{-2}) leads to formation of (X) = 1.8×10^{12} molecules

cm^{-3}. The above equation is valid for aromatic compounds with absorption cross section in the range of (1 - 4) x 10^{-19} cm^2 $molecule^{-1}$at 248 nm, which was the case for the aromatic compounds studied in reference [30]. However, in case of HMB, there are two references which provide completely different cross sections. In the NIST database, the UV absorption cross section for HMB at 248 nm is reported to be 2.4 x 10^{-19} cm^2 $molecule^{-1}$at 248 nm [33]. The amount of (X) was calculated using the above cross section and this yields concentration of (X) = 6.7×10^{11} molecules cm^{-3} as explained above. The UV decay signal at 328 nm was re-simulated using the mechanism proposed by [18*] with an added reaction of X + HMB-OH, assuming a fast rate constant of 1.8 x 10^{-10} cm^3 $molecule^{-1}$ s^{-1}. The new simulation is as shown in Figure 5. 17.

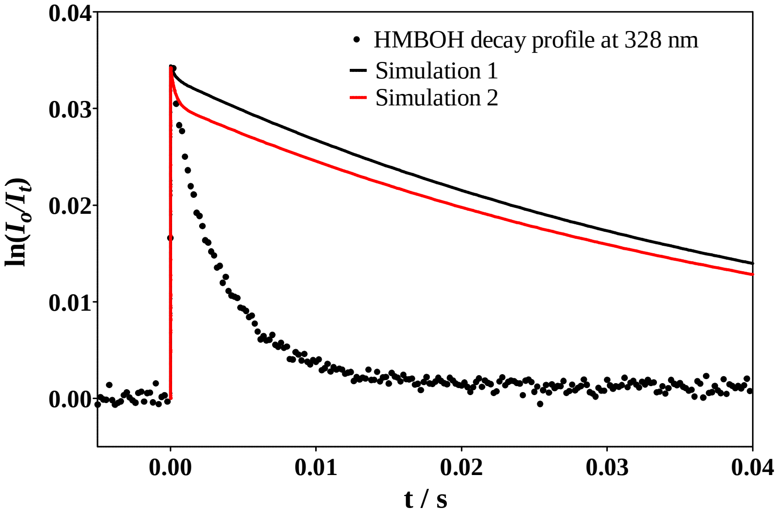

Figure 5. 17: Simulations of the HMB-OH adduct signal at 328 nm with 1) using the mechanism listed in Table 5. 1 alone, represented by (—) and 2) including the reaction of HMB-OH + X to the mechanism listed in Table 5. 1, presented by (—).

It can be seen from Figure 5. 17 that the concentration of (X) calculated from the above equation were not sufficient to explain the observed fast decays. This is not surprising, as the concentration of (X) calculated this way is much lower than the initial OH concentration (2-3 x 10^{13} molecules cm^{-3}) and hence only around 10% of the adduct decays rapidly. Since the UV decays at 328 nm were exponential, we would need concentrations of (X) to be at least a few times higher than the concentration of HMB-OH in order to observe the loss of HMB-OH under pseudo first order conditions. This possibility cannot be ignored as in another work by Bolovinos et al. [34], the gas phase spectrum of HMB is also provided and according to this article the cross section of HMB at 248 nm is 2.9 x 10^{-18} cm^2 $molecule^{-1}$at 248 nm, a value 10 times higher than the one reported by NIST. If such a high cross section, leads to for example, 4 x 10^{13} cm^{-3} of “X” than with a rate constant of 7 x 10^{-12} cm^3 $molecule^{-1}$ s^{-1}, a pseudo first order rate constant of ~313 s^{-1} can be obtained as needed to explain the decays of HMB-OH at 328 nm. However, this is just an example of what concentrations of (X) and the rate constant that will be needed to fit the UV decays and many more such combinations could be used to explain the decays of HMB-OH. Such a possibilty would explain why the UV decays of HMB-OH were faster than those expected from the TOF-MS studies (see Figure 5. 17).

4) Since the UV experiments were carried out at 373 K, it might be possible that a small perecentage of H_2O_2 might decompose on to the reactor walls and this might lead to the generation of O_2 in the system. If such a decomposition of H_2O_2 generates ~ 1x 10^{15} molecules cm^3 of O_2, this would be sufficient to explain the fast decay of HMB-OH (~300 s^{-1}). Such a possibility cannot be ignored. In addition to this, if the HMB-OH adduct would react with hexamethylbenzene with a rate constant of ~1.5 x 10^{-13} $cm^3molecule^{-1}s^{-1}$, then this would also explain the fast decays of HMB-OH in absence of O_2. Hence the possibilities are many but in order to identify the true cause of the disagreement, more experiments under different initial radical concentration are needed.

5.2.2.4 *Implications of the possible HMB photolysis to the HMB-OH decay kinetics in presence of O_2.*

As explained earlier, if the 248 nm cross section of HMB reported by NIST is the good one, than this leads to the production of $HO_2 = 6.7\times10^{11}$ molecules cm^{-3}. To account for this, the HMB-OH adduct decay at 328 nm in presence of different concentration of O_2 were re-simulated by using the mechanism listed in Table 5. 4. It was observed that, the addition of an initial HO_2 concentration (i.e. from photolysis) leads to a small decrease in the HMB-OH initial concentration (<10%) due to the fast reaction of HMB-OH + HO_2. However, the increase in the concentration of HO_2 due to photolysis is so small that it does not contribute significantly to cause a change the observed decay kinetic of HMB-OH in presence of O_2. Taking into account the 10 times higher absorption cross section of HMB as reported by Bolovinos et al. [34] and assuming that this generates say suppose 10 times more HO_2, than the contribution of HO_2 to the loss of HMB-OH adduct will be ~10 times more. This would mean that the rate constant of HMB-OH +O_2 would be much slower (may be10 time slower), than the previously estimated value of 2.9 x 10^{-13} $cm^3molecule^{-1}s^{-1}$. This would mean a complete disagreement with the reported rate constant of 1.8 x 10^{-13} $cm^3molecule^{-1}s^{-1}$ of Koch et al. However, instead of performing simulations using the mechanism listed in Table 5.4, if we fit the decays of HMB-OH adduct in presence of different O_2 concentrations, with an exponential fit and plot the decay rate obtained from the fits vs the O_2 concentration, than we obtain a straight line with an intercept of 578± 30 and a slope of (2.3±0.5) x 10^{-13} as shown in Figure 5. 18. This means that the increase in the decay rate of HMB-OH adduct can be explained very well with the increasing O_2 concentration and the obtained rate constant $k_{HMB\text{-}OH+O2}$ = (2.3±0.5) x 10^{-13} $cm^3molecule^{-1}s^{-1}$ is in good agreement with the one measured by Koch et al.

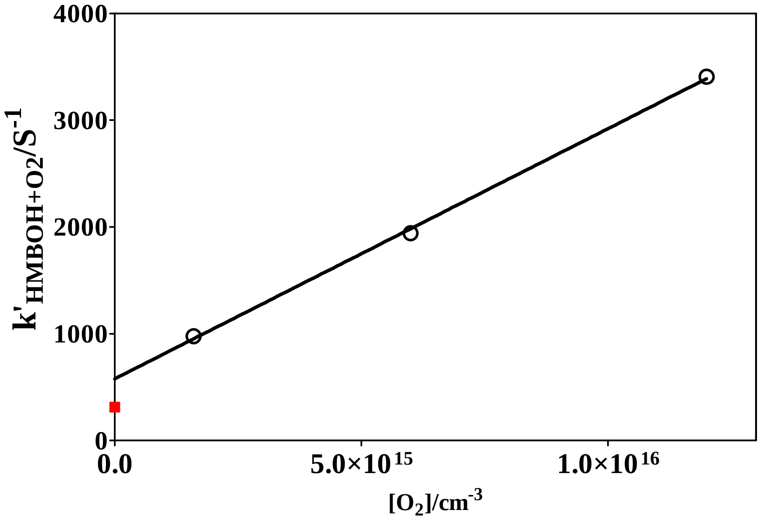

Figure 5. 18: A plot of k'$_{HMB\text{-}OH+O2}$ (pseudo first order decay rate obtained from the exponential fits) as a function of O_2. (■) repsenents the HMB-OH decay rate without O_2 and (○) represents the HMB-OH decay rate at different O_2 concentrations.

The high value of intercept (578 s^{-1}) obtained represents the expected HMB-OH adduct decay in absence of O_2, which is ~ 2 times higher than the one experimentally measured (~300 s^{-1}) at 328 nm without O_2. The formation of reactive species (HO_2 or X) from photolysis of HMB could be the reason behind the observed high intercept value. In order to understand this, it was important to perform experiments under different radical concentrations by changing the photolysis laser energy or by changing the HMB concentration. However, the excimer laser employed in these experiments did not allow laser energies to be varied over a large range. The maximum photolysis energy obtained was ≤15 mJ cm^{-2} and hence it was not possible to have higher radical concentrations. Also, as already explained, the present configuration of the experimental setup did not allow temperatures higher than 380 K and hence it was not possible to increase the HMB concentrations either. Hence no conclusion can be drawn about the photolysis of HMB and the subsequent chemistry of the photolysis products with HMB-OH at this stage. Nonetheless, as long as the OH decays are exponential under different O_2 concentrations, the increase in the decay rate of HMB-OH with increasing O_2 can be attributed to the reaction of HMB-OH+O_2 and the slope of the linear regression = 2.3×10^{-13} (in Fig. 5.18) which corresponds to the the rate constant $k_{HMB\text{-}OH+O2}$, is in good agreement with the one measured by Koch et al.

5.3 Conclusion

The OH initiated oxidation of HMB has been investigated using Discharge fast flow tube coupled to TOF-MS. In these measurements the HMB-OH was identified as the major oxidation product (90%) whereas PMB was detected in low amount (~10%) at 373 K. The temperature dependent studies were also carried out during the course of this study which allowed the back dissociation of the HMB-OH adduct to be estimated.

The OH initiated oxidation of HMB was also studied using laser photolysis coupled to time resolved UV spectroscopy. The HMB-OH adduct was produced by the reaction of OH radicals (produced from the 248 nm photolysis of H_2O_2) with HMB. The HMB-OH adduct spectrum was recorded by following the time resolved decay kinetics of HMB-OH adduct as a function of wavelength. The observed decays kinetics of the HMB-OH adduct could not be reproduced with a model using the branching ratios and the rate constants such as obtained in the discharge fast flow tube TOF-MS studies. In order to explain the disagreement, the possible complications of the UV measurements due to the 2 photon excitation of aromatics at 248 nm in presence of oxygen, leading to the formation of HO_2 radicals was considered. However, due to a lack of sufficient experiments as a result of some technical limitations, no definite explanation could be given to explain the observed disagreement between the TOF-MS studies and the time resolved UV measurements.

Nonetheless, a mechanism that could coherently explain the UV measurements alone was proposed. New branching ratios for HMB-OH (30%) and PMB (70%) were assumed and the back dissociation of the HMB-OH adduct at 373K was obtained by simulating the HMB-OH adduct decay profiles at 328 nm. Using the proposed mechanism, all the time resolved UV decay profiles of HMB-OH were simulated and the UV spectrum of the HMB-OH adduct was obtained. The recorded spectrum was found to be in good agreement with the previously reported m-xylene-OH and mesitylene-OH adduct spectra. Hence the existence of the HMB-OH adduct as one of the oxidation product of HMB was confirmed. The existence of the PMB could not be confirmed as the spectrum obtained from the simulations of the species which was assumed to be PMB, did not match the reported spectrum of the Benzyl radical.

Furthermore, the decomposition of the HMB-OH adduct was studied as function of oxygen concentration. The HMB-OH adduct was found to decay rapidly in the presence of small amounts of O_2. By simulating these decay kinetics as a function of O_2, a rate constant for the reaction of HMB-OH+O_2 of $k_{HMB\text{-}OH+O2}$ = (2.9±0.4) x 10^{-13} cm^3 $molecule^{-1}$ $s^{-1}$was estimated. The estimated value of $k_{HMB\text{-}OH+O2}$ = (2.9±0.4) x 10^{-13} cm^3 $molecule^{-1}$ s^{-1} was readjusted considering the reaction of HMB-OH+HO_2, assuming the possible photolysis of HMB at 248 nm and accounting for the amount of HO_2 that could be produced, calculated from refernce [30]. The new value of $k_{HMB\text{-}OH+O2}$ = (2.3±0.3) x 10^{-13} cm^3 $molecule^{-1}$ s^{-1} was found to be in even better agreement with the reported value of (1.8±0.3) x 10^{-13} cm^3 $molecule^{-1}$ s^{-1} by Koch et al. [6].

5.4 Future work

- The use of excimer laser at 248 nm to produce OH radicals possibly leads to complications due to the 2 photon absorption by the aromatic compounds which might lead to the production of unknown radical species. This problem could be avoided by generating OH at wavelengths at which aromatics either do not absorb or absorb very little so as to restrict the production of 2 photon excited species.

- HONO could be used as a source of OH instead of H_2O_2 by photolysing HONO.

- A new reactor specially designed to work over a larger temperature range needs to be build so that the equilibrium of the HMB-OH adduct can be studied.

- Experiments must be done by changing the radical concentrations which can be achieved by varying the photolysis laser energy over a larger range so as to observe and understand the change in the radical chemistry.

5.5 Reference

1. J. G. Calvert, R. Atkinson, K. H. Becker, R. M. Kamens, J. H. Seinfeld, T. J. Wallington, G.Yarwood, The mechanisms of atmospheric oxidation of aromatic hydrocarbons. Oxford University Press: Oxford, U.K (2002).

2. D. Johnson, S. Raoult, M.T. Rayez, J.C. Rayez, R. Lesclaux: Phys. Chem. Chem. Phys. 4, 4678–4686 (2002).

3. R. Atkinson: J.Phys.Chem.Ref.Data, Monograph 1. (1989).

4. R. Atkinson, S.M. Aschamann, J. Arey: Int. J.Chem. Kinet. 23, 77–97 (1991).

5. D. Johnson, S. Raoult, R. Lesclaux, L. N. Krasnoperov, J. Photochemistry and Photobiology A: Chemistry. 176, 98–106 (2005).

6. Koch, R. Knispel, M. Elend, M. Siese, and C. Zetzsch: Atmos. Chem. Phys. 7, 2057–2071 (2007).

7. B. Bohn, C. Zetzsch: Phys. Chem. Chem. Phys. 1, 5097–5107 (1999).

8. S. Nehr, B. Bohn, A. Hofzumahaus, A. Wahner, Phys. Chem.Chem.Phys. 13, 10699–708 (2011).

9. R. Volkamer, U. Platt, K. Wirtz, B. Klotz, I. Barnes, T. Imamura, N. Washida, K.H. Becker: Phys. Chem. Chem. Phys. 4, 1598–1610 (2002).

10. R. Volkamer: A DOAS study on the oxidation mechanism of aromatic hydrocarbons under simulated atmospheric condition, (2001).

11. R. Volkamer, U. Platt, K. Wirtz: J. Phys.Chem A. 105, 7865–7874 (2001).

12. J. Noda, R. Volkamer, M. J. Molina: J. Phys. Chem. 113, 9658– 9666 (2009).

13. S.M. Aschamann, J. Arey, R. Atkinson, Atmos. Env. 44, 3970 (2010).

14. Berndt and Böge: Int. J. Chem. Kinet. 33, 124–129 (2001).

15. C. Rio, P-M Flaud, J-C Loison, E Villenave: Chem. Phys. Chem. (2010).

16. J.C. Person, P.P. Nicole: J.Chem.Phys. 53, 1767 (1970).

17. Z. Zhou, M. Xie, Z. Wang, F. Qi: Rapid Commun. Mass Spectrom. 23, 3994–4002. (2009).

18. H. Koizumi: J.Chem.Phys. 95, 5846 (1991).

18*. J.C. Loison, M.T. Rayez, J.C. Rayez, A.Gratien, P. Morajkar, C. Fittschen, E.Villenave. Submitted to J. Phys. Chem. A July (2012).

19. F. Markert, P. Pagsberg. Chem. Phys. Lett. 209, 445–454 (1993).

20. J. Thiebaud, A. Aluculesei, C. Fittschen, J.Chem.Phys. 126, 186101–186101–2 (2007).

21. G.L. Vaghjiani, A.R. Ravishankara, J.Chem.Phys. 92, 996–1003 (1990).

22. R. Atkinson, D.L. Baulch, R.A. Cox, J.N. Crowley, R.F. Hampson, R.G. Hynes, M.E. Jenkin, M.J. Rossi, J.Troe, Atmos. Chem. Phys. 4, 1461–1738 (2004).

23. B. Bohn: J. Phys. Chem. A. 105, 6092–6101 (2001).

24. M. Markgraf, J. Troe, J.Phys.Chem. 92, 4899 – 4905 (1988).

25. A.A. Boyd, B. Noziere, R. Lesclaux, Phys. Chem. 99, 10815 – 10823 (1995).

26. A.W. Birdsall, J.F. Andreoni, M.J. Elrod, J.Phys.Chem. A. 114, 10655–10663 (2010).

27. F.F. Fenter, B. Nozière, F. Caralp, R. Lesclaux, Int. J. Chem. Kinet. 26, 171–189 (1994).

28. S. Nehr, B. Bohn, A. Wahner, J. Phys. Chem. A. 116, 6015–6026 (2011).

29. G.S. Tyndall, R.A. Cox, C. Granier, R. Lesclaux, G.K. Moortgat, M.J. Pilling, A.R. Ravishankara, T.J. Wallington: J. Geophys. Res. D. 106, 12157–12182 (2001).

30. C. Jain, P. Morajkar, C. Schoemaecker, C. Fittschen, J. Phys. Chem. A. 116, 6231–6239 (2012).

31. C. Jain, A. Parker, C. Schoemaeker, C. Fittschen: Chem.Phys.Chem. 11, 3867–3873 (2010).

32. A. Aluculesei, A.Tomas, C. Schoemaecker, C. Fittschen, App. Phys. B: Lasers and Optics. 92, 379–385 (2008).

33. V. Talrose, E.B. Stern, A.A. Goncharova, N.A. Messineva, N.V. Trusova, M.V. Efimkina, P.J. Linstrom, W.G. Mallard: ‘UV/Visible Spectra’ in NIST Chemistry WebBook, NIST Standard Reference Database Number 69, Eds. National Institute of Standards and Technology, Gaithersburg MD.

34. A. Bolovinos, J. Philis, E. Pantos, P. Tsekeris, G. Andritsopoulos. J. Mol. Spectrosc. 94, 55–68 (1982).

Thesis Summary

Thesis Summary

This thesis begins with a brief introduction to the photochemistry of the troposphere with special emphasis on the chemistry of OH and HO_2 radicals. The chapter also emphasizes on the tropospheric pollution caused by large amounts of NO_x and VOCs that are emitted to the troposphere both from natural and anthropogenic sources. The sources and the possible sinks of some of the organic compounds such as Formaldehyde, Acetaldehyde, Hexamethyl benzene, which were studied during the course of this thesis along with important monocyclic aromatic compounds such as Benzene, Toluene and Xylenes have also been discussed. Towards the end of the chapter 1, a brief description has been given of the fundamental principles underlying the three experimental techniques used in this thesis, namely UV spectroscopy, continuous wave-Cavity Ring-down Spectroscopy (cw-CRDS) and Laser Induced Fluorescence (LIF) which were used to investigate the HMB-OH adduct, HO_2 and OH radicals respectively.

Chapter 2 provides a detailed description of the instrumentation and the experimental techniques used for the entire work of this thesis. The first half of this chapter deals with the simultaneous measurements of HO_2 and OH radicals using the laser photolysis coupled to continuous wave-Cavity Ring-down Spectroscopy (cw-CRDS) and Laser Induced Fluorescence (LIF) techniques respectively, which were used to measure a) the absolute cross section of formaldehyde in the near IR region and to investigate the equilibrium of $CH_2O + HO_2$ reaction and b) the measurements of the quantum yields of HCO and H atoms from the 248 nm photolysis of Acetaldehyde at the university of Lille 1. The second half of the chapter 2 deals with the laser photolysis coupled to time resolved UV spectroscopy technique which was used to record the UV absorption spectrum of the HMB-OH adduct and its decay kinetics under atmospheric conditions at the university of Bordeaux 1. The Discharge fast flow tube coupled to time of flight mass spectroscopy (TOF-MS) studies that were carried out by J.C Loison for product determination of the OH initiated oxidation of HMB are also presented.

Chapter 3 presents the results and discussion of the absorption cross section measurement of formaldehyde in the near IR region in the first half of this chapter. In order to measure the absorption cross section of formaldehyde in the near IR region, cw-CRDS technique was employed to obtain the absorption spectra. The concentration of formaldehyde was measured by monitoring the reaction of OH radicals with formaldehyde (in large excess) using LIF technique. Knowing the absorption coefficient (from the absorption spectrum) and the concentration of formaldehyde, the absorption cross section of formaldehyde at two selected lines in the near IR region at 10 and 50 Torr were obtained. The measured values were found to be a factor of 2 lower than those reported by Staak et al. (2005).

The second half of this chapter presents the chemistry of CH_2O + HO_2 equilibrium. The absorption cross section of formaldehyde measured in the first half of this thesis was used to calculate the formaldehyde concentrations employed in the equilibrium constant measurement study. The HO_2 decay profiles were monitored using the laser photolysis coupled to cw-CRDS technique in presence of large excess of formaldehyde and the recorded profiles were simulated to obtain the equilibrium constant using a known reaction mechanism for the system under investigation. The measured equilibrium constant was validated by performing similar experiments over the temperature range of 292K – 306K. The measured equilibrium constant values were found to be in good agreement with the IUPAC recommended values. However, the individual rate constants for the association and back dissociation reaction were found to be ~ 2 times lower than the reported values of Veyret et al.(1989) obtained through fairly indirect measurements.

Chapter 4 of this thesis presents the results obtained for the quantum yield measurements of HCO and H atoms produced from the 248 nm photolysis of acetaldehyde. The H and the HCO radicals were converted into HO_2 radicals in presence of O_2 and the HO_2 concentration- time profiles were measured using laser photolysis coupled to cw-CRDS technique. The quantum yields were obtained by simulating the HO_2 profiles under different experimental consditions such as O_2 concentration, photolysis laser energy, acetaldehyde concentration and pressure. The measured quantum yields of HCO and H atoms were found to be 0.20± 0.02 and 0.17± 0.02 for HCO and H atoms respectively. This study was extended to understand the fate of the HO_2 radicals in the given reaction system. The rate constant for the reaction of HO_2 + CH_3 and the equilibrium constant for HO_2 + CH_3CHO were also investigated. The measured rate constant $k_{CH3\ +\ HO2}$ and the equilibrium constant was found to be in good agreement with the literature reported data. In addition to this, it has been speculated from this study that the unknown product (X) produced from the CH_3CO + O_2 reaction could react with HO_2 radicals in the given reaction system. However, this reaction needs further investigation. All the above studies were carried out at the University of Lille1.

The final Chapter 5 of this thesis presents the OH initiated oxidation of Hexamethyl benzene (HMB) using Laser photolysis coupled to time resolved UV spectroscopy. This study was carried out at the university of Bordeaux 1. The HMBOH adduct was formed by the reaction OH radicals (produced from the 248 nm photolysis of H_2O_2) with HMB. The UV absorption spectrum of the HMBOH adduct recorded in this study was found to have close resemblence to the reported m-Xylene-OH adduct and Mesitylene-OH adduct spectra, confirming the formation of HMBOH adduct.

The above reaction system was simultaneously investigated using discharge fast flow tube coupled to TOF-MS by J.C Loison at the university of Bordeaux 1. These results have also been presented for comparison. The TOF – MS studies provided the identification of different products of OH + HMB reaction. Based on the knowledge of the products, a possible global mechasim of the OH initiated oxidation of HMB was proposed. However, the two studies disgreed on the HMBOH decomposition channel leading to HMB + OH. The exact reason for the above disagreement has not been understood. However, it can be speculated that the 248 nm photolysis of HMB could lead to some unknown radical species which could react with the HMBOH adduct in case of UV studies whereas such an effect might not be observed in the TOF-MS measurements.

At the end of each Chapter, the possible improvements that can be made in the future works of each of the studies undertakenduring the course of this thesis, has been proposed.

Appendices

Appendix - Academic Records

I – Publications

1. P. Morajkar, C. Schoemaecker, C. Fittschen : Absolute absorption cross section of two selected formaldehyde lines in the near IR region: *J. Molec. Spect. 281, 18-22 (2012).*

2. C. Jain, P. Morajkar, C. Schoemaecker, B. Viskolcz, C. Fittschen: Measurement of absolute absorption cross sections for HONO in the near infrared region by cw-CRDS technique coupled to laser photolysis: *J. Phys. Chem. A. 115, 10720-10728 (2011).*

3. C. Jain, P. Morajkar, C. Schomaecker, C. Fittschen.Formation of HO_2 radicals from the 248 nm two photon excitation of different aromatic hydrocarbons in presence of O_2**.** *J. Phys. Chem. A**,** 116, 24, 6231-6239**,** (2012)*

4. C. Loison, M.T. Rayez, J.C. Rayez, P. Morajkar A. Gratien, C. Fittschen, E. Villenave Gas phase reaction of hydroxyl radicals with Hexamethyl benzene Submitted to the *Journal of Physical Chemistry A, July 2012*

5. P. Morajkar, C. Schomaecker, M. Okumura, C. Fittschen : Measurement of equilibrium constant for the reaction of CH_2O + HO_2 radicals using laser photolysis coupled to cw-CRDS technique *(manuscript under preparation).*

6. S. González, M. Antiñolo, P. Morajkar, C. Schoemaecker, J. Albaladejo , E. Jiménez, C. Fittschen : Pulsed laser photolysis of CH_3CHO at 248 nm: Overall Quantum Yield, and CH_4, HCO and H Primary Quantum Yields *(manuscript under preparation).*

II - Oral presentations

1. OH initiated oxidation of aromatic compounds: the special case of Hexamethyl benzene, DFG-CNRS meeting, Bayreuth (Germany), February 2010
2. Quantum yield of HCO and H atoms from the 248 nm photolysis of acetaldehyde and the reaction kinetics of CH_3 + HO_2 radicals. Journée des doctorants IRePSE, Lille, (France) May 2011
3. Quantum yield of HCO and H atoms from the 248 nm photolysis of acetaldehyde. Journée des doctorants IRENI, Lille, (France) May 2011
4. Quantum yield of HCO and H atoms from the 248 nm photolysis of acetaldehyde and the reaction kinetics of CH_3 + HO_2 radicals. GFCP, Bordeaux, (France) June 2011

III - Poster presentations

1. OH initiated oxidation of Hexamethylbenzene. GFCP Wimereux, (France), June 2010
2. Measurement of equilibrium constant for the reaction of CH_2O + HO_2 radicals using laser photolysis coupled to cw-CRDS technique Journée IRENI, Lille, (France) May 2011
3. A kinetic study of the gas phase reaction of CH_2O + HO_2 radicals. GK, Boulder Colorado (USA), June 2012

IV - Conferences and meetings attended

1. Workshop on Atmospheric Chemistry: kinetics and spectroscopy, Bayreuth, (Germany), February 2010
2. Conférence annuelle de Cinétique et de Photochimie, Wimereux, (France) June 2010.
3. Journée des doctorants IRePSE, Lille, (France) March 2011.
4. Journée des Doctorants, Douai, (France), May 2011
5. Journée des Doctorants, IRENI, Douai, (France), May 2011

6. Réunions du Groupe de Cinétique et Photochimie en Phase Gazeuse, (GFCP) et Interface Chimie-Spectroscopie Atmosphériques (ICSA), Lille, (France), May 2011.
7. Journée des Doctorants IRePSE, Lille, (France) May 2012
8. Journée des Doctorants, IRENI, Lille, (France), May 2012
9. Réunions du Groupe de Cinétique et Photochimie en Phase Gazeuse, (GFCP) Bordeaux, (France), June 2012.
10. 22nd Symposium on Gas Kinetics, Boulder, Colorado, (USA), June 2012